

Stephen F. Austin State University

SFA ScholarWorks

Electronic Theses and Dissertations

5-12-2018

A Geophysical Delineation of A Normal Fault Within the Gulf Coastal Plain, Montgomery County, Texas

Danielle Minter

minterdr@jacks.sfasu.edu

Follow this and additional works at: <https://scholarworks.sfasu.edu/etds>



Part of the [Geology Commons](#), and the [Geophysics and Seismology Commons](#)

[Tell us](#) how this article helped you.

Repository Citation

Minter, Danielle, "A Geophysical Delineation of A Normal Fault Within the Gulf Coastal Plain, Montgomery County, Texas" (2018). *Electronic Theses and Dissertations*. 153.

<https://scholarworks.sfasu.edu/etds/153>

This Thesis is brought to you for free and open access by SFA ScholarWorks. It has been accepted for inclusion in Electronic Theses and Dissertations by an authorized administrator of SFA ScholarWorks. For more information, please contact cdsscholarworks@sfasu.edu.

A Geophysical Delineation of A Normal Fault Within the Gulf Coastal Plain, Montgomery County, Texas

Creative Commons License



This work is licensed under a [Creative Commons Attribution-Noncommercial-No Derivative Works 4.0 License](https://creativecommons.org/licenses/by-nc-nd/4.0/).

A GEOPHYSICAL DELINEATION OF A NORMAL FAULT WITHIN THE GULF
COASTAL PLAIN, MONTGOMERY COUNTY, TEXAS

By

Danielle Renee Minter, Bachelor of Science

Presented to the Faculty of the Graduate School of

Stephen F. Austin State University

In Partial Fulfillment

Of the Requirements

For the Degree of Master of Science

STEPHEN F. AUSTIN STATE UNIVERSITY

May, 2018

A GEOPHYSICAL DELINEATION OF A NORMAL FAULT WITHIN THE GULF
COASTAL PLAIN, MONTGOMERY COUNTY, TEXAS

By

DANIELLE RENEE MINTEER, Bachelor of Science

APPROVED:

Dr. Wesley Brown, Thesis Director

Dr. Melinda Faulkner, Committee Member

Dr. Chris Barker, Committee Member

Dr. Joseph Musser, Committee Member

Pauline Sampson, Ph.D.

Dean of the Graduate School

ABSTRACT

The Gulf Coast of Texas has been a known hydrocarbon basin for many years with various structural trapping mechanisms such as anticlines, faults and salt domes. While most large salt domes have been extensively studied in the Gulf Coastal Plain, many smaller normal faults have not been studied in detail. This research study employs an integrated geophysical approach to mapping the Big Barn fault in Montgomery County, Texas. This fault is located on the Gulf Coastal Plain and is approximately 20 miles north of Houston, Texas. Most normal faults in the Gulf Coastal Plain formed as a result of the Gulf of Mexico basin which started during the Jurassic Period as a result of the breakup of Pangea and the rifting of North and South America. The Big Barn fault formed during the Jurassic but there is evidence that the fault plane has been recently reactivated. Within the past 20 years, extensive deformation and fractures within the vicinity of the fault have formed on Interstate Highway 45 (IH 45) and caused damage to nearby businesses and residences. In this study gravity, electrical resistivity surveys and traditional mapping techniques were conducted to determine the cause of deformation and the extent of faulting. Two-dimensional inverted resistivity models were made to determine the structures and stratigraphy of the area.

ACKNOWLEDGEMENT

I would like to thank the many people that have helped me complete my thesis work. I first thank my thesis advisor Dr. Brown for being supportive of my research and for being a great mentor. I am also sincerely grateful to all of the committee members who oversaw my thesis work.

I am thankful to the many friends and family that helped me complete my field work, including Justin Chavez, Melanie Seymour, Adam Chavez and Monique Gonzales. I am thankful for the Callahan family and their endearing support of my thesis work. I am also thankful to the friends that critiqued my work, Kayleigh Davis and Daniel Savarese.

I am also deeply grateful for the help and encouragement from my parents Cheryl Lambeth and James Minter. Finally, I would finally like to thank my husband Joe Callahan and my son, William Callahan for their endless faith and love for me and support for my fieldwork.

TABLE OF CONTENTS

ABSTRACT	i
ACKNOWLEDGEMENT	ii
TABLE OF CONTENTS	iii
CHAPTER 1	1
1.1 INTRODUCTION.....	1
1.2 PREVIOUS WORKS.....	5
CHAPTER 2	13
2.1 REGIONAL GEOLOGY	13
2.2 STRUCTURE	15
2.2.1 IAPETAN RIFTED MARGIN.....	18
2.2.2 GULFIAN TECTONIC CYCLE	20
2.2.3 GULF COAST GEOSYNCLINE	23
2.2.4 THE SABINE UPLIFT	25
2.2.5 LULING-MEXIA-TALCO FAULT ZONE.....	28
2.2.6 BALCONES FAULT ZONE	30
2.2.7 MOUNT ENTERPRISE FAULT ZONE	32
2.2.8 EAST TEXAS EMBAYMENT.....	33
2.2.9 RIO GRANDE EMBAYMENT	34
2.2.10 SALT DOMES.....	34
2.3 STRATIGRAPHY.....	37
2.3.1 PRE-JURASSIC	39
2.3.2 JURASSIC.....	40

2.3.3 CRETACEOUS.....	40
2.3.4 EOCENE TO MIOCENE	43
2.3.5 PLEISTOCENE AND HOLOCENE.....	46
2.3.5.1 LISSIE FORMATION.....	46
2.3.5.2 WILLIS FORMATION	48
CHAPTER 3	49
3.1 GRAVITY THEORY	49
3.1.1 APPLIED GRAVITY CORRECTIONS	53
3.1.2 DRIFT CORRECTION.....	53
3.1.3 ELEVATION CORRECTION	54
3.2 ELECTRICAL RESISTIVITY THEORY	57
CHAPTER 4	66
4.0 METHODOLOGY	66
4.1 GRAVIMETRY METHODOLOGY.....	67
4.1.1 LiDAR.....	70
4.1.2 DATA COLLECTION AND PROCESSING	70
4.2 CAPACITIVELY COUPLED RESISTIVITY METHODOLOGY.....	76
4.2.1 FIELD SETUP.....	79
4.2.2 DATA PROCESSING	80
4.2.3 PSEUDOSECTIONS	82
4.2.4 DATA MISFIT.....	85
4.3 MULTI-ELECTRODE ELECTRICAL RESISTIVITY METHODOLOGY	89
4.3.1 COMMAND FILES	91
4.3.2 DATA ACQUISITION.....	94
4.3.3 FIELD SETUP.....	94

4.3.4 DATA PROCESSING AND PSEUDOSECTIONS	98
CHAPTER 5	99
5.0 RESULTS	99
5.1 GRAVIMETRY	102
5.2 CAPACITIVELY COUPLED RESISTIVITY	109
5.3 MULTI-ELECTRODE RESISTIVITY	113
CHAPTER 6	119
6.0 DISCUSSION	119
CHAPTER 7	134
7.0 LIMITATIONS	134
7.1 CONCLUSION	135
7.2 FUTURE WORK	137
REFERENCES	138
APPENDIX	144
A.1 DATA REMOVAL	144
A.2 GRAVIMETRY CORRECTIONS	146
A.3 CROSSPLOT OF MEASURED VS APPARENT RESISTIVITY	149
VITA	153

LIST OF FIGURES

Figure 1. Study Area.....	2
Figure 2. Observed Faulting Location.....	4
Figure 3. Big Barn Fault	6
Figure 4. Listric Faulting Model.....	8
Figure 5. Fault Model.....	9
Figure 6. Gravity Study on Hockley Fault.....	10
Figure 7. Electrical Resistivity Study on the Hockely Fault.....	11
Figure 8. Glide and Shear Tectonic Models.....	17
Figure 9. Palinspastically Restored Margin of Southern Laurentia	19
Figure 10. Tectonic Stages of the Evolution of the Gulf of Mexico.....	22
Figure 11. Gulf Coast Geosyncline	24
Figure 12. Regional Structures in the Texas Gulf Coast.....	26
Figure 13. Major Regional Fault Zones	27
Figure 14. Cross Section of Mexia-Talco Graben.....	29
Figure 15. Cross Section of Balcones Fault Zone	31
Figure 16. Cross Section of the Mount Enterprise Fault Zone.....	33
Figure 17. Faulting Around Salt Domes.....	36
Figure 18. Stratigraphic Column of the Texas Gulf Coast	37
Figure 19. Stratigraphic Atlas of the Texas Gulf Coast.....	38
Figure 20. North American Intercontinental Seaway (Midway Sea).....	43
Figure 21. Modern Free-Fall Method for Determining Absolute Gravity.....	51
Figure 22. Conceptual Model of Capacitively Coupled Resistivity	60
Figure 23. Electrical Resistivity Current Flow Paths.....	61
Figure 24. Common Electrical Resistivity Array Configurations	63
Figure 25. Apparent Resistivity for 2D Pseudosections for Various Arrays.....	64
Figure 26. Trimble NOMAD GPS Unit	69
Figure 27. Gravity Field Survey Lines.....	71
Figure 28. Field Setup of Gravimeter.....	73
Figure 29. Absolute Gravity Base Station	75
Figure 30. Field Setup for OhmMapper	77
Figure 31. Grid Orientation for OhmMapper Surveys.....	80
Figure 32. Grid Orientation for OhmMapper Surveys.....	81
Figure 33. Capacitively Coupled Resistivity Pseudosection from Field Site 2	83
Figure 34. Initial Settings in Earth Imager 2D for OhmMapper Survey	84
Figure 35. Resistivity Inversion Settings in Earth Imager 2D Software	86

Figure 36. Data Misfit Histogram for CCR Field Survey Site 2	87
Figure 37. Crossplot of Measured vs. Predicted Apparent resistivity for CCR Surveys ..	88
Figure 38. Super Sting Field Sites.....	90
Figure 39. SuperSting R2 Electrical Resistivity Meter Setup	90
Figure 40. Parameters for a Dipole-Dipole Electrical Resistivity Survey	92
Figure 41. Dipole-Dipole Electrode Configuration.....	93
Figure 42. Schematic of Field Surveying with SuperSting.....	95
Figure 43. Field Setup of 28-Electrode SuperSting Survey.....	95
Figure 44. Pseudosection Monitored During SuperSting Field Survey	97
Figure 45. Study Area Regional Location.....	100
Figure 46. Gravity Data from Field Site 1	103
Figure 47. Gravity Data from Field Site 2	104
Figure 48. Gravity Data from Field Site 3.....	105
Figure 49. Gravity Data from Field Site 4	106
Figure 50. Gravity Data from Field Site 5	107
Figure 51. Gravity Data from Field	108
Figure 52. CCR Survey Site 2 Data	110
Figure 53. CCR Survey Site 3 Data	111
Figure 54. CCR Survey Site 7 Data	112
Figure 55. Multi-electrode Resistivity Survey Site 1	114
Figure 56. Multi-electrode Resistivity Survey Site 2 (4 Meter Survey).....	115
Figure 57. Multi-electrode Resistivity Survey Site 2 (6.5 Meter Survey)	116
Figure 58. Multi-electrode Resistivity Survey Site 5	117
Figure 59. Multi-electrode Resistivity Survey Site 7	118
Figure 60. All Geophysical Data from Field Site 1	121
Figure 61. All Geophysical Data from Field Site 2	123
Figure 62. All Geophysical Data from Field Site 3	125
Figure 63. All Geophysical Data from Field Site 4	127
Figure 64. All Geophysical Data from Field Site 5	129
Figure 65. All Geophysical Data from Field Site 6	131
Figure 66. All Geophysical Data from Field Site 7	133
Figure 67. Crossplot from CCR Survey Site 2.....	149
Figure 68. Crossplot from CCR Survey Site 3.....	150
Figure 69. Crossplot from CCR Survey Site 7.....	150
Figure 70. Crossplot from Multi-electrode Resistivity Survey Site 1.....	151
Figure 71. Crossplot from Multi-electrode Resistivity Survey Site 2.....	151
Figure 72. Crossplot from Multi-electrode Resistivity Survey Site 5	151
Figure 73. Crossplot from Multi-electrode Resistivity Survey Site 7	152

LIST OF TABLES

Table 1. Regional Faulting Data	12
Table 2. Gravity Field Site Information.....	72
Table 3. OhmMapper Specifications	78
Table 4. SuperSting Survey Sites and Field Parameters	91
Table 5. Techniques Used and Fault Trends at Each Field Site.....	101
Table 6. Capacitively Coupled Electrical Resistivity Data Removal Percentages.....	144
Table 7. Multi-Electrode Electrical Resistivity Removal Percentages	145

LIST OF EQUATIONS

Equation 1	$F = \frac{Gm_1m_2}{r^2}$	49
Equation 2	$F = mg = -k(s-s_0)$	52
Equation 3	Free-air correction (FAC) = 0.3086 h	55
Equation 4	Bouguer correction (BC)S = 0.4193ph	56
Equation 5	$R = \Delta V I$	57
Equation 6	resistance, $R = \text{resistivity } (\rho) \times \frac{\text{length}}{\text{area of cross-section}}$	58
Equation 7	resistivity, $\rho = \text{resistance } (\times) \times \frac{\text{area of cross-section}}{\text{length}}$	58

CHAPTER 1

1.1 INTRODUCTION

The study area is located approximately 6.5 miles north of the Woodlands on Interstate 45, Montgomery County, Texas (Figure 1). This study examined a northeast trending fault line through the study area that caused fractures on the freeway and frontage roads. Residential homes and commercial businesses situated within the vicinity of the fault line have also been affected in many cases. The primary goal of this study was to use an integrated geophysical approach to map and produce a model for this previously unstudied fault line.

This research study employed traditional geological mapping, gravitational and resistivity surveys to map a fault line in Montgomery County, Texas. Two of the main fault lines within the study area have not been formally named or entered by United State Geological Survey (USGS), in their database but are referred to by Fugro Consultants as the Big Barn fault and the Egypt fault (Fugro Consultants, Inc., 2012).

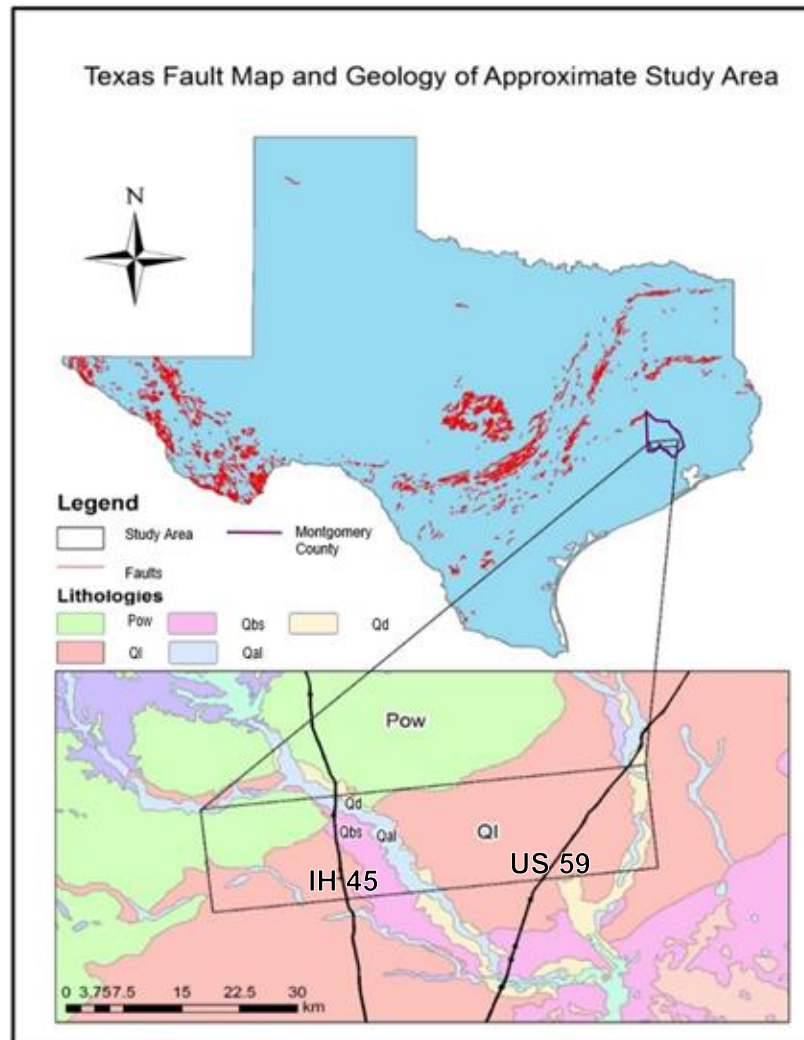


Figure 1. Study Area

The study area extends from Interstate Highway 45 (IH 45) to U.S. Route 59 (US 59) and is shown with a black rectangular box. The upper map shows the location of major faults in Texas recognized by the United States Geological Survey (USGS), Texas Natural Resources Information System (TNRIS) and the Bureau of Economic Geology (BEG). Montgomery County is outlined in purple and the thick red lines represent recognized fault lines. The lower figure shows the study area, the primary geologic units and the major highways within the study area. The primary geologic units in the study are the Lissie Sand (Ql) and the Willis Clay (Pow).

This study focused on the Big Barn fault, which is located in Montgomery County, Texas. In the Texas Coastal Zone, there have been over 450 active surface faults identified, but no recorded geophysical studies have been done in southern Montgomery County, Texas. Some of the faults in the Texas Coastal Zone were first identified by Norman and Britt, 1991, where the general trends and the start of deformation were recorded. The Big Barn fault and Egypt fault have not been extensively studied; however these faults have been mentioned in multiple articles (Fugro Consultants, Inc., 2012; Norman and Britt, 1991). A detailed fault study has been done on the Hockley fault system in Harris County, which is located to the southwest of the study area. It is a reference for the Big Barn fault and is a source of geophysical information on the area (Khan, et. al., 2013; Saribudak, 2011).

The study area was selected because the Big Barn fault has caused extensive damage to residential homes, commercial businesses and roadways in the area (Figure 2). Commercial businesses located within the vicinity of the fault line have experienced damaged parking lots and buildings, while residents in the area have also experienced damage to their homes due to recent activity associated with movement along the fault line. A field survey was conducted in the study area to delineate the extent of the fault. The location of field sites displaying the most pronounced deformation are shown in Figure 2.

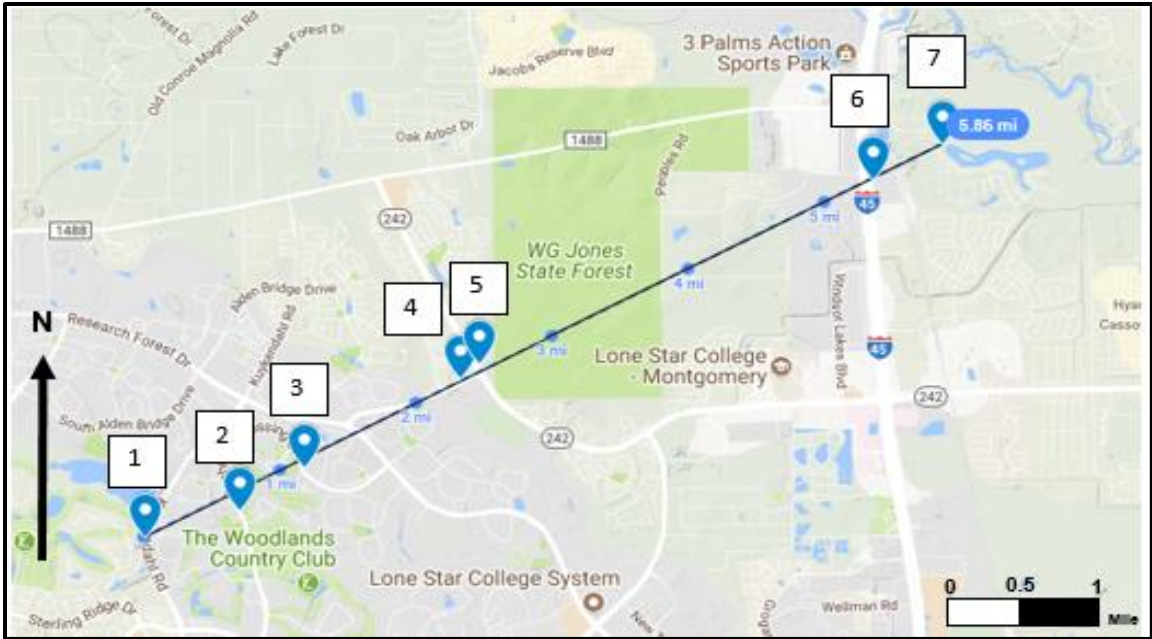


Figure 2. Observed Faulting Location

This figure shows the primary field sites (1-7) where gravity and electrical resistivity measurements were done. These field sites were chosen based on observed surficial deformation and have the most pronounced deformation of the areas examined. The length of the fault line that runs through the primary field sites is 5.86 miles long. The map was made using Google Maps.

This recent reactivation of the fault plane could possibly be caused by factors such as salt dome intrusion or regional subsidence. Electrical resistivity and gravity measurements were used to study the extent of faulting and help establish the mechanism of faulting. A Houston Geological Society field trip guide of the study area noted that core data showed that the Big Barn fault has caused an offset in lithology of 300-400 feet at a depth of 5000 feet (Norman and Britt, 1991). Since the study area was in close proximity to the active Conroe oil field,

core data from wells in the area could not be obtained because the data is proprietary. Subsidence, possibly occurring due to movement toward the Gulf Coast geosyncline, or from over pumping, has been a known problem in the Houston area for many years and could be partially responsible for reactivation of the Big Barn fault. Norman (2005), postulated that groundwater extraction could be a source of reactivation of the fault planes.

1.2 PREVIOUS WORKS

While the Big Barn fault has not been extensively studied, it was mentioned in a field trip guide book by the Houston Geological Society (Norman and Britt, 1991) and in a study completed by Fugro Consultants in 2012. Fugro Consultants acknowledged the presence of faulting in a small portion of the study area; however surficial observations for this study show that the fault line extends a minimum of five miles and potentially extends farther (Figure 3) (Fugro Consultants, Inc., 2012). The maps produced by Fugro Consultants, 2012, also have variability on where the faulting occurred. This study expands upon the earlier study by Fugro Consultants to determine the extent of the fault line.

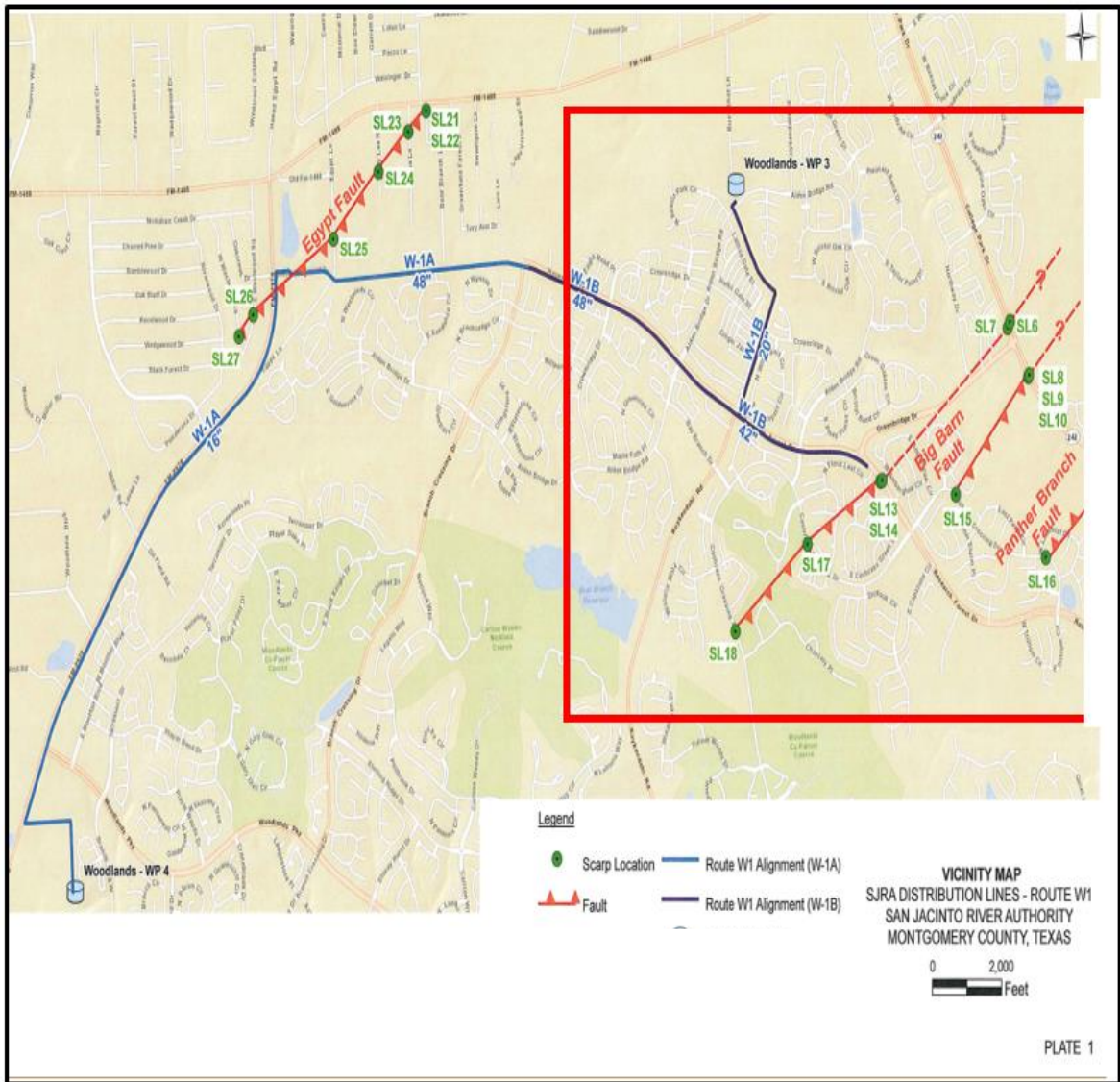


Figure 3. Big Barn Fault

Faulting in the southwestern part of the study area as shown in a previous study completed by Fugro Consultants. Fugro Consultants mapped surficial deformation in association with the Big Barn Fault along with the Egypt Fault and Panther Branch Fault. The red rectangular box shows the southwestern part of the study area for this study compared to the faulting locations outlined by Fugro Consultants (Modified from Fugro Consultants, Inc., 2012).

Previous authors described most these faults as listric normal faults with a curved fault plane that formed due to the opening of the Gulf of Mexico (Norman and Britt, 1991; Hosman, 1996). Norman and Britt, 1991, were able to associate these faults with the opening of the Gulf of Mexico because the faults strike parallel to the coast of Texas and the downthrown side of the fault is toward the coast in most cases. Nearby salt domes could have affected some faults that have differing dip and strike directions. A model of listric normal faulting can be seen in Figure 4.

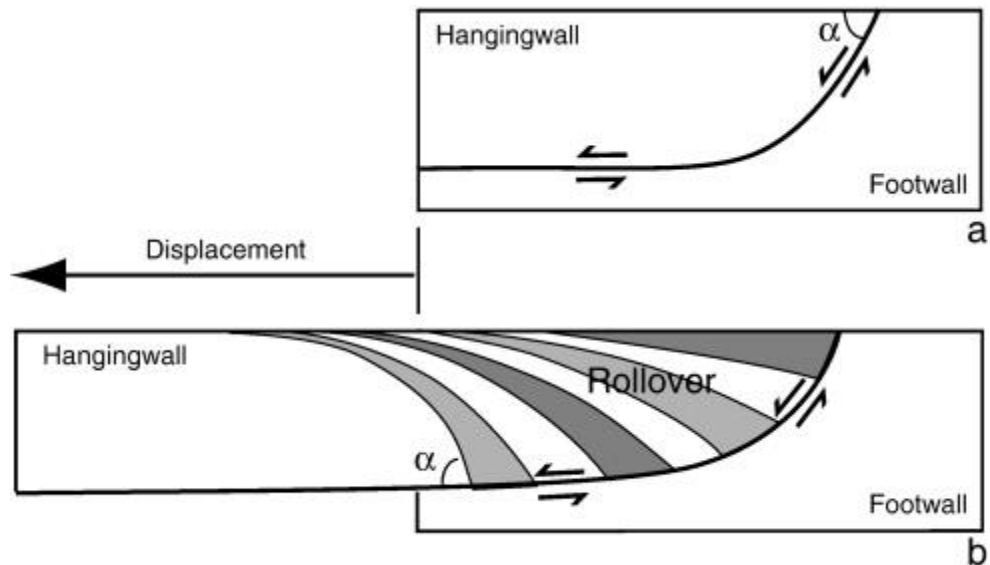


Figure 4. Listic Faulting Model

Listic normal faults have curved fault planes as shown in (a). The curved fault plane can cause the beds to be rotated and rollover structures can form as shown in (b). Rollover structures can be a hydrocarbon trapping mechanism, while the listric fault plane can be a migration pathway for hydrocarbons (Brun and Mauduit, 2008).

Listic normal faults are abundant along the Gulf Coastal Plain of Texas, but the Big Barn fault has other notable features associated with it. The Big Barn fault was found to trend along the truncation of the Lissie Sand and Willis Clay formations, but stratigraphically the Lissie Sand should overlie the Willis Clay. This can be explained by erosion removing the Lissie Sand from the upthrown block and exposing the Willis Clay. A model of faulting in the study area can be seen in Figure 5.

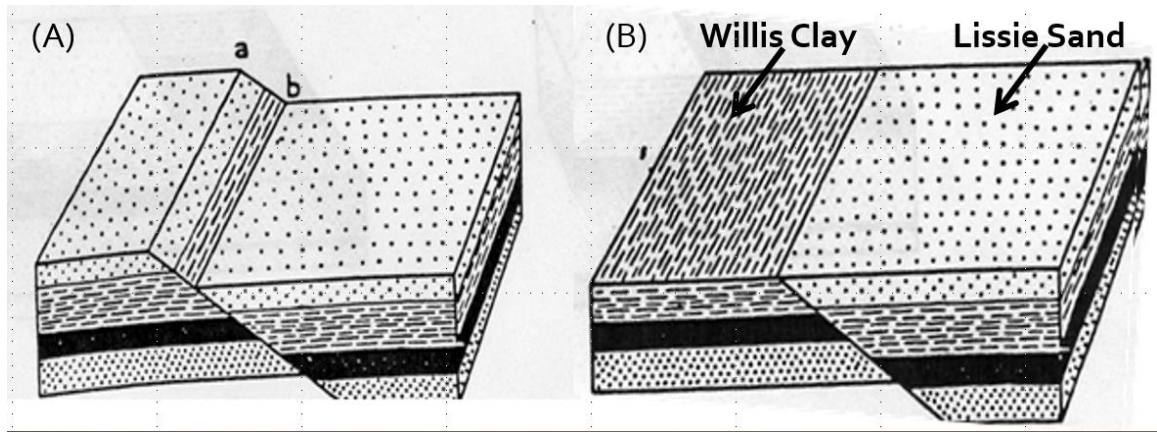


Figure 5. Fault Model

This figure shows a model of the faulting in the study area. (A) shows normal faulting occurring in an area with sand as the upper lithologic unit and shale lying conformably beneath it. (B) shows what the area would look like after erosion has removed overlying material on the upthrown block. The Willis Clay is the upper lithologic unit on the upthrown side of the fault, while the Lissie Sand is the upper lithologic unit on the downthrown side of the fault. In the study area the Willis Clay was found on the upthrown side of the fault, while the Lissie Sand was found on the downthrown side of the fault (modified after Billings, 1972).

Khan et. al., 2013 and Saribudak, 2011 examined the Hockley fault line, located 40 miles to the west of the study area and trends the same as the Big Barn fault (Figure 6). These authors used gravity and electrical resistivity imaging techniques to delineate the Hockley fault and their studies were used as an analog for faulting in the study area (Khan et. al., 2013; Saribudak, 2011). Khan et. al., 2013 delineated the Hockley fault using gravity techniques (Figure 6). The survey revealed higher gravity values on the downthrown side of the fault. This was attributed to the denser Lissie Sand being on the downthrown side of the

fault and juxtaposed against the less dense Willis Clay on the upthrown side of the fault.

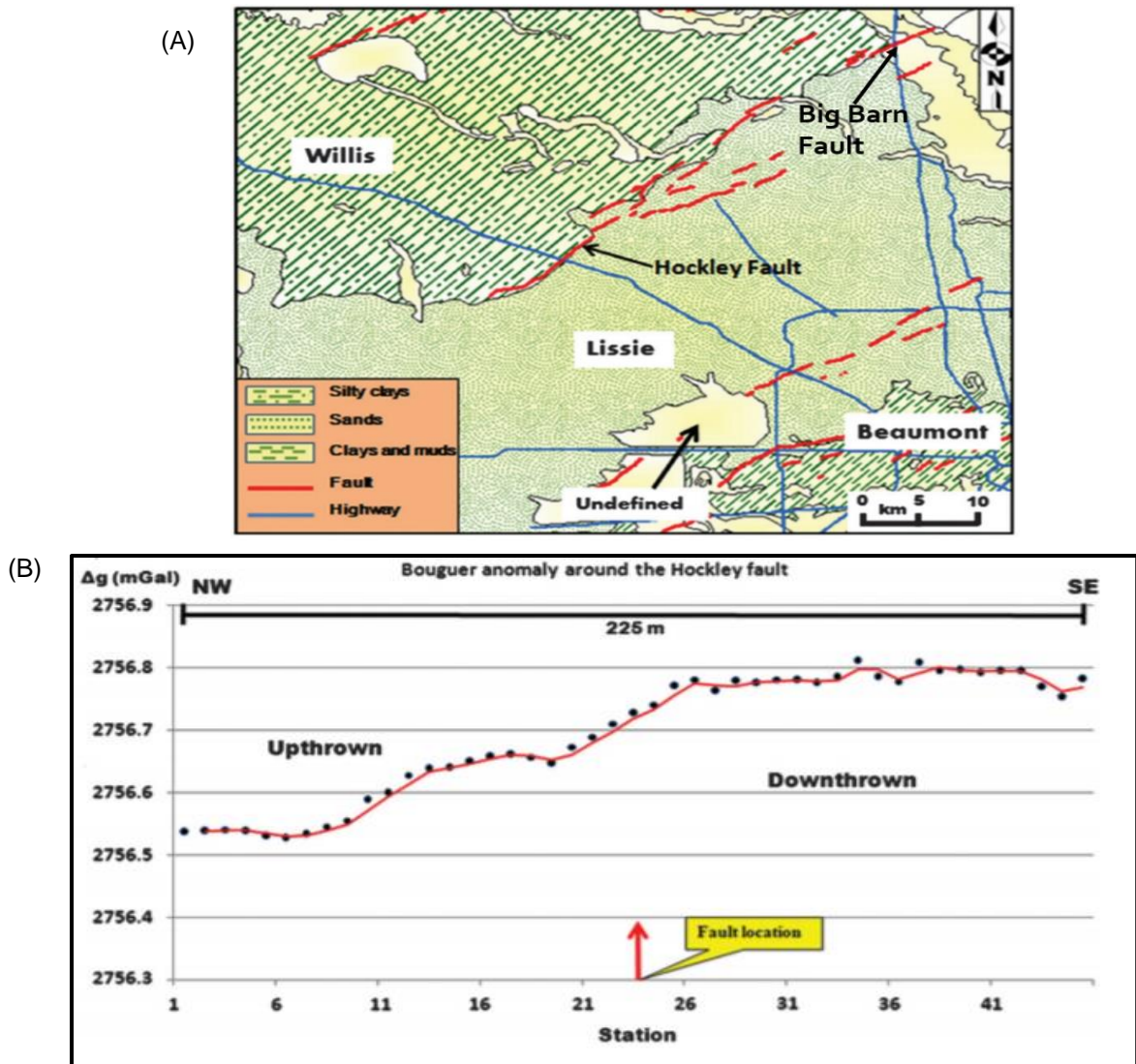


Figure 6. Gravity Study on Hockley Fault

Gravity study done on the Hockley Fault in Harris County, Texas. (A) shows the location of the Hockley Fault compared to the Big Barn Fault. (B) shows a graph of the Bouguer anomaly conducted perpendicular to the Hockley Fault. Higher gravity readings were found on the downthrown side of the fault and lower gravity readings were found on the upthrown side of the fault. The authors concluded that there is higher gravity on the upthrown side of the fault because of a change in surficial lithology. The upthrown side of the fault was found to indicate the denser sandy Lissie Formation and the downthrown side of the fault composed of the less dense clayey Willis Formation (Khan et. al., 2013).

Saribudak, 2011, examined the Hockley fault using electrical resistivity imaging techniques. The authors were able to map to 130m depth and image the Hockley Fault along with the contact between the Willis Clay and the Lissie Sand (Figure 7). The higher resistivity sand was shown with brighter red coloring and the lower resistivity clay was shown with darker blue coloring.

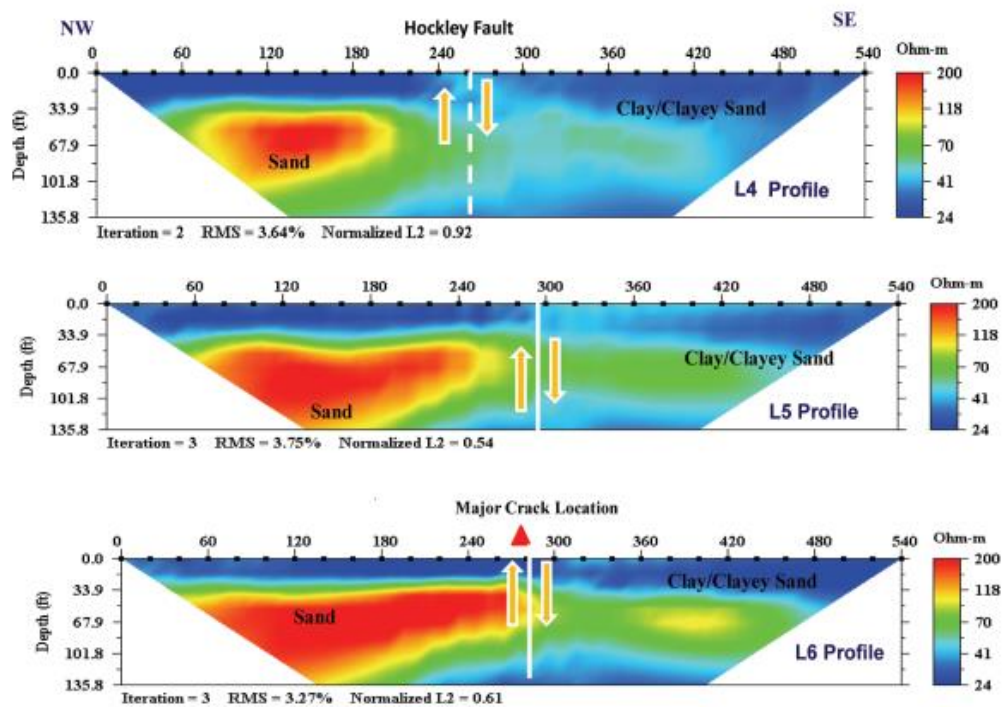


Figure 7. Electrical Resistivity Study on the Hockley Fault

This figure shows an electrical resistivity survey that used Advanced Geosciences, Inc. (AGI) Super R1 Sting/Swift resistivity meter with the dipole-dipole resistivity technique over the Hockley Fault in west Harris County, Texas. Higher resistivity was represented by orange to red colors, while lower resistivity was represented by blue to green colors. The three graphs are representative of three different field sites and the surveys were conducted perpendicular to the Hockley Fault (Saribudak, 2011).

The Houston Geological Society led a field trip in the northern part of the Gulf Coastal plain and noted 11 fault sites, including the Big Barn fault. (Norman and Britt, 1991) (Table 1).

The guidebook published by the Houston Geological Society also mentioned that the Big Barn fault has been recently reactivated (Norman and Britt, 1991). Their guidebook mentioned that some of the faults in the area have been reactivated, with minimal fault movement prior to 1987 and accelerated movement since 1987 (Norman and Britt, 1991; Table 1).

Table 1. Regional Faulting Data

This table shows the rate of movement of fault lines in south Montgomery County and Harris County. The Big Barn fault showed no movement prior to February, 1987. After February, 1987 the rate of movement was two to three time that of other faults in the area, except for the Conroe fault (Norman and Britt, 1991).

Fault Number	Fault Name	Strike	Downthrown Side	Rate of Movement (in/yr)	Date
1	Long Point	N45-N75E	SE	0.5	
2	Brittmoore	N55-60E	SE	0.47	
3	Woodgate	N52E	SE	0.35	
4	Hardy	N45E	SE	0.24	
5	Lee	N53E	NW	0.27	
6	Jetero	N72E	NW	0.25	
7	Cantertrot	N75W	NE	0.22	
8	Navarro	N52E	SE	0.43	
9	Big Barn	N40E	SE	0	8/85-9/86
				0.64	2/87-9/87
10	Conroe	N55E	SE	0	8/85-2/87
				0.74	2/87-9/87
11	Grangerland	N83W	NE	N/A	

CHAPTER 2

2.1 REGIONAL GEOLOGY

The relevant regional geology of the Gulf Coast includes parts of Texas, Arkansas, Oklahoma and the Gulf of Mexico. Texas is underlain by Precambrian rocks that are primarily volcanic and intrusive igneous rocks that formed early in the Earth's history. The rocks are mostly buried; however, they are exposed in the Llano Uplift and in a few geographically isolated areas in Trans-Pecos Texas. These basement rocks are referred to as the Texas Craton. During the early Paleozoic, broad inland seas inundated the stable West Texas region, depositing widespread limestones and shales (Bureau of Economic Geology, 1992). The Texas Craton was bordered on the east and south by the Ouachita Trough, a deep-marine basin extending along the Paleozoic continental margin from Arkansas and Oklahoma to Mexico (Bureau of Economic Geology, 1992). Sediments accumulated in the Ouachita Trough until late in the Paleozoic Era when the European and African continental plates collided with the North American plate. Convergence of the North and South American plates during the assembly of Pangea in this area produced fault-bounded mountainous uplifts (the

Ouachita Mountains) and small basins filled by shallow inland seas that constituted the West Texas Basin (Bureau of Economic Geology, 1992).

The Gulf Coast geosyncline began with rifting of Pangea and deformation of the Paleozoic surface in the Early Mesozoic. The geosyncline served as a catch basin for sediments eroded from the North American plate. Down-warping and down-faulting proceeded further in response to the weight of sediment accumulation (Hosman, 1996). Faulting in this area has been active since the Mesozoic and is still occurring. Mesozoic deposition caused vast accumulations of sediments to form in the Gulf Coast geosyncline, which continued to deepen during the Jurassic (Hosman, 1996). Advances of Cretaceous seas left marine deposits as far as the northern limit of the Mississippian embayment (Hosman, 1996). Deposition expanded northward during the Cretaceous Period when the sea inundated the Mississippi embayment. The early Cenozoic Mississippi River flowed across East Texas, and a large delta occupied the region north of Houston. Smaller deltas and barrier islands extended southwestward into Mexico, very much like the present Texas coast (Hosman, 1996). In the Gulf Coast Basin, deeply buried Jurassic salt moved upward to form domes and anticlinal structures (Hosman, 1996). At present, Cenozoic strata are exposed throughout East Texas and in broad belts in the coastal plain that become younger toward the Gulf of Mexico. The isolated High Plains were eroded by several Texas rivers during and since the Pleistocene Ice Age, causing the

eastern margin to retreat westward to its present position. While the northern part of the continent was covered by thick Pleistocene ice caps, streams meandered southeastward across a cool, humid Texas carrying great volumes of water to the Gulf of Mexico. Those rivers, the Colorado, Brazos, Red, and Canadian, slowly entrenched their meanders as gradual uplift occurred across Texas during the last 1 million years (Hosman, 1996). Sea-level changes during the Ice Age alternately exposed and inundated the continental shelf. River, delta, and coastal sediments deposited during interglacial (high-sea-level) stages are exposed along the outer 80 kilometers of the coastal plain. Sea level reached its approximate present position about 3,000 years ago, and thin coastal-barrier, lagoon, and delta sediments have been continually deposited along the Gulf Coast (Hosman, 1996).

2.2 STRUCTURE

The structure of the Texas Gulf Coast is a broad homocline dipping gulfward. Some regional structural features that alter the general attitude and stratigraphy of the plain are the Sabine uplift, the East Texas basin, the San Marcos arch, and the Rio Grande embayment. In part, the physiography reflects the regional structure (Waters, McFarland and Lea, 1955). The Gulf Coast of Texas has many structural features such as listric normal faulting from the

opening of the Gulf of Mexico to salt dome intrusions and subsequent faulting (Hosman, 1996). The three major regional fault zones in proximity to the study area are the Luling-Mexia-Talco fault zone, the Balcones fault zone and the Mt. Enterprise fault zone. The Luling-Mexia-Talco and Mt. Enterprise fault zones are composed of grabens while the Balcones fault zone is comprised of en echelon faults.

Of the active faults in nearby Harris County, many of them have been correlated with subsurface faults (Van Siclen, 1967). Verbeek et al. (1978) recognized that these faults are growth faults. The main structures in Montgomery County are normal faulting and salt domes. The regional Gulf Coast structural features are formed by salt diapirism and glide and shear tectonics related to the opening of the Gulf of Mexico (Waters, McFarland and Lea, 1955). The Gulf of Mexico Coastal Plain contains sediments that glide downslope toward the coast (0.5° - 4.0°) (Figure 8). The shearing resistance must be small, but the detachment may form a thin shear zone or fault (Mourgue and Cobbold, 2006).

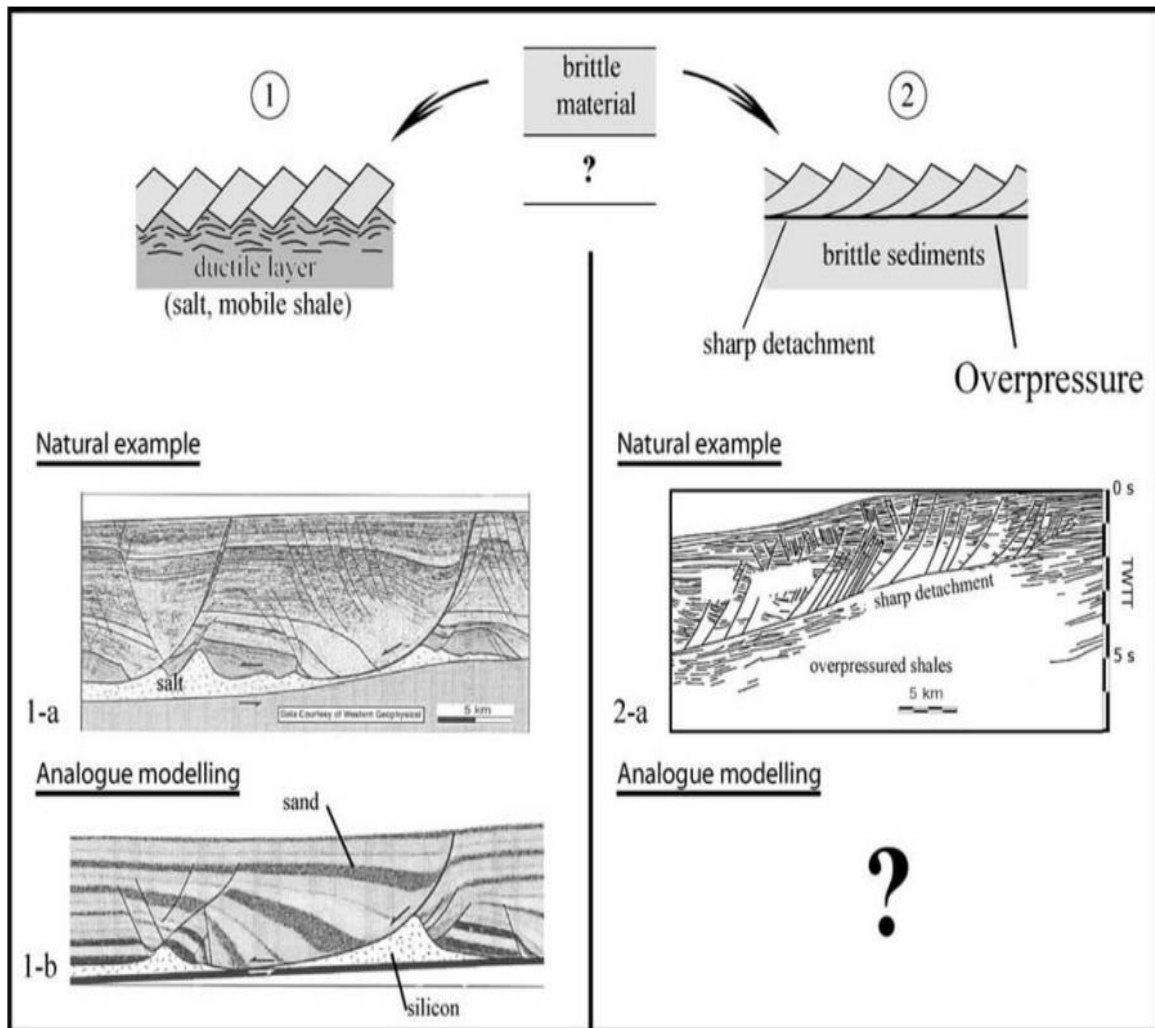


Figure 8. Glide and Shear Tectonic Models

This figure shows how faulting occurs over brittle materials and in ductile layers. Typical ductile layers are shale or salt domes and a natural example along with an analog model are shown. Faulting over brittle sediments tends to happen on over pressured shales where you have sharp detachment faulting occurring. A natural example is shown, but the authors did not have an analog model (Mourgue and Cobbold, 2006).

2.2.1 IAPETAN RIFTED MARGIN

During the late Precambrian to Early Cambrian the Iapetan rifted margin formed in the southeastern part of Laurentia. It is now covered by late Paleozoic Ouachita-Appalachian allochthonous rocks and Mesozoic-Cenozoic synrift and passive-margin strata of the Gulf Coastal Plain (Thomas, 2011). In southern Laurentia, the Alabama-Oklahoma transform fault intersects with the Blue Ridge strata and the Texas Transform fault intersects with the Ouachita and Marathon rift segments. This intersection outlined the Alabama and Texas promontory and the Ouachita and Marathon embayment (Thomas, 2011) (Figure 9). In Central Texas, the Waco uplift is a subsurface basement structure with significantly uplifted basement rocks relative to rocks beneath the leading edge of the Ouachita thrust belt. The Luling uplift, southeast of the Llano uplift has a similar geometry and composition as the Waco uplift and was interpreted to suggest an alignment of basement thrust ramp anticlines (Thomas, 2011).

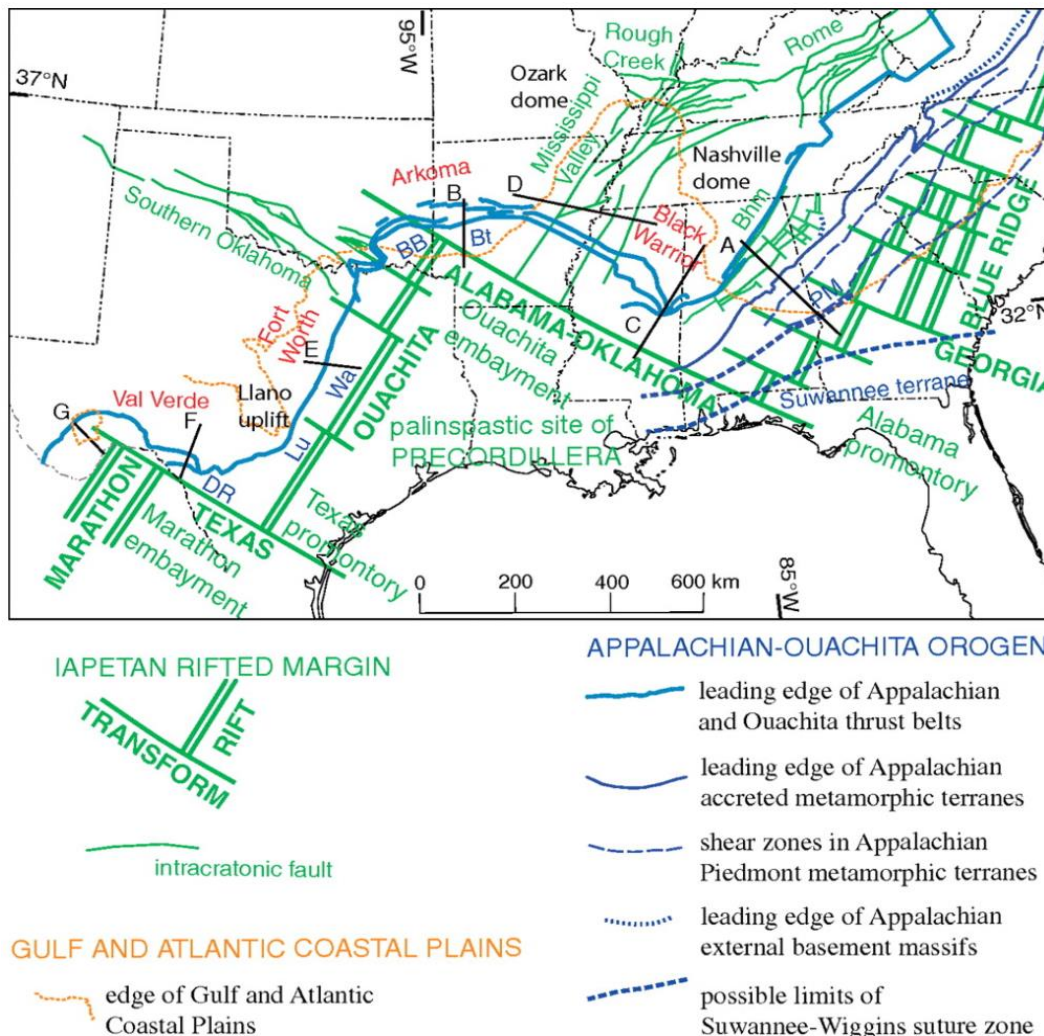


Figure 9. Palinspastically Restored Margin of Southern Laurentia

This figure shows the palinspastically restored Iapetan rifted margin of southern Laurentia, synrift intracratonic basement faults, and palinspastic site of Argentine Precordillera terrane. Intracratonic basement fault systems are labeled in green letters, abbreviation: Bhm—Birmingham graben. Locations of Ouachita-Appalachian basement uplifts (thrust-ramp anticlines) are shown by abbreviations in blue letters: DR—Devils River uplift; Lu—Luling uplift; Wa—Waco uplift; BB—Broken Bow uplift; Bt—Benton uplift; and PM—Pine Mountain internal basement massif. Locations of Ouachita-Appalachian late Paleozoic synorogenic foreland basins are shown by names in red letters. Locations of intracratonic basement domes are shown by names in black letters (Thomas, 2011). Black lines labeled A through G show locations of cross sections found in Thomas, 2011.

2.2.2 GULFIAN TECTONIC CYCLE

The Gulf of Mexico began forming in the Late Triassic to Early Jurassic Period (190 Ma) and continued until the Early Cretaceous period (132 Ma). The Gulf of Mexico basin formed through the down-warping of Paleozoic basement rocks during the break up of Pangea. These processes were a result of the opening of the North Atlantic Ocean and then the Gulf of Mexico basin in the late Triassic and Early Jurassic (Byerly, 1991; Hosman & Weiss, 1991). The exact kinematics of the opening of the Gulf of Mexico are still debated; however, the main stages of tectonic evolution are generally agreed upon. The main stages are: (1) Northwest–southeast Triassic continental rifting between North America, the Yucatan continental block, and South America (Marton and Buffler, 1994; Pindell and Keenan, 2009; Kneller and Johnson, 2011; Hudec et al., 2013; Eddy et al., 2014; Nguyen and Mann, 2016). (2) Syn-rift salt deposition occurred in the late Middle Jurassic Period (163-161 Ma). The opening of the oceanic crust in the center of the Gulf of Mexico caused the salt basin to separate into two basins. The Louann salt basin and the Campeche salt basin formed at the end of the Middle Jurassic Period (~152 Ma) (Hudec et al., 2013; Nguyen and Mann, 2016). (3) Ocean spreading and transform faulting occurred and rotated the Yucatan block 40° counterclockwise (Marton and Buffler, 1994; Pindell and Keenan, 2009; Nguyen and Mann, 2016). The spreading of the seafloor continued until the Early Cretaceous (~138 Ma) (Eddy et al., 2014; Nguyen and

Mann, 2016). After this time, the Gulf of Mexico began subsiding with passive margins that were covered by thick accumulations of clastic sediment (Marton and Buffler, 1994; Hudec et al., 2013; Nguyen and Mann, 2016). The tectonic stages of evolution of the Gulf of Mexico can be seen in Figure 10 below.

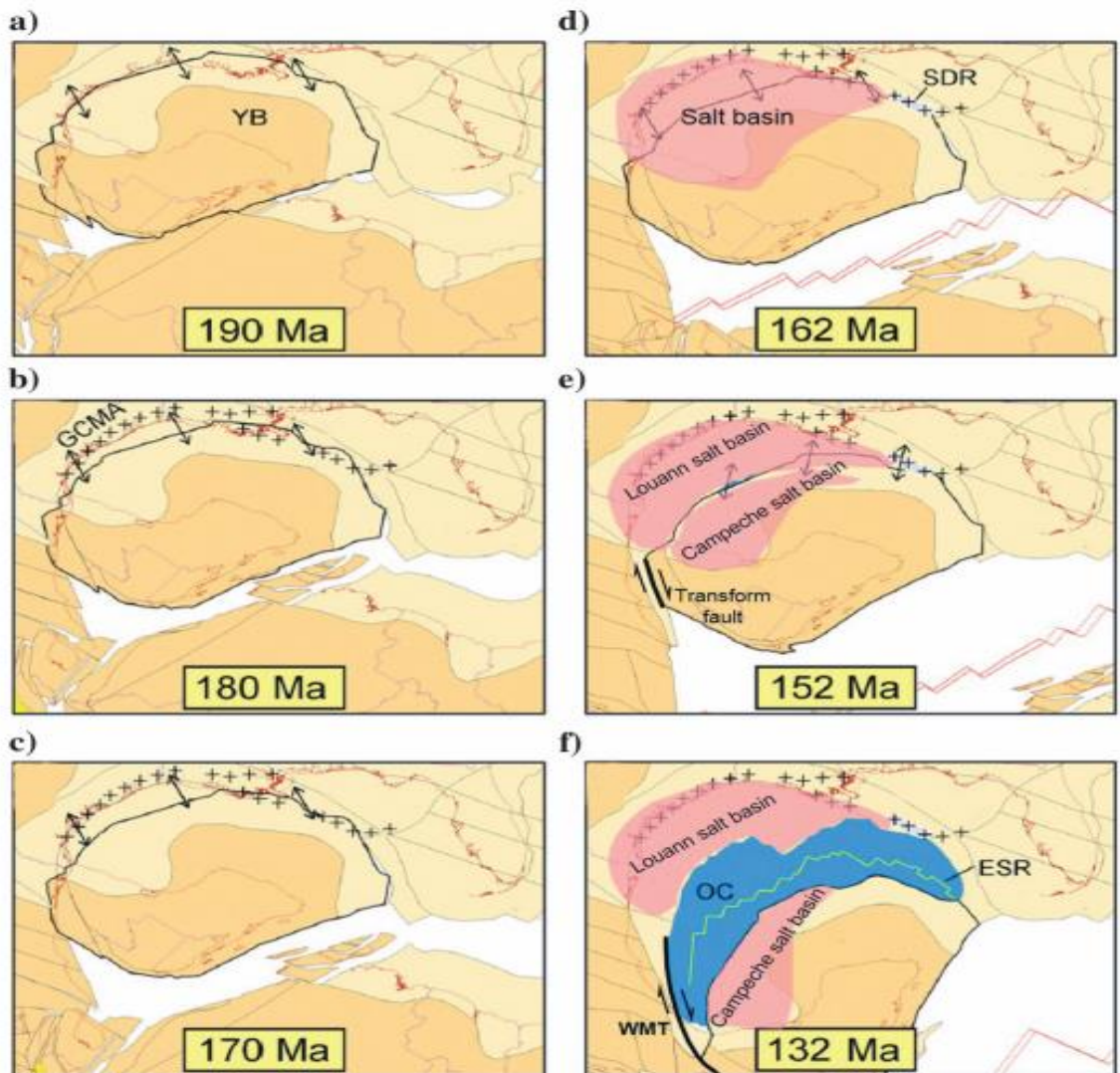


Figure 10. Tectonic Stages of the Evolution of the Gulf of Mexico

(a-c) Early continental rifting in the Late Triassic to Early Jurassic (190-170Ma) between North America and the Yucatan-South American Plates. The black crosses show a magmatic belt that erupted in the early stages of rifting. (d) In the Middle Jurassic, a layer of salt was deposited in the basin over the rifted continental crust. (e) Late Jurassic, the direction of extension changed from northwest-southeast to north-south as the Yucatan block rotated in a counterclockwise direction and formed the Western Main Transform along the continental margin of Mexico. The oceanic crust opened in the center of the Gulf of Mexico and separated the salt basin into the Louann salt basin and the Campeche salt basin. (f) Early Cretaceous sea floor spreading and strike-slip motion along the Western Main Transform stopped (Nguyen and Mann, 2016).

2.2.3 GULF COAST GEOSYNCLINE

The Gulf Coast geosyncline is a major structural feature located along the coast of the Gulf of Mexico. After Pangea broke apart, North and South America began spreading away from each other and the Gulf of Mexico Basin formed. This basin became a topographic low and filled with water. To the north and south of the basin, normal faults formed parallel to the coast. These normal faults caused the downthrown, southern portion of the Gulf Coastal Plain to dip toward the coast. Folding associated with the Ouachita orogeny formed the Gulf Coast geosyncline and formed a catch basin for subsequent sedimentation, and downfaulting continued in response to the weight of sediment accumulation (Hosman, 1996). The geosyncline continued to subside throughout Mesozoic and Cenozoic time. The Gulf of Mexico basin gained sediment through shifting alluvial source areas which provided deposits along unstable faulted shelf margins (McGookey, 1975; Winker, 1982). The geosyncline is defined by mainly Cretaceous and Tertiary beds dipping and thickening gulfward. The stratigraphic thickness of the geosyncline in Houston is at least 20,000 feet (Barton, Ritz and Hickey, 1933) (Figure 11). Other authors have concluded that stratigraphic deposits along the coastline are 50,000-60,000 feet thick (Baker, 1994).

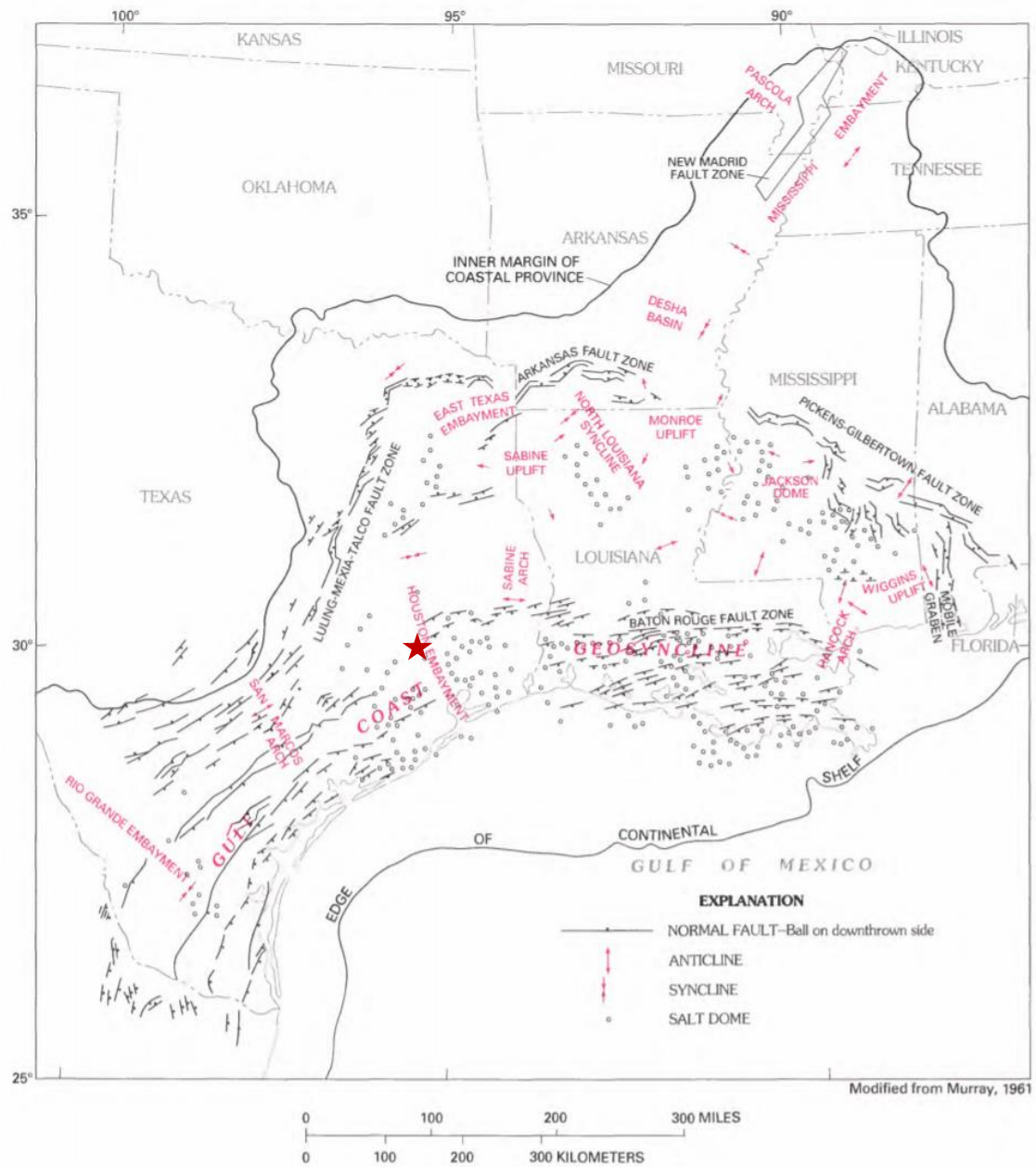


Figure 11. Gulf Coast Geosyncline

This shows the structural features associated with the Gulf Coast geosyncline. The study area is depicted as a red star and is located closest to the Houston Embayment on the Gulf Coast geosyncline (modified from Hosman, 1996).

2.2.4 THE SABINE UPLIFT

The Sabine uplift formed just northward of the Gulf Coast geosyncline and represents a structural high that formed during the Jurassic (Figure 12). The uplift was submerged during the Tertiary due to the deposition marine clay in the Midway group associated with a shallow marine environment. The Wilcox group forms the surface and has remained a structural high since the Tertiary (Lea, McFarland and Waters, 1955). There are also many structural elements superimposed upon the uplift, but they are not significant regionally.

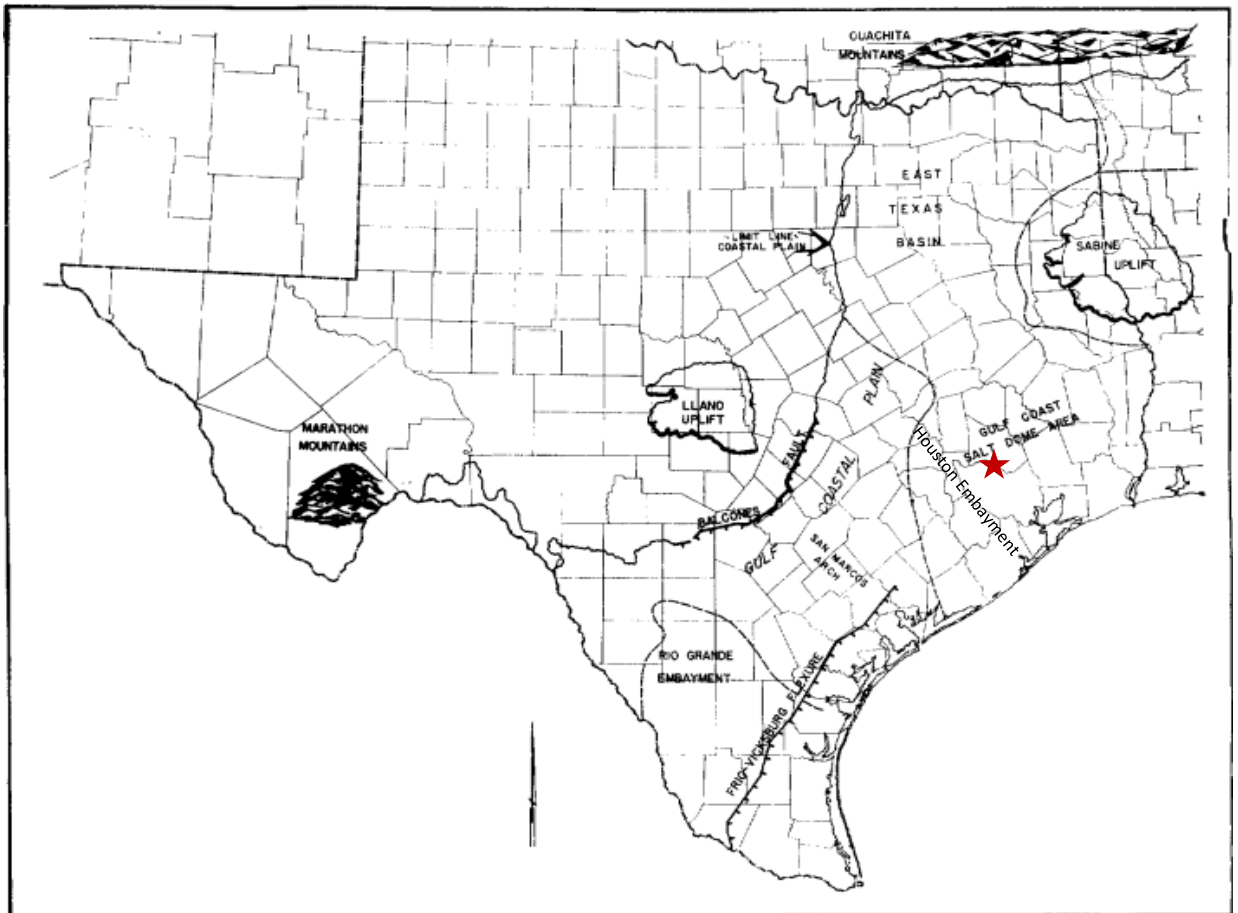


Figure 12. Regional Structures in the Texas Gulf Coast

This figure shows the primary regional structures within the Gulf Coast, including salt domes and nearby uplifts. The red star represents the approximate location of the study area (Modified from Lea, McFarland and Waters, 1955).

One of the major regional structures along the Texas Gulf Coast are normal faults. There are three major fault systems located near the study area and they are the Luling-Mexia-Talco fault zone, Balcones fault zone and the Mt. Enterprise fault zone (Figure 13).

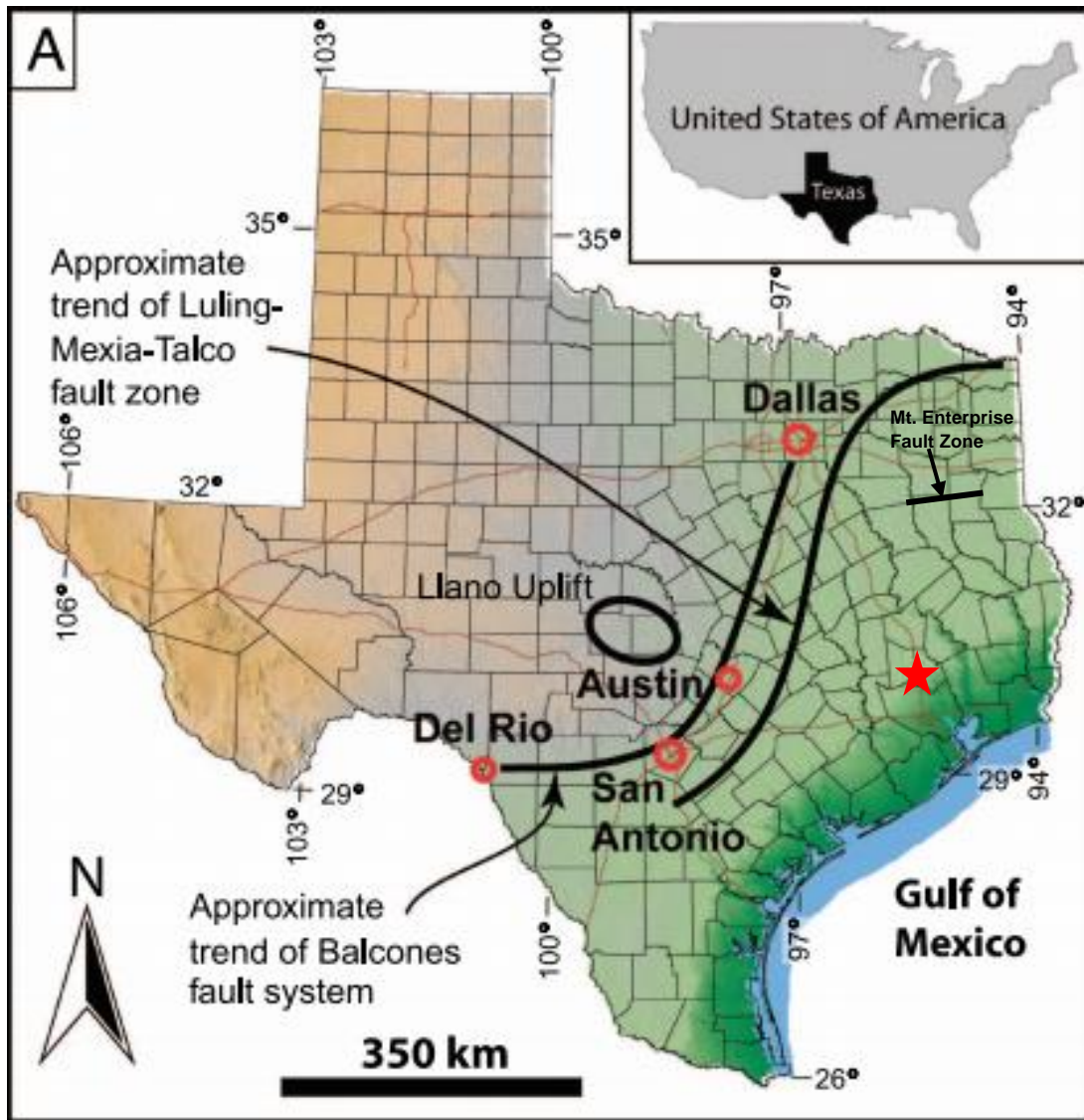


Figure 13. Major Regional Fault Zones

The Luling-Mexia-Talco fault zone, Balcones fault zone and Mt. Enterprise fault zone are shown with dark black lines that mark the northern extent of the Gulf of Mexico. These fault zones are located in central Texas near Austin and San Antonio and extend westward to Del Rio, northward to Dallas and east into Louisiana. The study area is represented by a red star (Modified from Ferrill and Morris, 2008).

2.2.5 LULING-MEXIA-TALCO FAULT ZONE

An important fault zone in the area is the Luling-Mexia-Talco fault zone which extends northeastward across southern and southeastern Texas (Hosman, 1996). In northeastern Texas the trend of the zone turns eastward. The major faulting episodes occurred during the Early Cretaceous and Miocene (Woodruff Jr., 1980). These faults are associated with the Gulf Coast geosyncline. The zone is a system of en-echelon grabens several miles across and normal faults (Hosman, 1996). The normal faults in the system mark the boundary between the Edwards plateau uplands and the Gulf Coast plains (Woodruff Jr., 1980). Strike-oriented growth faulting also occurs in zones of varying extent throughout the Gulf Coastal Plain. All are associated with subsidence of the Gulf Coast geosyncline, and at least some are still active. A few faults, mostly in the southeastern part of the Gulf Coastal Plain, are at approximate right angles to the general strike of the growth-fault system (Hosman, 1996). The reasons for the origin and orientation of these faults are not known but could be caused by salt movement because they mark the updip limit of the Louann salt (Hosman, 1996; Figure 14).

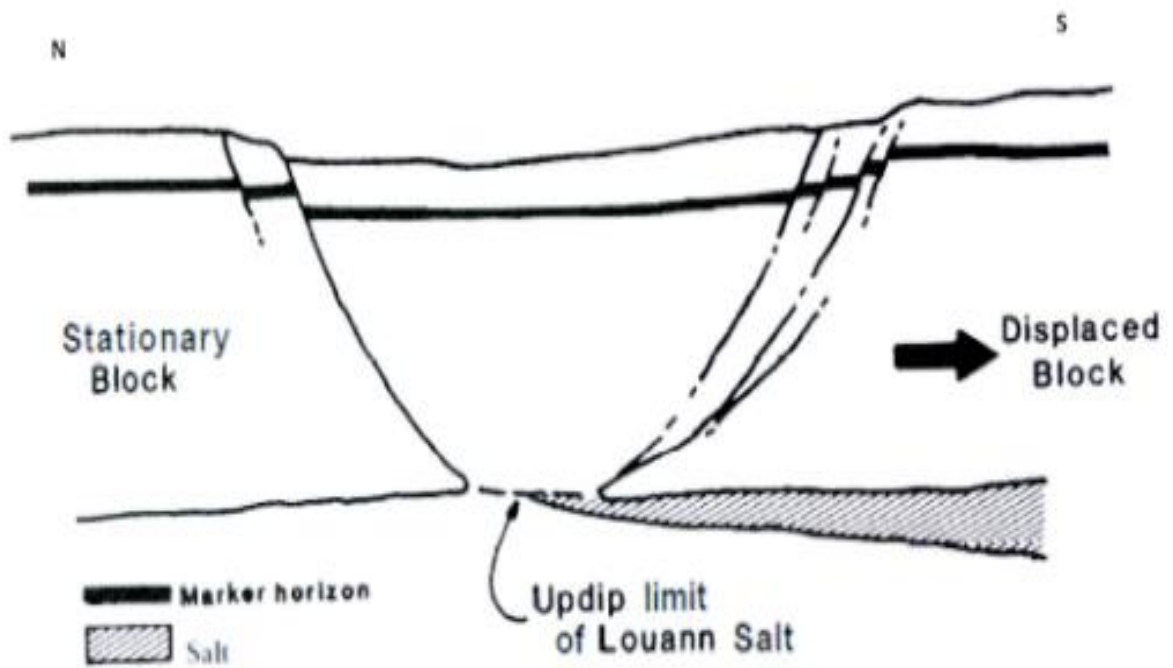


Figure 14. Cross Section of Mexia-Talco Graben

This figure shows the Mexia-Talco graben which is also the updip limit of the Louann Salt. The graben system was facilitated by the southward extension caused by salt gliding (Wood and Giles, 1982).

2.2.6 BALCONES FAULT ZONE

The Cretaceous Edwards Formation was deposited as a carbonate platform and forms the south and eastern edge of the Edwards Plateau. The Balcones fault system is a major, down-to-the-south, normal fault system that is found along the southeastern margin of the Edwards Plateau. Compared to the Luling-Mexia Talco fault zone, the Balcones fault zone has more pronounced faulting due to the softer strata found along the Balcones fault zone (Ferrill and Morris, 2008). The Balcones fault system is a line of normal faults along the northwestern margin of the Gulf of Mexico basin. The trend of the fault zone matches the trend of the buried Ouachita orogeny (Ferrill and Morris, 2008). A cross section of the Balcones fault zone can be seen in Figure 15.

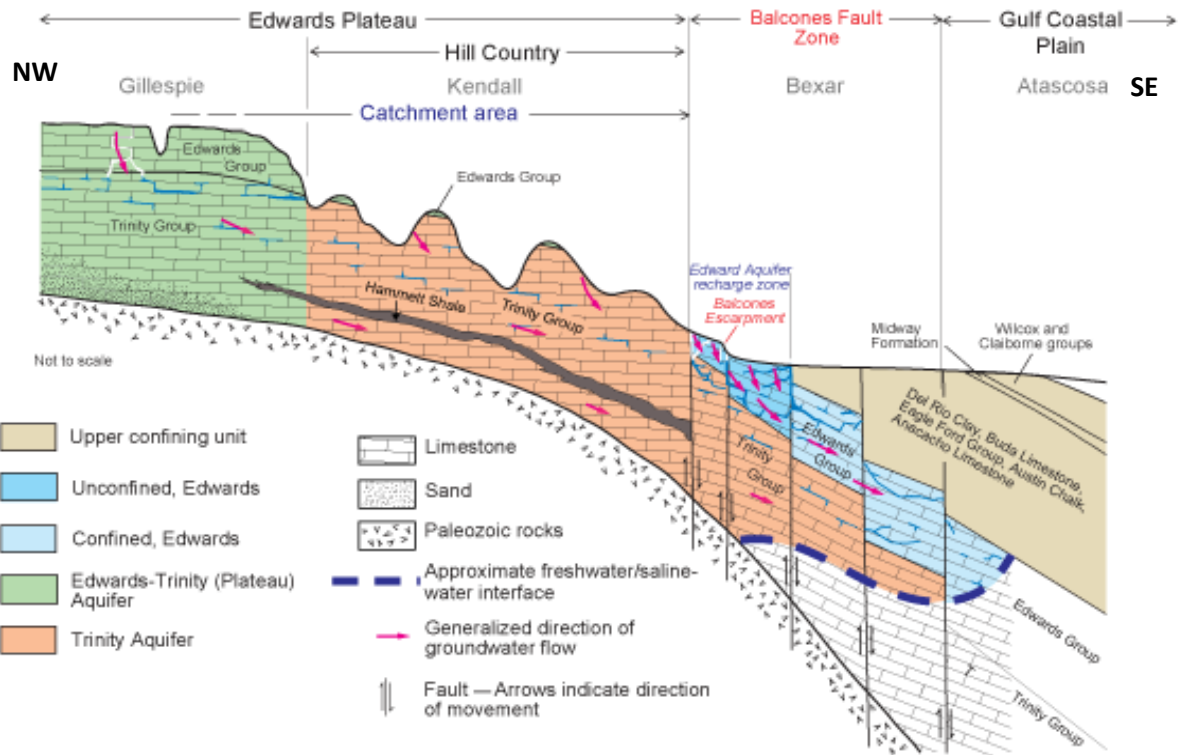


Figure 15. Cross Section of Balcones Fault Zone

This figure shows a cross section of normal faults within the Balcones Fault Zone. These faults offset the Trinity Group, Edwards Group along with the Upper confining unit. Groundwater flow patterns and aquifers are also shown (Modified from Barker and Ardis, 1996).

2.2.7 MOUNT ENTERPRISE FAULT ZONE

The Mount Enterprise fault zone is found northeast of the study area and consists of parallel and en echelon normal faults with a NE/SW trend and with dips of 35 to 60° northward or southward (Jackson, 1982). The Mount Enterprise faults are similar to the Gulf Coast growth faults but have the opposite sense of throw. The Mount Enterprise fault zone does not overly any major salt structures and is not related to the Angelina flexure or the growth of the Sabine Arch (Jackson, 1982). A cross section can be seen in figure 16.

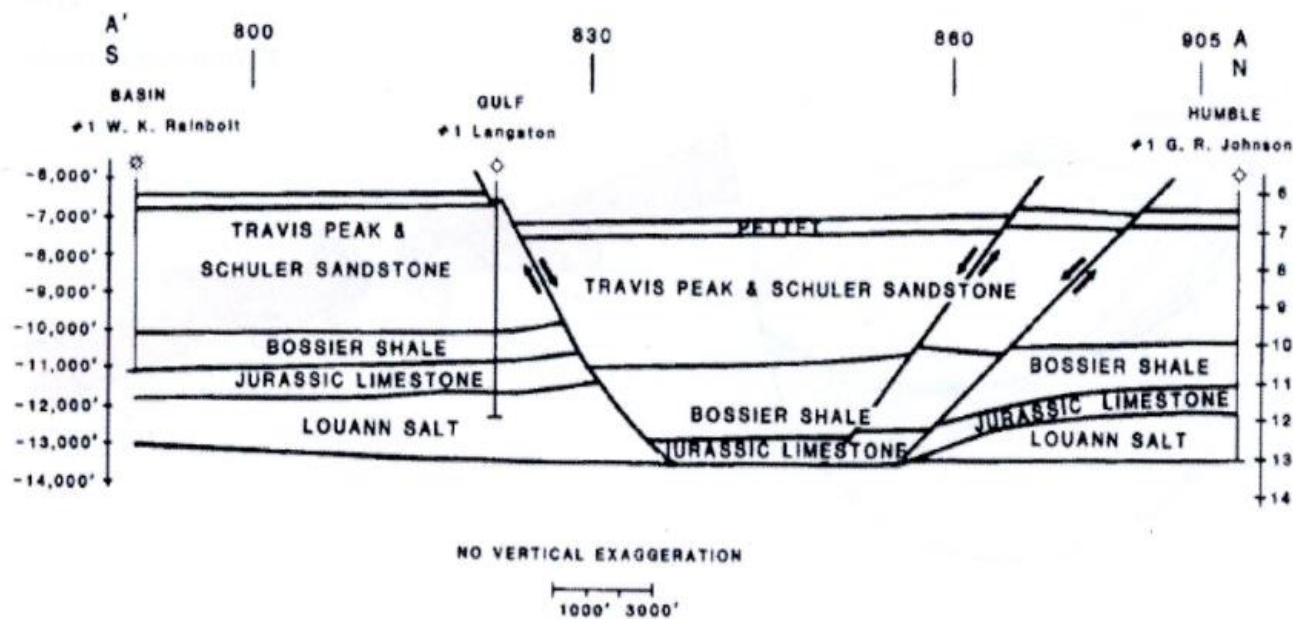


Figure 16. Cross Section of the Mount Enterprise Fault Zone

This figure shows the Mount Enterprise Fault Zone which is an east-west oriented graben that runs through southern Rusk County. There is a greater thickness of the Louann Salt in the southern portion of the graben which could have been caused by upwelling of salt by sediment load (Wood and Giles, 1982).

2.2.8 EAST TEXAS EMBAYMENT

The East Texas embayment and the North Louisiana syncline form a single major geosyncline that arcs around the northern half of the Sabine uplift (Figure 11). The initial deformation that produced this large regional depression was likely associated with the Ouachita orogeny. The Gulf Coast Geosyncline

has not received sedimentation since the withdrawal of the sea in the Tertiary (Hosman, 1996).

2.2.9 RIO GRANDE EMBAYMENT

The Rio Grande embayment in southern Texas is a more pronounced depression than the Houston embayment and these two embayments are separated by the San Marcos arch (Figure 11 and 12). The axis of the Rio Grande embayment trends east-southeast, whereas the axis of the San Marcos arch strikes more southeast. During the late Mesozoic uplift the Rio Grande embayment became a primary source of syntectonic sedimentation (Oldani, 1986). Tectonic sediment also accumulated in the embayment in the Oligocene when basin and range deformation was occurring (Oldani, 1986).

2.2.10 SALT DOMES

Salt domes are common in the Gulf Coastal Plain. Hosman says that the largest concentration of domes extends along the coast from the southeastern corner of Texas to the southeastern tip of Louisiana (Hosman, 1996). The salt domes formed from the Louann Salt and its age is estimated to range from

Triassic to Late Jurassic. Salt accumulation occurred in East Texas and incipient Gulf of Mexico basins from Triassic to the Middle Jurassic time (Garrison, 1973). Garrison postulated that the thick accumulations of salt led to a tectonically unstable area where there is a high degree of mobility. The plastic flow of bedded salt into pillows or similar structures began in the Late Jurassic and Early Cretaceous time in response to density differences between the salt and the accumulating overburden (Hosman, 1996). The pillows of salt moved upward in the form of diapirs, domes or ridges and gained and gave continuing relief from growing pressure of the overburden. Salt domes then grew penecontemporaneously with surrounding sedimentation. The domes grew and moved in a series of pulses of isostatic adjustments as changing equilibriums were met (Hosman, 1996). The underlying salt flowed toward the top of the dome and this process is known as the rim-syncline effect (Hosman, 1996). Faulting then formed adjacent to the dome (Figure 17). A cap rock overlies the salt domes and can show impurities in the salt that remained after salt dissolution by groundwater (Hosman, 1996).

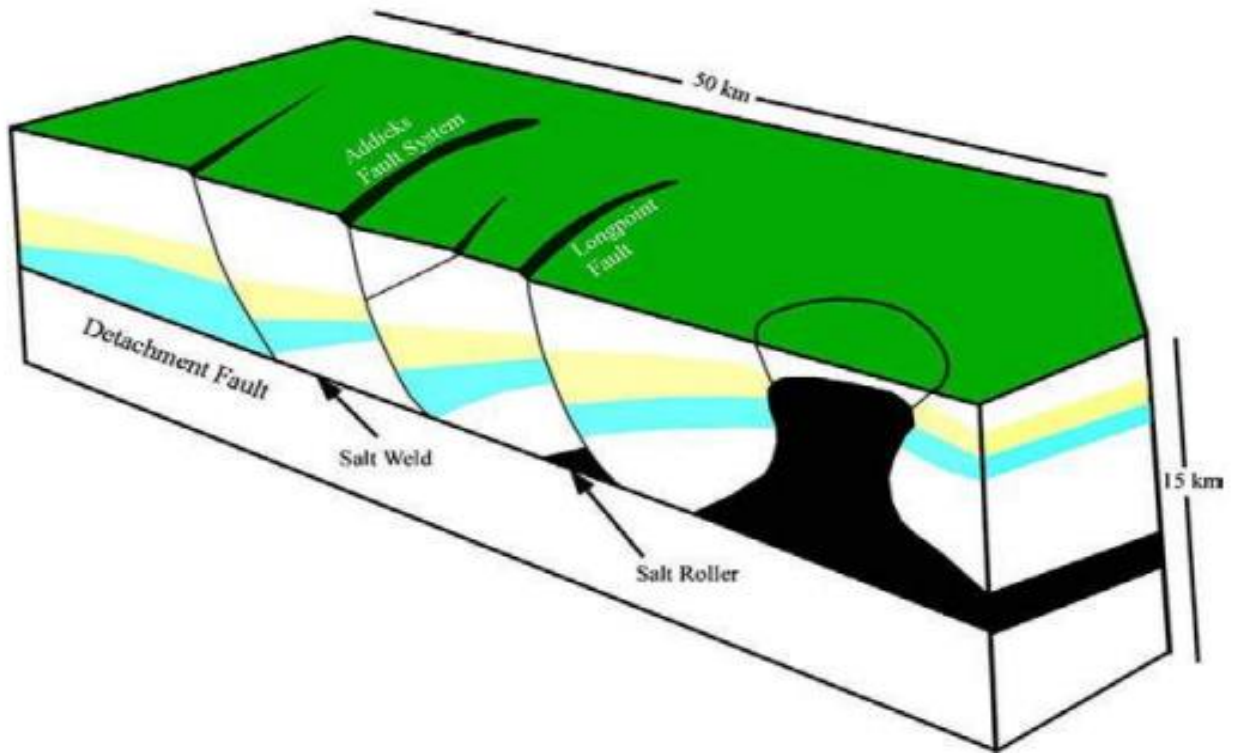


Figure 17. Faulting Around Salt Domes

This model shows the relationship between faulting and rising salt domes. This model is an analog for the faults found around salt domes in north Harris County, not far from the study area (Engelkemeir et al., 2010).

2.3 STRATIGRAPHY

The stratigraphy of the eastern Gulf Coastal Plain of Texas is very similar to the stratigraphy in other parts of the Gulf of Mexico. The following figure shows the stratigraphy of the Gulf of Mexico through the Cenozoic (Figure 18).

ERA	SYSTEM	SERIES	SW	SE	SW	SE	SW	SE				
			SOUTH COASTAL PLAIN (includes Rio Grande embayment)		CENTRAL COASTAL PLAIN (includes San Marcos arch)		EAST COASTAL PLAIN (includes East Texas Basin, Sabine uplift, and Houston embayment)					
CENOZOIC	Quaternary	Holocene	Alluvium		Alluvium		Alluvium					
		Pleistocene	Beaumont Formation		Beaumont Formation		Beaumont Formation					
			Lissie Formation		Lissie Formation	Montgomery Formation	Lissie Formation	Montgomery Formation				
						Bentley Formation		Bentley Formation				
					Willis Sand		Willis Sand					
	Tertiary	Pliocene	Goliad Sand		Goliad Sand		Goliad Sand					
		Miocene	Fleming Formation		Fleming Formation		Fleming Formation					
			Oakville Sandstone		Oakville Sandstone		Oakville Sandstone	Fleming Formation				
			Catahoula Tuff	Upper part of Catahoula Tuff subsurface	Anahuac Formation	Catahoula Tuff or Sandstone	Upper part of Catahoula Tuff or Ss. subsurface	Anahuac Formation	Catahoula Sandstone	Upper part of Catahoula Ss. subsurface	Anahuac Formation	Frio Formation
					Frio Formation			Frio Formation				Frio Formation
					Frio Clay	Vicksburg Fm. (subsurface)	Frio Clay	Vicksburg Fm. (subsurface)		Vicksburg Fm. (subsurface)		
		Oligocene	Jackson Group		Jackson Group		Whitsett Fm. Manning Clay Wellborn Ss. Caddell Fm.	Jackson Group				
			Eocene	Yegua Formation		Yegua Formation		Yegua Formation				
				Laredo Formation	Cook Mountain Fm.	Cook Mountain Formation		Cook Mountain Formation				
					Sparta Sand	Sparta Sand		Sparta Sand				
				El Pico Clay	Weches Formation	Weches Formation		Weches Formation				
					Queen City Sand	Queen City Sand		Queen City Sand				
				Bigford Formation	Reklaw Formation	Reklaw Formation		Reklaw Formation				
				Carrizo Sand	Carrizo Sand		Carrizo Sand					
	Paleocene	Indio Formation		Calvert Bluff Formation		Calvert Bluff Formation						
				Simsboro Formation		Simsboro Formation						
				Hooper Formation		Hooper Formation						
	Midway Group		Midway Group		Midway Group							

Figure 18. Stratigraphic Column of the Texas Gulf Coast

This figure shows the Stratigraphic Column of the Gulf Coast of Texas. The surficial lithologic units can be seen outlined in red. The main units in the study area are the Lissie Formation and the Willis Formation (Baker, 1994).

A stratigraphic atlas of the surface geology in the study area can be seen in Figure 19 below. The two primary units in the study area are the Lissie Sand and the Willis Clay.

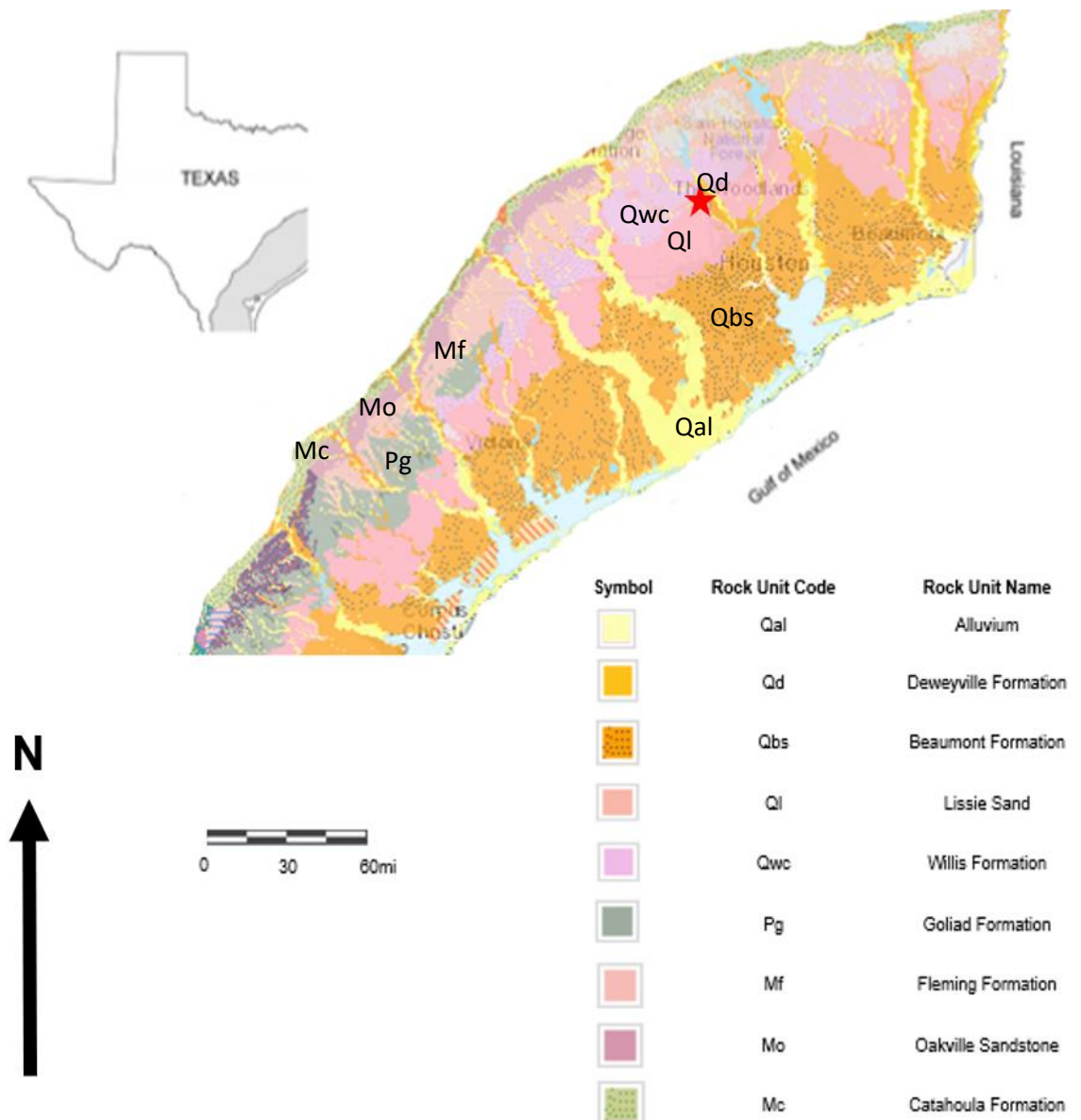


Figure 19. Stratigraphic Atlas of the Texas Gulf Coast

This shows surficial geology of Texas along with the outline of the Gulf Coast. The red star shows where the study area is located. Modified from USGS.

The study area specifically involves the eastern Gulf Coast Plain in Montgomery, Texas. The oldest sediments were deposited in the Paleozoic and include the Ouachita facies, but have been deeply buried. The youngest sediments were deposited in the Quaternary and include alluvium. Drilling downward, a well in this area would penetrate over 100 different stratigraphic units from the Mesozoic and Cenozoic eras (Baker, 1994). Baker postulated that these deposits are estimated to be 50,000-60,000 feet thick near the coastline and are disrupted by fault systems.

2.3.1 PRE-JURASSIC

Any knowledge of pre-Jurassic geology in the Gulf Coastal Plain is very limited, especially in the southern part of the area where the extreme depths of these strata place them beyond the interest of petroleum exploration drillers and often beyond the reach of their equipment. Paleozoic and Mesozoic rocks underlie Cenozoic coastal deposits at the surface (Waters, McFarland and Lea, 1955). No rocks from the Triassic have been found in the Texas Gulf Coastal plains, northern Mexico or Louisiana, but it is possible that they may be underneath the younger strata.

2.3.2 JURASSIC

Jurassic deposits underlie the inner margin of the Texas Coastal Plain but are not exposed. The principal rocks are sandstone, shale, limestone, dolomite, and evaporites, which suggest deposition under varied environments (Waters, McFarland and Lea, 1955). Gulfward tilting was nearly continuous although there were unconformities that indicate periods of uplift and erosion. Thickening of the marine facies suggests deepening of the East Texas basin during Late Jurassic to Early Cretaceous time. In the basin there are more than 5,800 feet of Jurassic sediments which pinch out before reaching the surface (Waters, McFarland and Lea, 1955). During this time the Cotton Valley group formed and extended from east Texas to Alabama. The Cotton Valley group consisted of sandstone, shale and limestone and now underlies the northern coastal plain of the Gulf of Mexico (Dyman and Condon, 2006).

2.3.3 CRETACEOUS

During the Cretaceous Period carbonates such as the Edwards Group, Glen Rose Formation, Georgetown Formation, Del Rio Formation, Buda Limestone, Eagle Ford Formation and the Austin Group were deposited in south-central Texas as a part of a regionally extensive carbonate-dominated sequence (Ferrill and Morris, 2008).

In the lower Cretaceous, sediments were deposited by a northwestward transgressing sea. This resulted in the deposition of Trinity, Fredericksburg, and Washita strata in the coastal province and further inland. The sediments reflect varied environmental conditions, but the dominant rocks are limestones in the upper part and clastics in the lower part (Waters, McFarland and Lea, 1955).

In the upper Cretaceous, the primary lithologies that were deposited were sandstone, shale, marl, and chalk. These beds rest on the Washita group throughout most of the Texas Coastal Plain and in the northeast, they are on older Comanche strata (Waters, McFarland and Lea, 1955). The Woodbine Group, described as having alternating layers of sandstone and shale is the oldest of the Upper Cretaceous groups in the Gulf of Mexico. The Woodbine has been traced in the subsurface as far south as Brazos and Grimes counties. The overlying unit is the Eagle Ford, which is absent on the Sabine uplift and is thickest in the East Texas basin. The Eagle Ford thins over the San Marcos arch and thickens southwestward to the Mexican border. The Austin group consists of chalk and marl over most of Texas, but in the northeastern part the dominant lithologic types are chalk, clay, and sand (Waters, McFarland and Lea, 1955). The thickness of the Austin group varies from 1,400 feet on the western flank of the Sabine uplift to more than 3,600 feet in the East Texas basin. Southwestward it varies in thickness from 1,900 feet on the San Marcos arch to more than 4,300 feet in the Rio Grande embayment (Waters, McFarland and Lea, 1955). The

distribution of the clastic Woodbine suggests deposition in a shallow basin with the maximum percentage of sandstone occurring on the west flank of the Sabine uplift. Volcanic activity outside Texas supplied large amounts of ash in northeast Texas during this time (Leah, McFarland and Waters, 1955).

The encroachment of the Midway Sea at the close of the Cretaceous Period began a succession of alternating marine and non-marine depositional cycles that lasted throughout the Paleocene and Eocene Epochs (Hosman, 1996) (Figure 20). This can also be seen through the varying lithologies present in the area. The marine interval during which sediments of the Midway Group were deposited lasted the entire Paleocene Epoch. This was the longest and most expansive of the Cenozoic depositional cycles (Hosman, 1995). The maximum point of withdrawal was the Gulf Coast geosyncline, and marine deposition there was continuous. Thus, a marine facies equivalent exists for the entire continental sequence (Hosman, 1996).

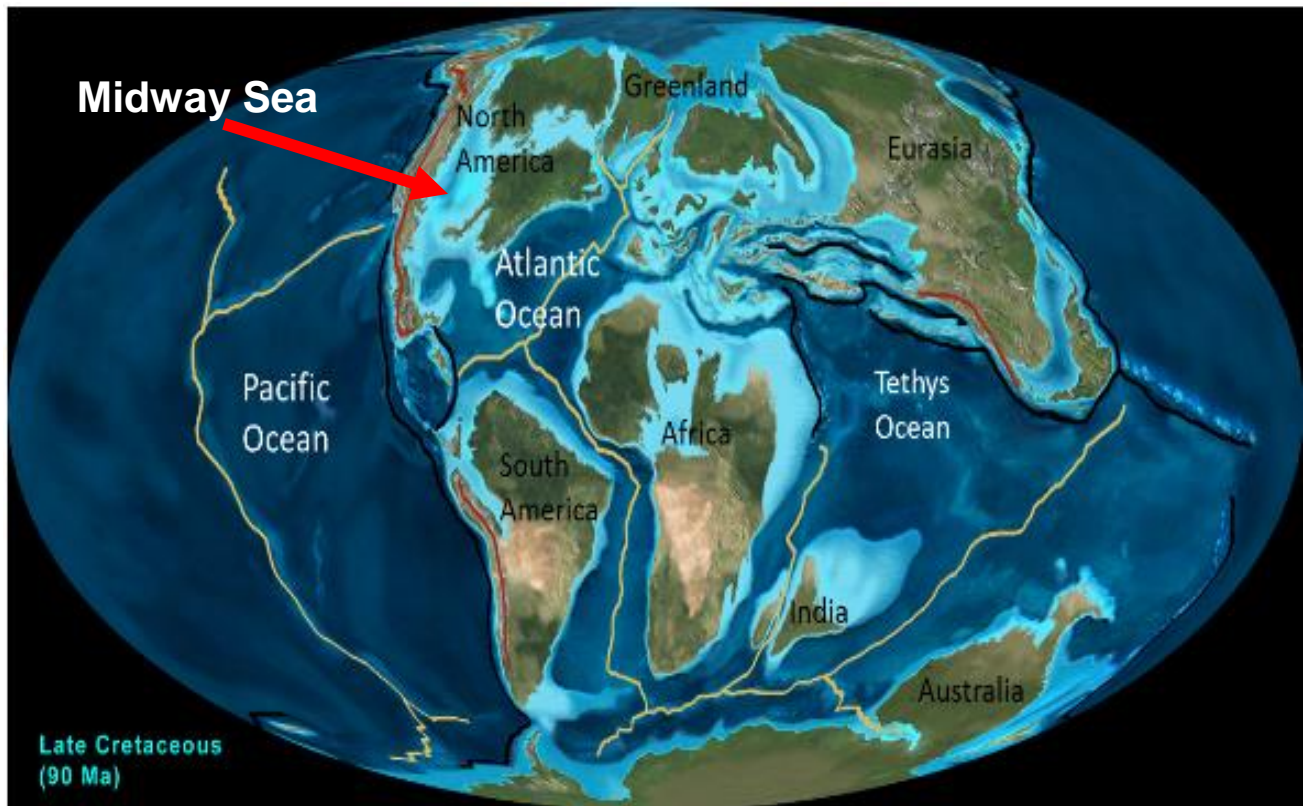


Figure 20. North American Intercontinental Seaway (Midway Sea)

This figure shows the intercontinental seaway that ran through North America during the Late Cretaceous Period (90 Ma) (Blakey, 2016).

2.3.4 EOCENE TO MIOCENE

Transgression and regression of the Midway Sea was followed by widespread deposition of Wilcox deltaic clastics which set the pattern for Eocene sedimentation (Lea, McFarland and Waters, 1955). Each of the Eocene groups crops out and extends from the Louisiana State line to the Mexican border. In

the subsurface of the Texas Coastal Plain, the Wilcox increases from 767 feet updip in Zavala County to nearly 7,000 feet downdip in Harris County (Lea, McFarland and Waters, 1955). Unconformably above the Wilcox is the Mount Selman Formation, which is divided into three members (Figure 18). The oldest is the marine Reklaw that thickens abruptly downdip across a zone of strike parallel normal faults in the San Marcos arch area, indicating a Wilcox flexure (Stoneham, 1953). The Queen City deltaic sand thickens from Polk County southwestward to more than 3,400 feet in McMullen County. This suggests that the source of Gulf Coastal Plain sediments has shifted from northeastward to northwestward. The fossiliferous Weches is the top member of the Mount Selman. The Sparta Formation thickens from the southwest toward the east into South Louisiana where it is an important oil-producing formation. It is overlain by the glauconitic fossiliferous brown shales of the Cook Mountain which in turn is overlain by the marine sands and shales of the Yegua. The Jackson marly shales and marine sandstone layers are the youngest Eocene group (Figure 18). Eocene sediments thicken gulfward and the predominant down dip lithology is shale. One well in Goliad County penetrated 10,000 feet of Eocene section without reaching the Midway, and other areas may be underlain by greater thicknesses (Stoneham, 1953).

The only strata of Oligocene age in the Texas Coastal Plain are beds forming a marine wedge overlying the Jackson and underlying the lower Catahoula-Frio sandstone (Figure 18).

The Miocene sediments of Texas primarily consist of ashy clay, shale, and sand. Miocene aged strata are the most productive units in the Gulf of Mexico (Hentz and Zeng, 2003). Southward-flowing streams transported heavy loads of sediments and volcanic material and the ultimate deposition took place in marshes, lagoons, and along beaches forming barrier islands and deltas, which approached or were on the continental shelf (Berryhill et. al, 1987). In ascending order, the Miocene units are: lower Catahoula-Frio, marine Catahoula, upper Catahoula, Oakville, and Lagarto (Berryhill et. al, 1987; Figure 18). Miocene sediments thicken greatly gulfward and in the subsurface it is difficult to establish the upper and lower boundaries of the Oakville and Lagarto Formations. The Catahoula group is 3,600 feet thick in Jackson County and 5,300 feet in Refugio County (Berryhill et. al, 1987). Many of the major down-to-the-coast faults show a greater thickness of Miocene on the downthrown side. This thickening indicates movement contemporaneous with deposition. In the Gulf Coast salt-dome area these fault zones are less prominent and local structural features are more generally related to salt movement (Berryhill et. al, 1987).

2.3.5 PLEISTOCENE AND HOLOCENE

On the surface, the primary formations found in the study area were the Pleistocene aged Lissie Sand Formation and Willis Clay Formation (Figure 18). The Pleistocene gravels were also found in the study area and are associated with the stream channels of the Coastal Plain. Recent sediments have been deposited along the coast as sand dunes, beach sands, terrace material and alluvium. In part, these units extend out under the Gulf of Mexico. The continental shelf narrows from 13 miles at the Louisiana-Texas line to 50 miles at the Mexican border (Lea, McFarland and Waters, 1955).

2.3.5.1 LISSIE FORMATION

Pleistocene deposits units constituted the last major depositional episodes in the northwestern Gulf Coast Basin. The Pleistocene highstand fluviodeltaic progradation deposited the Lissie Sand and terminated during pre-Holocene sedimentation. The early phase of the Lissie deposition was initiated by a sudden flexing of the coastal area which produced an even sheet of gravel, sand, sandy clay, and much ferruginous material in the form of concretionary nodules and cementing material (Metcalf, 1940). The second phase of the cycle began when the streams started to in-trench into this plain, and to erode and transport the interior portions of the Lissie toward the coast. This process gradually developed

channels which cut deeper into the up-dip phases of the Lissie and into older formations (Metcalf, 1940). The type locality is at the town of Lissie, in Wharton County, Texas. The Lissie Formation (Pleistocene) consists of thick beds of sands with lens-shaped bodies of gravel, interspersed with clay beds (Doering, 1935). The maximum outcrop thickness for the Lissie Formation is estimated to be about 600ft. Lissie sediments consist of reddish, orange and gray, fine-to coarse-grained and cross-bedded sands, and include abraded fossils and lentils of gravel of varied composition. In the subsurface, Lissie floodbasin sediments are bluish and greenish gray (Solis, 1981). Doering also says that the slope of the top surface of the Lissie is about 5 feet per mile, while that of its base, which is the top of the Willis, averages about 20 feet per mile. This discordance in rate of dip gives the Lissie a coastward thickening of about 15 feet per mile (Doering, 1935). At the surface, the Lissie Sand was found to cover 30% of Montgomery County (USGS, 2018).

2.3.5.2 WILLIS FORMATION

The Willis Formation is primarily composed of clay and secondarily composed of silt. The major lithologic constituents are coarse-to-fine grained detrital sediments with some gravels intermixed. The gravels formed from channel facies and the formation itself was orange-brown colored, gravelly, coarse-to-fine sand with lenses of red, sandy silt and gray clay that is approximately 30-200 feet thick (Moore and Wermund, 1993). The type locality for the Willis Clay is Willis, Texas which is approximately 10 miles north of the study area. At the surface, the Willis Clay covers 50% of Montgomery County (USGS, 2018). Stratigraphic studies of the Willis Formation have been very limited and future work could be done to expand upon the stratigraphy of the formation and its depositional history.

CHAPTER 3

3.1 GRAVITY THEORY

Gravity surveys are conducted to determine variations in the gravitational field of the Earth. Isaac Newton first theorized about gravity in 1687 and formulated Newton's Law of Universal Gravitation shortly after (Lowrie, 2007). Newton's Law of Universal Gravitation states that the force of attraction between two masses (m_1 and m_2) is directly proportional to the product of their masses and is inversely proportional to the square of the distances between the two masses (Telford, et. al., 1990; Okocha, 2016). This can be defined by the following equation:

Equation 1
$$F = \frac{Gm_1m_2}{r^2}$$

G is defined as the universal gravitational constant $6.673 \times 10^{-11} \text{m}^3\text{kg}^{-1}\text{s}^{-2}$, m_1 and m_2 are two masses in kilograms and r is the distance between the centers of the masses.

Gravity is not constant throughout the Earth because the Earth is not a perfect sphere and is not made of a homogenous material. The main factors that influence gravity measurements are: elevation, latitude, topography, tidal

influence and density variations in the surface of the Earth (Telford, et. al., 1990; Okocha, 2016).

Gravity measurements are typically measured in two ways: absolute and relative gravity measurements. Absolute gravity measurements determine the absolute gravity at any place while relative gravity measurements consist of measuring the change in gravity from one place to another (Lowrie, 2007).

Absolute measurements of gravity are classically conducted with a pendulum. Gravitational acceleration can be determined by measuring the time of an oscillating pendulum (Telford, et. al., 1990; Okocha, 2016). More modern methods of determining gravitation acceleration are based on observations of free falling objects. The absolute value of gravity can be determined by fitting a quadratic to the position of the object versus time (Lowrie, 2007). Modern equipment uses a Michelson interferometer to accurately measure the change of position of a free-falling object. A simplistic model of the modern free-fall method can be seen in Figure 21. Absolute gravity methods are usually not practical for field surveys because the absolute gravity measurements need to be conducted over a smaller area than relative gravity measurements.

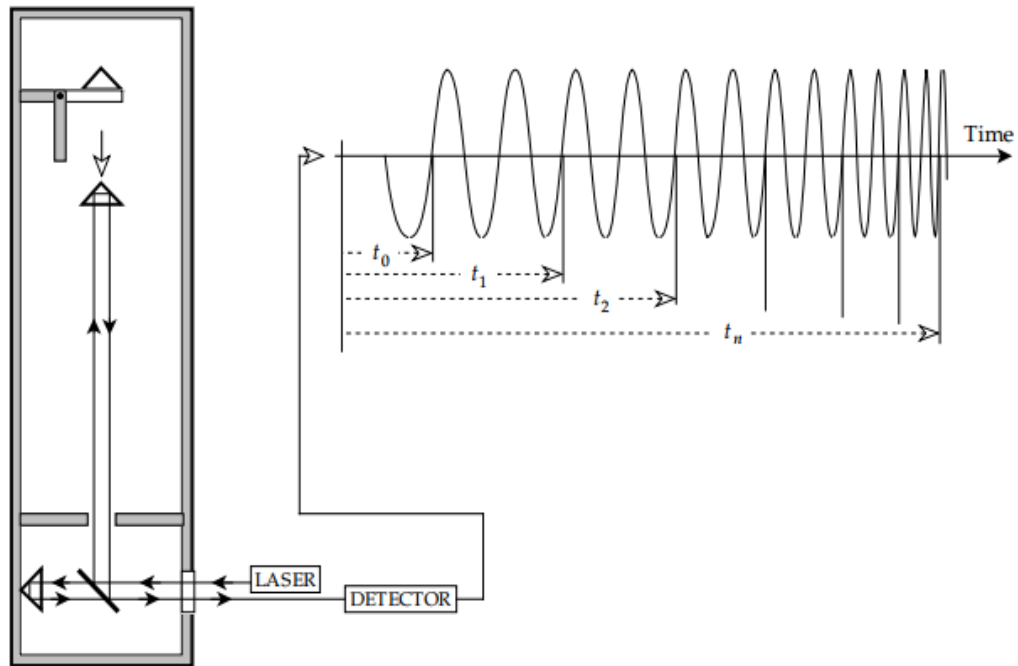


Figure 21. Modern Free-Fall Method for Determining Absolute Gravity

Absolute measurements of gravity can be conducted using the free-fall method. A laser beam is split along two paths to form a Michelson interferometer. The horizontal path is a fixed length while the vertical path is reflected off a corner cube retroreflector. The corner cube retroreflector is released at a known time and falls freely in an evacuated chamber to reduce air resistance. The detector determines the position of the corner cube retroreflector and the time it takes to fall (Lowrie, 2007).

The second method of measuring gravity is through relative gravity measurements. A gravimeter is typically used in these surveys and is described as a very sensitive balance (Lowrie, 2007). The most basic gravimeter is called a stable type gravimeter and is comprised of a mass “ m ” that is suspended from a spring with a length “ s_0 ”. The force of gravity weighing down on the spring

causes the spring to stretch to a new length “**s**”. The change of length in the spring is proportional to the restoring force of the spring and the value of gravity. The elastic constant of the spring “**k**” must also be known and is usually provided by the manufacturer of the gravimeter (Lowrie, 2007; Equation 2). This can be defined by the following equation:

Equation 2 $F = mg = -k(s-s_0)$

Where the force of gravity in a gravimeter is defined by the elastic constant of a spring multiplied by the change in length of the spring (Lowrie, 2007).

Modern gravimeters have replaced the basic stable type gravimeter with more sensitive types that have an additional force that acts in the same direction as gravity and opposes the restoring force of the spring. This causes an unstable equilibrium and is realized in the design of the spring. If the length “**s₀**” can be made as small as possible, then the restoring force will be proportional to the physical length of the spring instead of its extension (Lowrie, 2007). The LaCoste-Romberg gravimeter first introduced the *zero-length spring* and is still used in most modern gravimeters (Lowrie, 2007). An example of a modern gravimeters that utilize the *zero-length spring* is the CG-5 Scintrex Autograv.

At any given time, a gravimeter can only measure absolute gravity or the change in gravitational variation, because it is not possible to measure both at the same time. Absolute and relative gravity instruments can only measure the

maximum of the total gravitational fields, which is the vertical component (Telford, et. al., 1990; Okocha, 2016).

3.1.1 APPLIED GRAVITY CORRECTIONS

Gravity surveys measure the gravitational field in the Earth and are a passive method for geophysical investigation. Passive geophysical techniques do not input any kind of energy into the ground; instead these techniques measure physical properties naturally occurring in the subsurface. Since the Earth is an oblate spheroid instead of a perfect sphere there are variations in gravitational acceleration that differ from one location to another. Gravity corrections remove unwanted components of gravity readings that are collected in the field. Various gravity corrections are applied to the raw gravity dataset and are discussed further below.

3.1.2 DRIFT CORRECTION

Drift corrections account for changes caused by the instrument itself. If a gravimeter is placed at a stationary point and readings are taken over a period of time the gravity readings will not be consistent. The CG-5 Autograv used in this study automatically corrects for tide and drift on measured gravity readings. Tide corrections account for changes in gravity due to the movement of the sun and

the moon. Tidal corrections are also dependent on time (Telford, et. al., 1990; Okocha, 2016).

The CG-5 Autograv gravimeter is equipped with a sensor made of non-magnetic fused quartz that is not affected by the magnetic field of variation of less than ten times the Earth's magnetic field $\pm 0.5\text{mT}$ (Scintrex, 2012; Okocha, 2016). The quartz elastic system is a stable operating environment that allows for long term drift of the sensor to be predicted accurately and the software applies the drift corrections to be less than 0.02 mGal per day. It is recommended that a 12-24 hour instrument drift calibration be carried out on the instrument prior to doing any field surveying.

3.1.3 ELEVATION CORRECTION

Elevation corrections are needed to correct for topographic effects resulting from the difference in elevation between the base station and the field stations. Typically, there are three types of elevation corrections applied during gravity corrections: Free-air, Bouguer and terrain corrections.

(a) Free-air correction: This corrects for variations in elevation from one field station to another. Newton's Law of Universal Gravitation (Equation 1) shows that gravity decreases with the square of the distance. This means that gravity readings will change when the gravimeter is raised or lowered; because

of this, the gravity data must be reduced to a datum in order to compare gravity readings taken at various elevations within the study area. When the elevation increases, the observed gravity readings are decreased by a vertical gradient of 0.3086 mGal/m (Telford, et. al., 1990; Okocha, 2016). The Free-air correction is added to the observed gravity data if the field station is above the datum and is subtracted if the observed gravity data is below the datum. The datum used in this study was the elevation of the base station because it had a lower elevation than all of the field stations in the study area. Since all elevation values were above the datum, they were added to the measured gravity readings. All elevation values for this study were extracted from LiDAR. Free-air corrections (mGal) were calculated using the following equation:

Equation 3 Free-air correction (FAC) = 0.3086 h

Where h is defined as the elevation in meters (Telford et. al., 1990, Okocha, 2016).

(b) Bouguer correction (BC): Another type of elevation correction applied to the observed gravity data was the Bouguer correction. The Bouguer correction removed the effect of rock density between the measured gravity point and the reference datum. The mass effect, or density of the rock causes measured gravity to be greater at higher elevations than at lower elevation. Pierre Bouguer first applied this type of correction to his work by using an assumed horizontal

slab with an average density of rock that was added to his observed gravity measurements (Telford, et. al., 1990; Okocha, 2016). The equation for the Bouguer correction is shown below:

Equation 4 Bouguer correction (BC) $S = 0.4193\rho h$

Where “ ρ ” is the average density of the surrounding Bouguer slab and “ h ” is the elevation in meters. An average rock density value of 2.65g/m³ was assigned to the Bouguer slab based on the geologic composition (sand and silt) of the study area (Telford et. al., 1990, Okocha, 2016).

(c) Terrain correction: The terrain correction accounts for the effect of topography by considering the irregularities in terrain from one location to another. Topographic highs that are located above the elevation of the gravity base station exert an upward force on the gravimeter, which decreases the gravitational acceleration. Valleys and topographic lows that are below the gravity base station fails to apply a downward force on the gravimeter (Telford, et. al., 1990; Okocha, 2016). Without terrain corrections, readings taken on top of a mountain would have much higher gravity readings than those taken in a valley because there is a vast difference in the amount of material beneath the gravimeter between both locations. Topographic highs and lows effect gravity readings, so terrains corrections must be made to account for these variations. Since the study area was in the Gulf Coastal Plain the topography is characterized by flat-low lying topography, so terrain corrections were not

necessary for this study. Gravity corrections for each survey site can be seen in Appendix A.2.

3.2 ELECTRICAL RESISTIVITY THEORY

Electrical resistivity can be defined as “the electrical resistance per unit length of a unit cross-sectional area of material” (Bates and Jackson, 1984). Electrical resistivity is measured in ohm-m (Cardimona, 2002). Ohm’s law describes the relationship between resistance, the change in surficial voltage and the current transmitted into the subsurface by electrodes.

The relationship is shown in the equation:

Equation 5
$$R = \frac{\Delta V}{I}$$

(R) is the resistance value, (ΔV) is the change in voltage at the surface and (I) is the current (Ball et. al., 2004).

Direct electrical current is propagated in rocks and minerals by electrolytic means and electronic conduction occurs where free electrons are available (Rucker, et. al., 2010). Electrical resistivity methodology injects an electrical current (I) into the Earth through one pair of electrodes (transmitting dipole) and

measures the resulting voltage potential (V) across another pair of electrodes (receiving dipole) (Rucker, et. al., 2010). Resistance can be defined as the amount of current flowing through a material and can vary depending on materials and dimensions. For example, a copper wire would have less resistance than a lead wire of the same dimensions and a short thick wire would have less resistance than a long thin wire (Mussett and Khan, 2000; Majzoub, 2016) (Equation 2 and 3). These equations are shown below:

$$\text{Equation 6 } \text{resistance, } R = \text{resistivity } (\rho) \times \frac{\text{length}}{\text{area of cross-section}}$$

$$\text{Equation 7 } \text{resistivity, } \rho = \text{resistance } (R) \times \frac{\text{area of cross-section}}{\text{length}}$$

The purpose of electrical resistivity surveying is to measure the distribution of resistivity in the subsurface. Certain geologic parameters such as lithology, soil content, water saturation and porosity influence the resistivity measurements (Loke, 1999; Majzoub, 2016). Electrical resistivity can be measured through multi-electrode resistivity techniques or through capacitively coupled resistivity techniques. The OhmMapper was used in this study to image the shallow subsurface structures and to delineate the surficial lithologic unit. The OhmMapper computer console was worn by the operator and the dipole cables

were towed behind the operator. The main operating principal of the OhmMapper is constant-current that is capacitively-coupled. Capacitively coupled resistivity (CCR) is a method that uses a set of cables or capacitive plates instead of metal stakes in the ground (Figure 22). When CCR is used, a voltage is applied to the conductor inside the CCR transmitter and an electric charge forms between the conductor and the ground (Yamashita, et. al., 2004). Insulation separates the ground and conductor. In a CCR system, two cables are used for the transmitter dipole and two cables are used for the receiver dipole. The Earth acts as half of a capacitor while the cable acts as the other half of the capacitor. The insulating jacket around the cable acts as the dielectric that separates the two halves of the cable-earth capacitor. An AC current passes through a capacitor and a DC current is blocked. In a CCR resistivity meter an AC current is applied to the cable, which then passes through the earth-cable capacitor into the ground. At the receiver side, the AC voltage is measured on the receiver cables (Geometrics, Capacitively Coupled Resistivity).

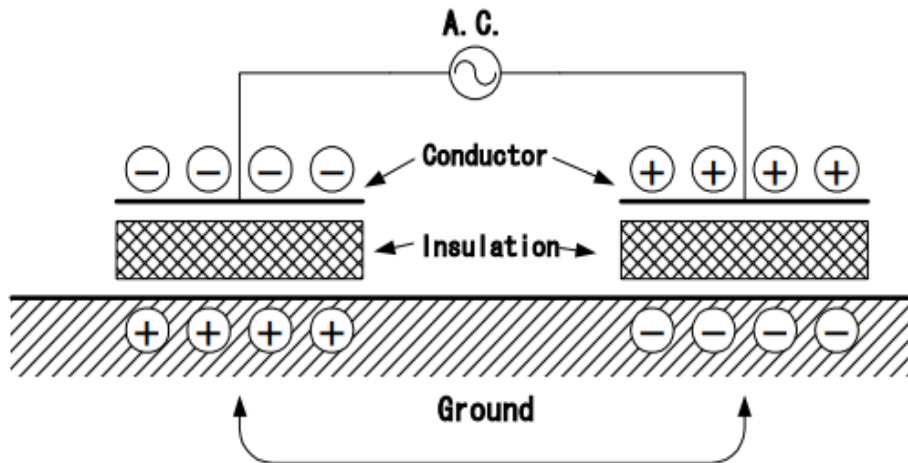


Figure 22. Conceptual Model of Capacitively Coupled Resistivity

The conceptual model for capacitively coupled resistivity where a voltage is applied to the conductor inside the transmitter and an electric charge forms between the conductor and the ground. An insulation is used between the ground and the conductor (Yamashita, et. al., 2004).

The SuperSting resistivity meter measures electrical resistivity by placing electrodes into the ground and the current traveling from one electrode to another is measured with a resistivity meter. For 1-D traditional electrical resistivity surveys, four electrodes are placed in the ground with a fixed distance between the electrodes (Figure 23). A current is then injected into the ground and the differences in voltage is measured by two potential electrodes. Apparent resistivity can be calculated from the voltage (V) and current (I) values. This “apparent” resistivity value is a calculated resistivity based on the geometry of the electrode configuration and is not the “true” resistivity (Loke, 1999; Majzoub,

2016). True resistivity must be found using an inversion processing software, such as EarthImager 2D.

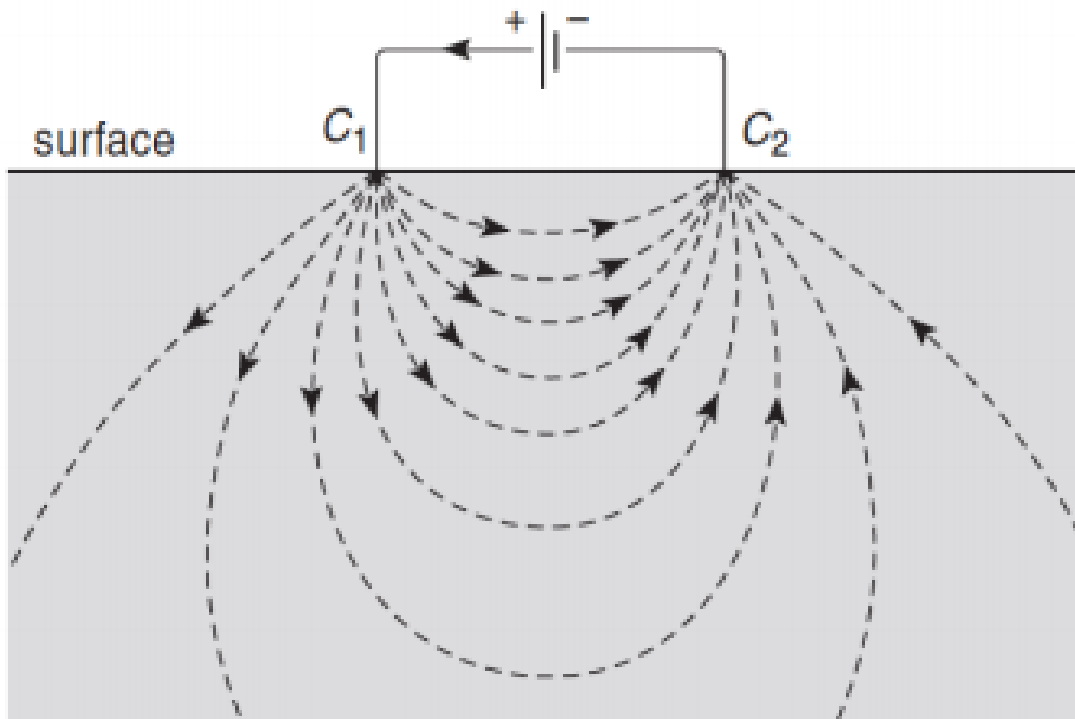


Figure 23. Electrical Resistivity Current Flow Paths

Simplified model of the current flow paths between two electrodes placed a few centimeters into the ground for an electrical resistivity survey. Modified from Musset and Khan, 2000.

1-D surveys can be time consuming, so two-dimensional (2-D) surveys are more commonly used. 2-D surveys can take a large quantity of measurements in a single reading (100-1000) compared to 10-20 readings in a 1-D survey. 3-D surveys give the most accurate data but are much more time consuming and costly than 1-D or 2-D surveys (Loke, 1999; Majzoub, 2016).

Electrical resistivity surveys are also dependent on the type of array used in the survey. While there are many arrays that can be used, the most common are Wenner, Schlumberger and dipole-dipole arrays.

The Wenner array positions four electrodes at a fixed interval and is connected to a resistivity meter. The electrode spacing is increased progressively throughout the survey and measurements are taken repeatedly. The Wenner array is typically more sensitive to vertical variations in resistivity than horizontal variations in resistivity (Mussett and Khan, 2000; Majzoub, 2016) (Figure 24, Section A). The Schlumberger array configuration is similar to the Wenner array, but the “**P**” potential electrodes are more closely spaced while the “**C**” current electrodes are moving symmetrically and progressively farther apart. Since the “**P**” potential electrodes are fixed, the electrodes do not have to be moved as often (Loke, 1999; Mussett and Khan, 2000; Majzoub, 2016) (Figure 24, Section B). The gradient array is similar to the Schlumberger array, but is less commonly used. (Figure 24, Section C). The most commonly used array in electrical resistivity surveys is the dipole-dipole array because it can be used to find many different anomalies with high accuracy. The current electrodes and potential electrodes are separated by a spacing marked as “**a**”. The ratio between the “**C**” current electrode and the “**P**” potential electrode is marked as “**n**”. Typically, the “**a**” spacing is fixed while the “**n**” factor is increased to increase the depth of investigation of the survey (Loke, 1999; Majzoub, 2016) (Figure 24, section D).

As the “n” factor gets larger, the resolution of the survey gets poorer. This is one of the main disadvantages of the dipole-dipole array.

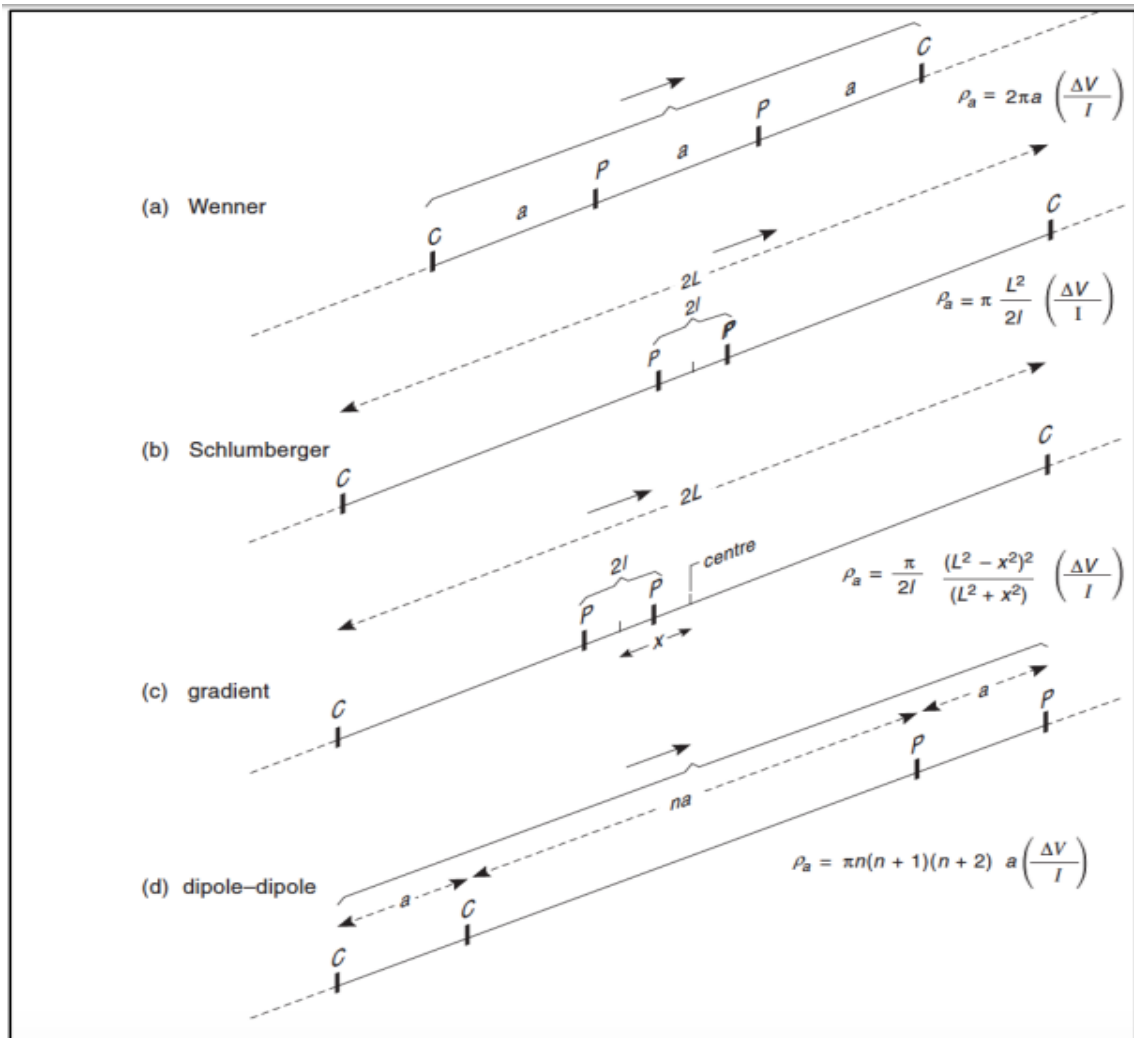


Figure 24. Common Electrical Resistivity Array Configurations

The most common electrical resistivity array configurations are Wenner, Schlumberger, gradient and dipole-dipole arrays. **C** is the current electrode and **P** is the potential electrode. Current travels from the **C** current electrode while resistivity is measured by the **P** electrode (from Mussett and Khan, 2000).

The differences in resistivity readings on a 2D pseudosection between the different arrays can be seen below in Figure 25.

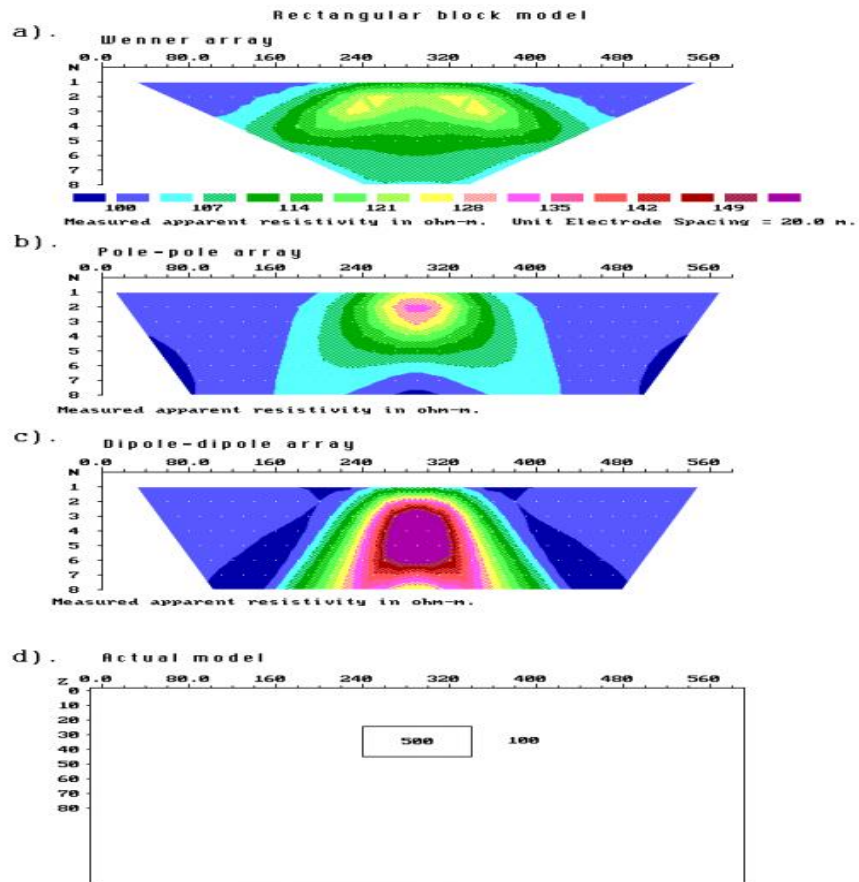


Figure 25. Apparent Resistivity for 2D Pseudosections for Various Arrays

The apparent resistivity for a 2D pseudosection over a rectangular block differs for the Wenner, Pole-pole and Dipole-dipole array. The Wenner array does not clearly define the block and projects the block to be wider than it is. The Pole-pole array defines the block more clearly than the Wenner array but underestimates the size of the block. The dipole-dipole array defines the block better than the other arrays even though it overestimates the horizontal depth of the block (Loke, 1999).

When selecting an array configuration for an electrical resistivity survey it is important to consider the size of the target along with the shape, depth and

resistivity contrast between the surrounding rocks (Mussett and Khan, 2000; Majzoub, 2016). The dipole-dipole array was used in this survey due to its high resolution and multi-channel capability.

CHAPTER 4

4.0 METHODOLOGY

Geophysical research was conducted on the Big Barn fault in Montgomery County, Texas. A CG-5 gravity meter was used to measure gravity and an TR4 OhmMapper and an R2 SuperSting resistivity meters were used to measure electrical resistivity. Field observations were first completed to determine areas with visible surface deformation. Broken up roadways that occurred within the trend of the fault and displayed a noticeable decrease/increase in elevation were examined. A Brunton compass was used to determine the trend of fault scarps. A Brunton compass is a clinometer that has hand level capabilities and is commonly used to determine the trend and dip of regional geologic structures.

Gravity data was acquired using the CG-5 Autograv and was used along various roadways that bisect the fault line. The CG-5 Autograv has a resolution of 1 microGal with a standard deviation of <5 microGals. The gravitational force exerted on the mass inside the instrument is balanced by a spring and an electrostatic restoring force (Scintrex, 2008). Since faults commonly juxtapose

rocks of different densities, gravity surveying can be a viable tool for the identification and detection of subsurface faults (Hatherton and Hunt, 1968).

Traditional electrical resistivity with a dipole-dipole array was used for both the capacitively coupled and multi-electrode electrical resistivity surveys. Data was first collected from the OhmMapper with a TR4 setup. Electrical resistivity was also collected using a Super Sting R2 resistivity meter.

4.1 GRAVIMETRY METHODOLOGY

In this study gravity data was collected along traverses that were perpendicular to the suspected fault line. The *Scintrex* CG-5 Autograv gravimeter was used in this study. The CG-5 Autograv has a sensing element that is based on a fused quartz spring system. The spring had a spring coefficient of -130 mGal / $^{\circ}$ K. This coefficient allowed the spring to become stronger as the temperature increased. The spring itself was protected from ambient temperature, so that it maintained its spring temperature constant to within 0.5 mK under normal operating conditions (Okocha, 2016; Scintrex, 2012). The gravimeter had an electric tilt sensor built into it that automatically compensated for errors in instrument tilt during measurements. The CG-5 Autograv applied real time tidal corrections based on the geographic location and the time zone entered by the operator. A seismic filter was also incorporated into the CG-5

Autograv which removed micro-seismic noise due to locally induced shocks (Okocha, 2016; Scintrex, 2012).

Measurements taken from the CG-5 Autograv provided information pertaining to the density of the rocks underneath the surface. Variations in gravity are due to lateral changes in the density of subsurface rocks. These variations are very small and are typically measured in milligals (mGal). The CG-5 Autograv also had a microprocessor-based automated gravity meter >8000mGal without reset. The reading resolution was 0.001 mGal with a standard deviation <5 (Okocha, 2016; Scintrex, 2002).

A Trimble NOMAD was used as a handheld computer with an integrated GPS receiver for navigation. The unit used Marvell PXA320 XScale 806 MHz processor and Windows Mobile 6.1 software. It was also integrated with quadband GSM GPRS/EDGE and GPS (WAAS / SBAS) capability (Okocha, 2016; Trimble, 2011). The main feature used on the Trimble NOMAD was the GPS. The GPS was used to determine exact coordinates of field stations throughout the survey (Figure 26).



Figure 26. Trimble NOMAD GPS Unit

The Trimble NOMAD handheld GPS Unit was used throughout the survey to accurately determine the location of every field station.

4.1.1 LiDAR

LiDAR (Light Detection and Ranging) was used in this survey to determine the elevation at every field station in order to make terrain corrections. LiDAR is a remote sensing technology that illuminates a target area with a laser and analyzes the reflected light in order to measure vertical distances (Okocha, 2016). The LiDAR data was collected in 2008 using Merrick's ALS50 Phase 2 sensor and the survey had a 1-meter resolution. The raw data was verified in MARS software for complete coverage of the project area. The Houston-Galveston Area Council contracted with Merrick & Company to fly the study area, which exceeded 3,500 square miles. The purpose of collecting the LiDAR data was for numerous GIS applications including flood modeling and prevention along with general educational purposes. The dataset was in an .laz file format and it contains elevation estimated values (in meters) using LiDAR technology.

4.1.2 DATA COLLECTION AND PROCESSING

Gravity data was collected using the CG-5 *Scintrex* Autograv and field surveys were conducted from May to August, 2017 (Figure 27). A local gravity base station was established and was visited before and after every day of field surveying. Local base station visitations were necessary to ascertain the degree of accuracy of the automatically applied drift corrections. The gravimeter was

programmed to collect three gravity readings per gravity station which were collated together. Prior to field surveying, a walk-through was done at every field site to determine the maximum length of surveying and other survey parameters. The gravity surveys were conducted perpendicular to the fault line in order to show a change in gravity from one side of the fault to the other. The survey stations at every field site started at the upthrown side of the fault and extended past the fault to the downthrown side of the fault.

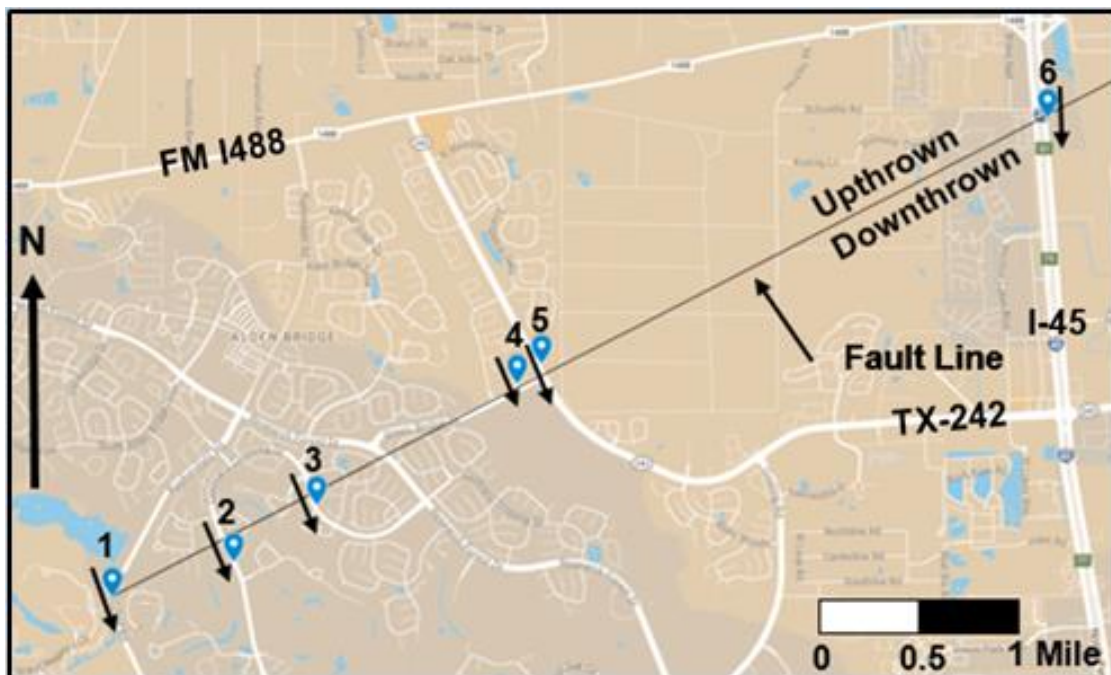


Figure 27. Gravity Field Survey Lines

This shows the 6 field locations for the gravity studies conducted in this survey. The survey lines were conducted perpendicular to the fault line and went from the upthrown to the downthrown side of the fault. Map made in Google MyMaps.

The survey line lengths were at various lengths due to the presence of anthropogenic features at each field site (Table 2). Planned survey lines were adjusted where necessary to make accommodations for busy roadways, dense forests and other obstructing features. An example of the field setup can be seen in Figure 28.

Table 2. Gravity Field Site Information

The following table shows the various line lengths for each of the 6 field sites examined in this survey.

Field Site	Line Length (m)	Station Spacing (m)	Number of Station Readings per Field Site
1	150	25	7
2	90	15	7
3	150	25	7
4	125	25	6
5	200	25	9
6	200	25	9



Figure 28. Field Setup of Gravimeter

The CG-5 Gravimeter was used in this study to complete field work. In this picture the surveyor is leveling the gravimeter by adjusting the dials at the bottom of the stand. The right figure shows the faceplate of the CG-5 Autograv (Scintrex, 2012).

All relative gravity readings measured for this survey were tied to a pre-established absolute gravity base station. The absolute gravity base station was located at latitude N 29° 44.2' and longitude W 95° 25.1'. This absolute gravity base station is located southwest of downtown Houston (Figure 31). The absolute gravity information of the base station was retrieved from the International Gravimetric Bureau website, <http://bgi.omp.obs-mip.fr/data->

products/Gravity-Databases/Reference-Gravity-53-Stations (Figure 29). This absolute base station is the closest one to the study area and it is an open and easily accessible. The absolute gravity was measured in July of 1967 and was found to be 979283.720 mGal with an estimated accuracy of ± 0.1 mGal. A local gravity base station was also established and was visited before and after every survey to ensure accuracy of the gravimetry data.

Gravity Base Station: 002701, g (microgals) = 979283720

GRAVITY BASE STATION			
LATITUDE	29° 44.20' N	(1)	STATION DESIGNATION
LONGITUDE	95° 25.10' W	(1)	HOUSTON
ELEVATION	18.40	METERS (1)	COUNTRY/STATE
REFERENCE CODE NUMBERS		ADOPTED GRAVITY VALUE	
ACIC 0270-1			
IGC 08295B			
OW 18			
		ESTIMATED ACCURACY	DATE
		± 0.1 mgals	MONTH/YEAR
			July/1967
DESCRIPTION AND/OR SKETCH			
<p>The station is southwest of downtown Houston at the northeast corner of Branard St. and Argonne St., at the former Hall-Sears Co. (2424 Branard St., also formerly occupied by Houston Technical Lab and Electro Tech International Co.), near the center of the building, east of the reception room, in the former lunchroom, at the west wall, about two meters south of the northernmost of two doorways in the west wall, on the tile floor.</p> <p>Station is monumented with a USAF Gravity Disk. A USC&GS Gravity Disk is set vertically 0.3 meters south of the northwest corner of the building, 0.3 meters above the ground. (1)</p>			
REFERENCE SOURCE			
(1) 02733			

ACIC HQ FORM 0-415

<http://bgi.omp.obs-mip.fr/data-products/Gravity-Databases/Reference-Gravity-Stations>

Figure 29. Absolute Gravity Base Station

Information about the absolute gravity base station used in this study is shown.

4.2 CAPACITIVELY COUPLED RESISTIVITY METHODOLOGY

A multichannel OhmMapper was used that had one transmitter and four receivers (TR4). The OhmMapper consists of transmitter electronics and batteries along with two transmitting dipole cables. The transmitter was towed by a non-conductive tow link that was connected to the receivers. The receivers consisted of the transmitter electronics, batteries and dipole cables. The received voltage level was converted into a digital signal by an optical wand and was transmitted to the data logger that was carried by the operator. The data logging console (DataMapper) was attached to the operator at the waist (Figure 30). The dipole-dipole array was selected for this survey because the data is plotted in a pseudosection with each measurement having apparent resistivity data plotted at the midpoint between two poles and a depth half the distance between two poles (AGI, 2005). The main advantage of the dipole-dipole array is its high resolution and multi-channel capability.

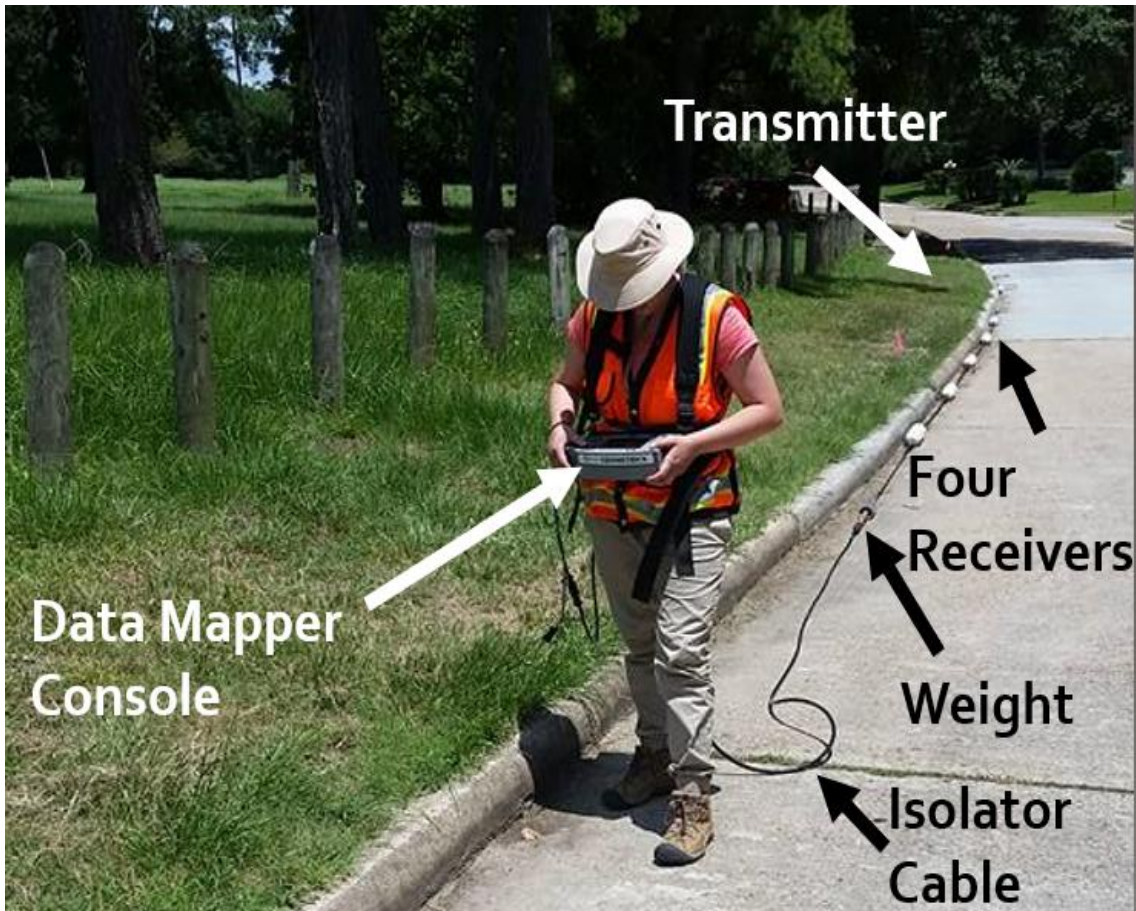
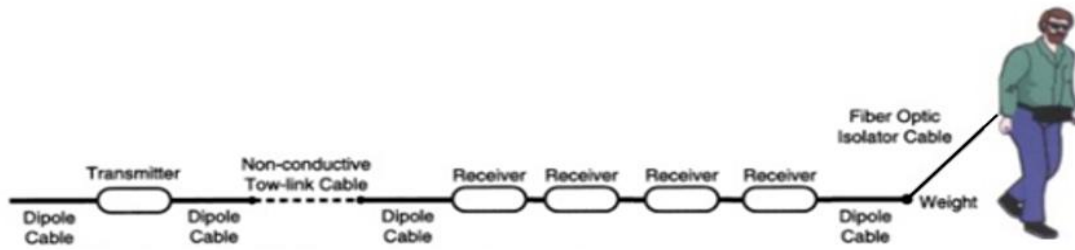


Figure 30. Field Setup for OhmMapper

This study used the TR4 setup which had one transmitter and four receivers. The transmitter had dipole cables on either side of it and a non-conductive tow-link cable that attached another dipole cable to the four receivers. The last receiver was attached to a dipole cable that attached to a weight that then attached to a fiber optic isolator cable. The fiber optic isolator cable was attached to the DataMapper that was worn at the waist of the operator (Modified from Geometrics Operation Manual, 2001).

The specifications for the OhmMapper resistivity meter include the main operating principle, operating range, cycle rate, data storage capacity, transmitter specifications and receiver specifications (Table 3).

Table 3. OhmMapper Specifications

Specifications for the OhmMapper include operating principle, operating range, cycle rate, data storage, transmitter specifications and receiver specification. A TR4 setup was used in this study which used one transmitter and four receivers.

Principle	Constant-current, capacitively coupled, dipole-dipole resistivity
Operating Range	From 3 to 100,000 Ohm-meters
Cycle Rate	Selectable data logging up to 2 scans/sec
Data Storage	2 Mbytes of non-volatile RAM
Transmitter Specification	Frequency : approx. 16.6 kHz Output Power : Up to 2 Wats Output Current : 0.125 mA to 16 mA
Receiver Specification	Cable Lengths : 1, 2.5, 5(standard), 10 m Input Impedence : >5 M Ohm Measured Voltage Accuracy : Better than 3 % Input Voltage Range : 0-2 V RMS

In this study the dipole-dipole array was exclusively used to measure electrical resistivity. Not all eight field sites were accessible with the OhmMapper resistivity meter due to a large amount of traffic in an urban environment and anthropogenic barriers such as buildings and houses. Three of the eight field sites were suitable for data collection using the OhmMapper resistivity meter.

4.2.1 FIELD SETUP

For each of the three surveys conducted with the OhmMapper resistivity meter a specific grid orientation had to be considered. For each field site, data collection was initiated on the downthrown side of fault and progressed to the upthrown side of the fault. This was done to keep consistency throughout the surveys. The signal sample and data logging rate was set to two times per second with an operating range of less than one Ohm Meter to greater than 100,000 Ohm Meters. The Data Mapper console was attached to the operator at the waist and the resistivity system was towed behind the operator as the operator walked the survey line. Once the entire traverse has been surveyed to include at least 25 meters past the suspected fault, data collection ceased. For the second line of data collected at each field site, the line was relocated by a distance of 5 meters along the fault line (in the x-direction). The line was then dragged to the downthrown side of the fault and entire line was dragged at least 25 meters past the suspected fault line (Figure 31).

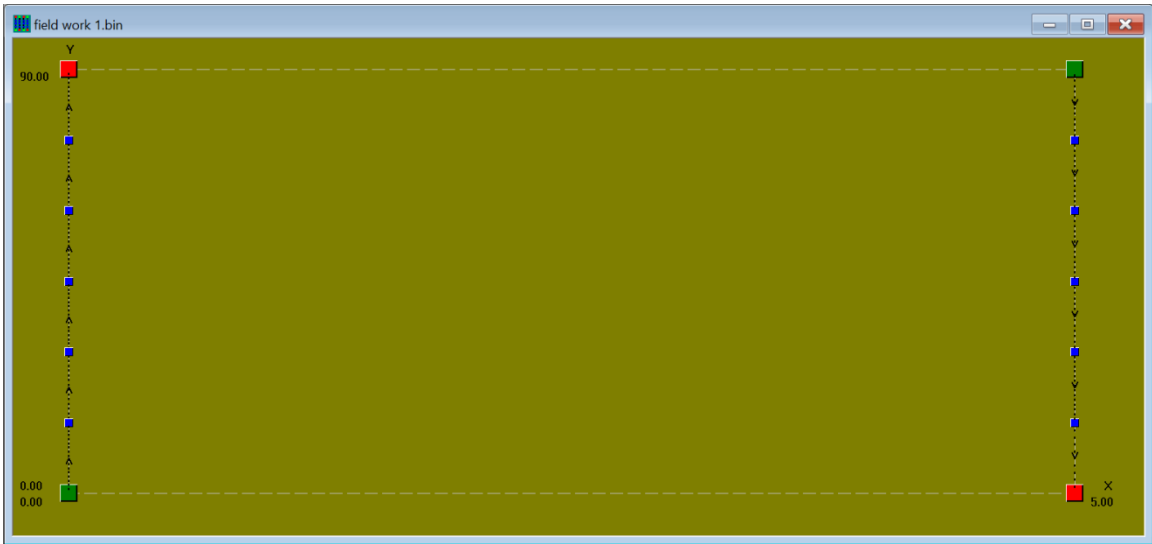


Figure 31. Grid Orientation for OhmMapper Surveys

For every field site that used the OhmMapper, the line was pulled from the downthrown to the upthrown side of the fault and was then moved over 5 meters and surveying continued.

4.2.2 DATA PROCESSING

All data stored on the console was downloaded to a desktop computer via PC communication cables. Individual datasets from the capacitively coupled resistivity surveys were then uploaded to the MagMap 2000 software, which intakes raw resistivity data and outputs representative pseudosections. Once the data files were uploaded to Magmap2000 software, survey orientation and data type were selected (Figure 32). All surveys were conducted in a bidirectional orientation along the Y axis.

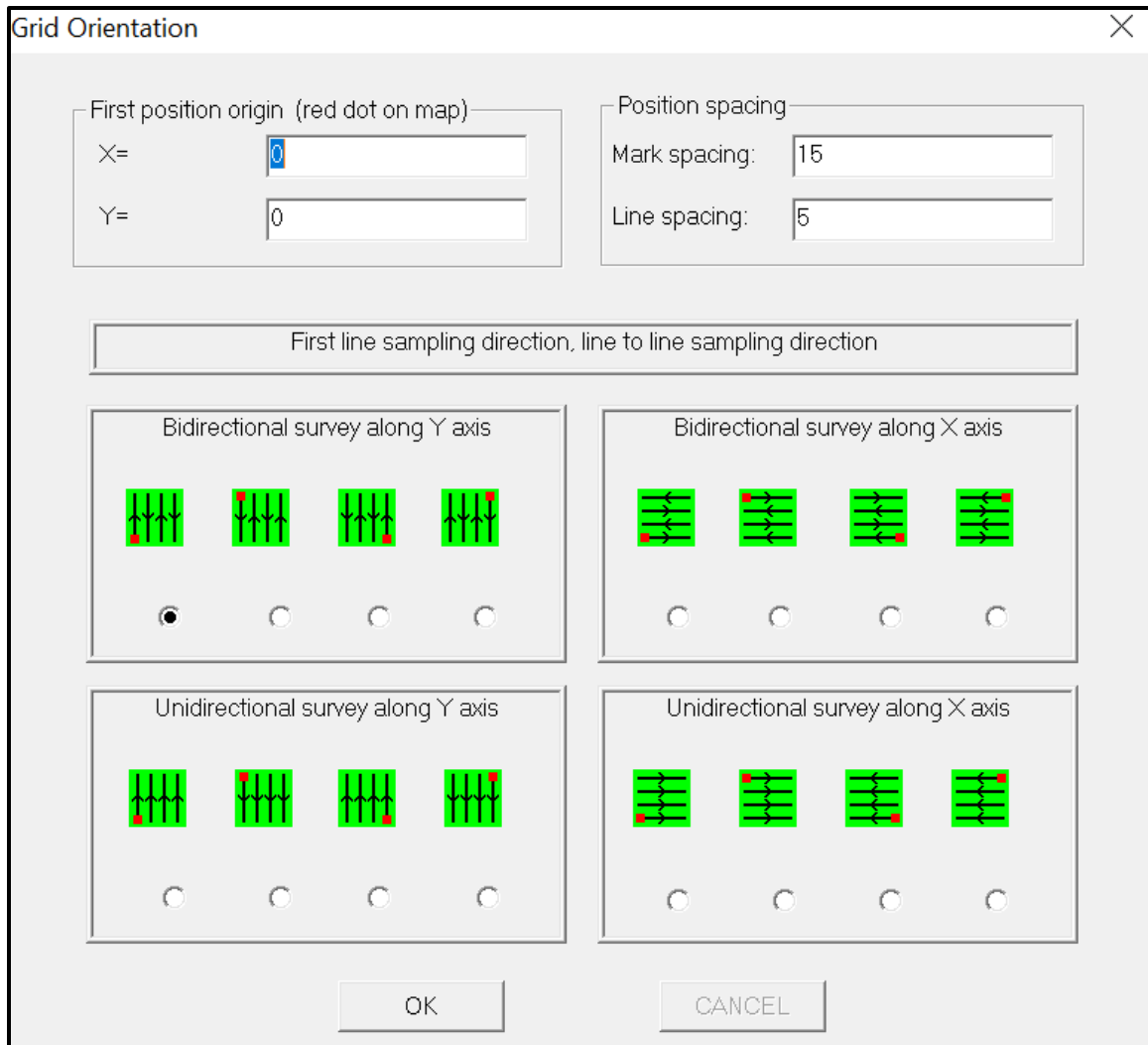


Figure 32. Grid Orientation for OhmMapper Surveys

The grid orientation was chosen for every field site once it was uploaded into the MagMap 2000 software. The first position and position spacing were set based on each field site and the surveys were always bidirectional along the Y-axis.

4.2.3 PSEUDOSECTIONS

After the grid orientation was selected, the survey lines were highlighted and pseudosections were created for each field site (Figure 33). All pseudosections were oriented along the Y-axis, which correlated to the orientation of the appropriate survey lines. The pseudosections were then exported to Earth Imager 2D in the RES2DINV output and formatted to create an inverted resistivity section, which represents the resistivity variation across each field site. Each line of resistivity data was uploaded into the Earth Imager 2D software and was further processed to reduce noise and error.

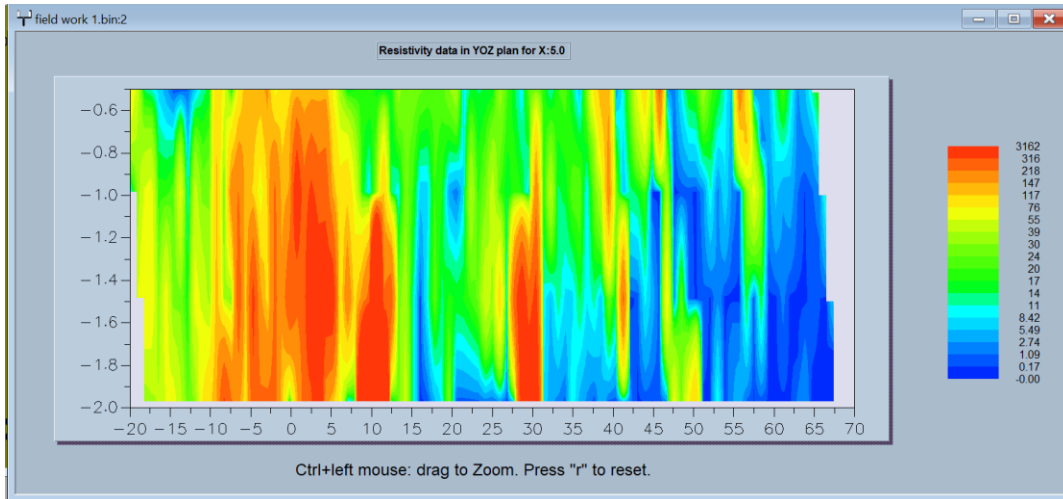


Figure 33. Capacitively Coupled Resistivity Pseudosection from Field Site 2

Raw data is shown as depth (y-axis) vs. the length of the line (x-axis). The darker blue color represented lower resistivity readings, while darker red colors represented higher resistivity readings.

The pseudosection represented a relative distribution model of the apparent resistivity values collected during the field survey. The data had to be inverted in order to produce a true Earth resistivity model. Uploaded data was inverted using the smooth model inversion or Occam's inversion that finds the smoothest model to fit the collected data. *Surface* settings were used for all data collected in the survey (Figure 34).

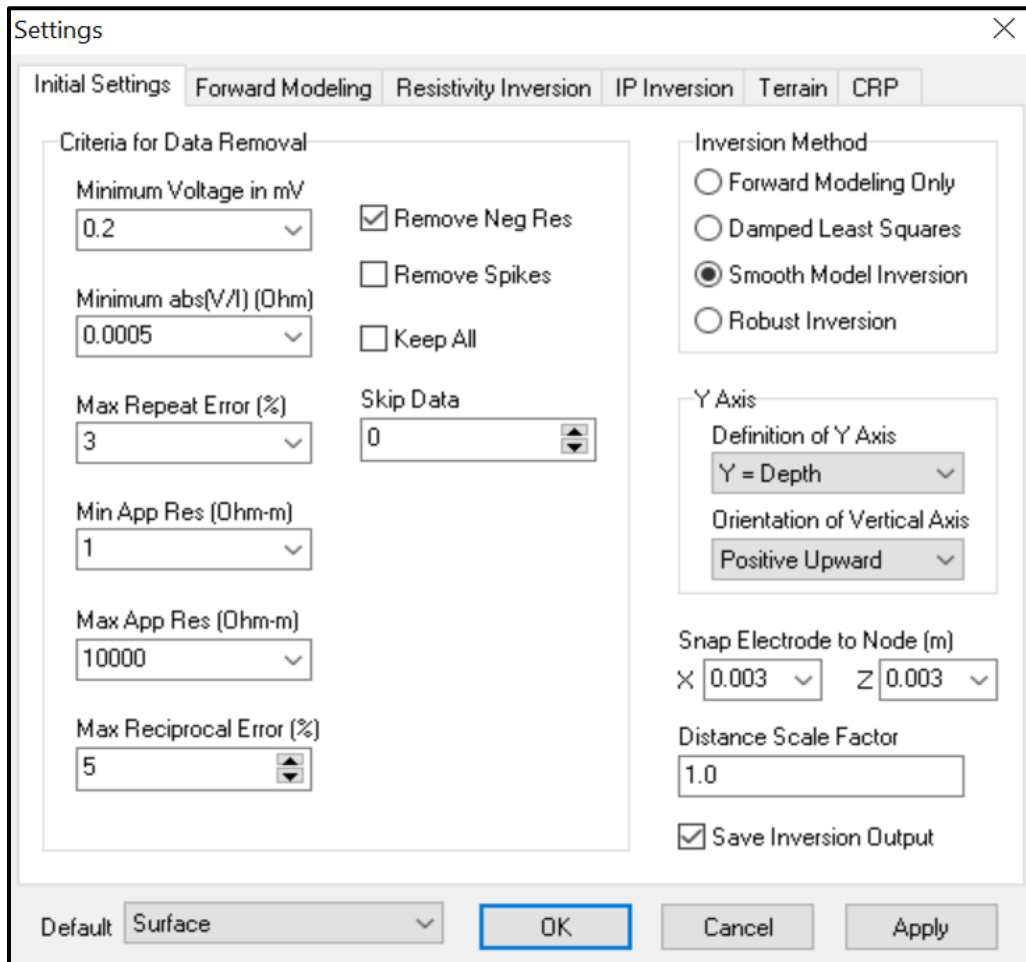


Figure 34. Initial Settings in Earth Imager 2D for OhmMapper Survey

The Smooth Model Inversion was selected as the inversion method for all data collected by the SuperSting resistivity meter. EarthImager 2D utilized this and the Surface setting was always selected as the default.

4.2.4 DATA MISFIT

The percentage of mismatch between data collected in the field and the resulting inversion model was calculated by the inversion software and reported as mismatched or the Root Mean Square (RMS). Noise data collected during the survey could be attributed to surface background resistance or anthropogenic features such as telephone poles, wire fences and pipelines. Noise is automatically accounted for in the initial settings and less weight is given to it in the inverted section. A 3% maximum repeat error was applied in the *Resistivity Inversion* settings (Figure 35). While this setting helps reduce noise, it does not completely remove it.

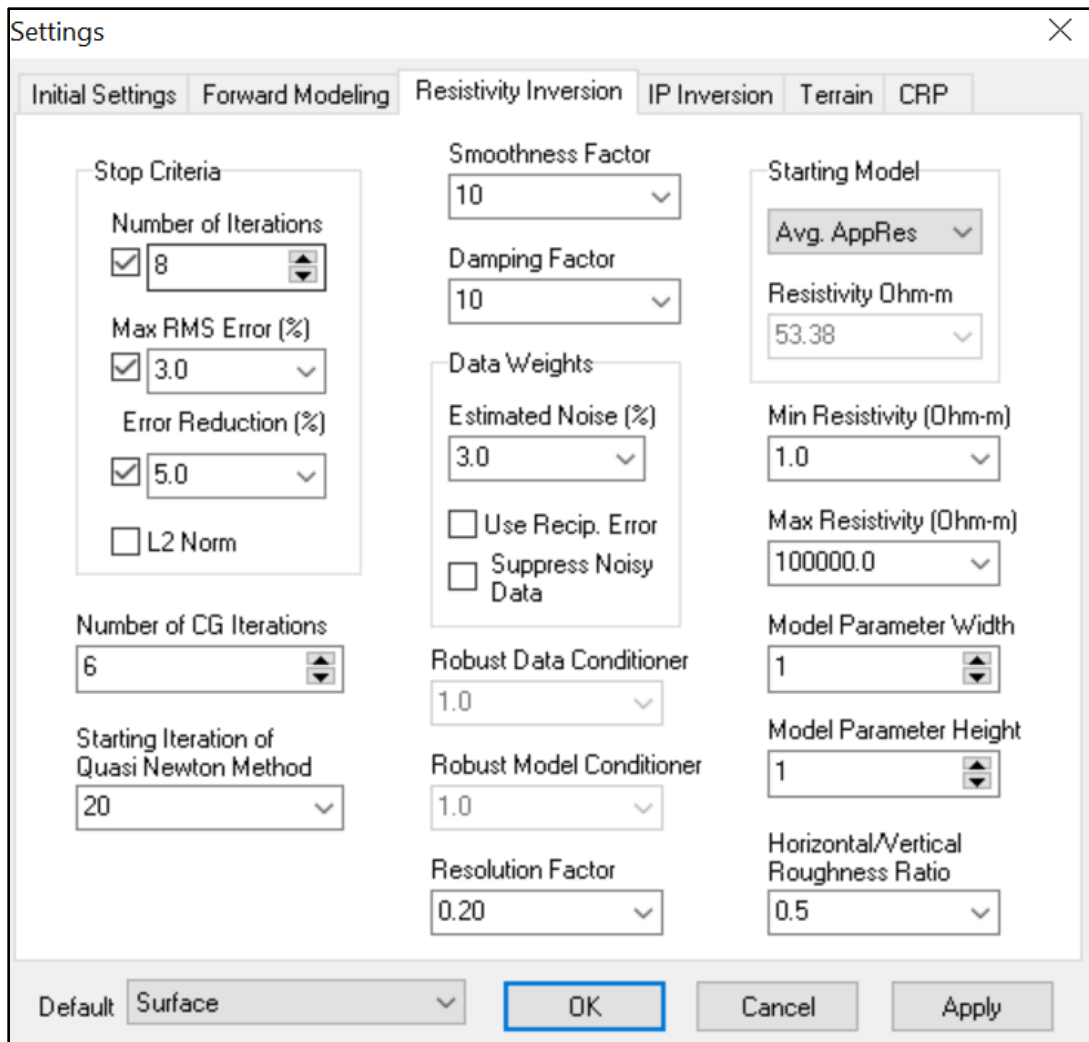


Figure 35. Resistivity Inversion Settings in Earth Imager 2D Software

The estimated noise for all surveys was set to 3% under the Resistivity Inversion settings in the Earth Imager 2D software. All other amounts were set to the default amounts for all surveys.

Data that was poorly fitted was manually removed based on the relative misfit observed in the *data misfit histogram* (Figure 36). A data misfit histogram for each data set allows the operator to remove small amounts of noisy data to

lower the RMS value of the survey. The histogram is automatically generated after every inversion was fully converged.

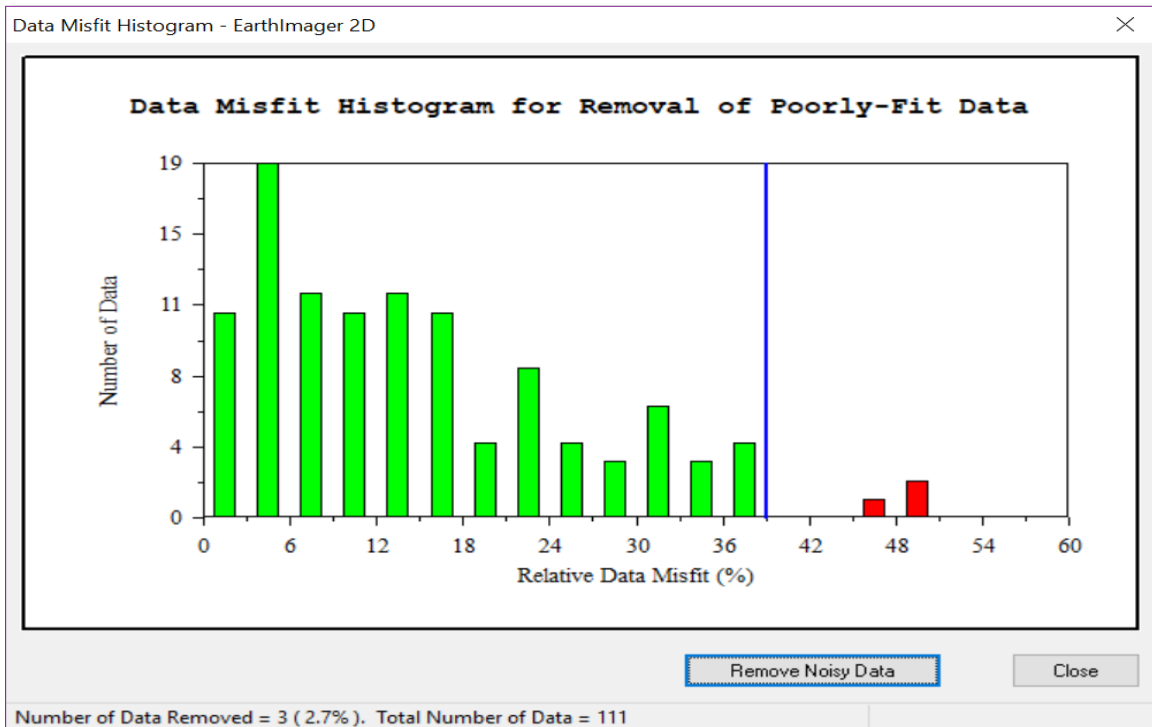


Figure 36. Data Misfit Histogram for Capacitively Coupled Resistivity Field Survey Site 2

A screenshot was taken of the data misfit histogram for the capacitively coupled resistivity survey site 2. The figure shows the relative data misfit % (x-axis) versus the number of data (y-axis). In the above example, 3 out of a total 111 noisy data points were removed.

Any misfit data was removed incrementally before running the inversion processes again. The maximum data removed for all conductively coupled resistivity surveys was 15%. This process was repeated until the Root Mean Squared Error was reduced to <10%. A data misfit crossplot was examined for every field site to see the measured vs. apparent resistivity data (Figure 37).

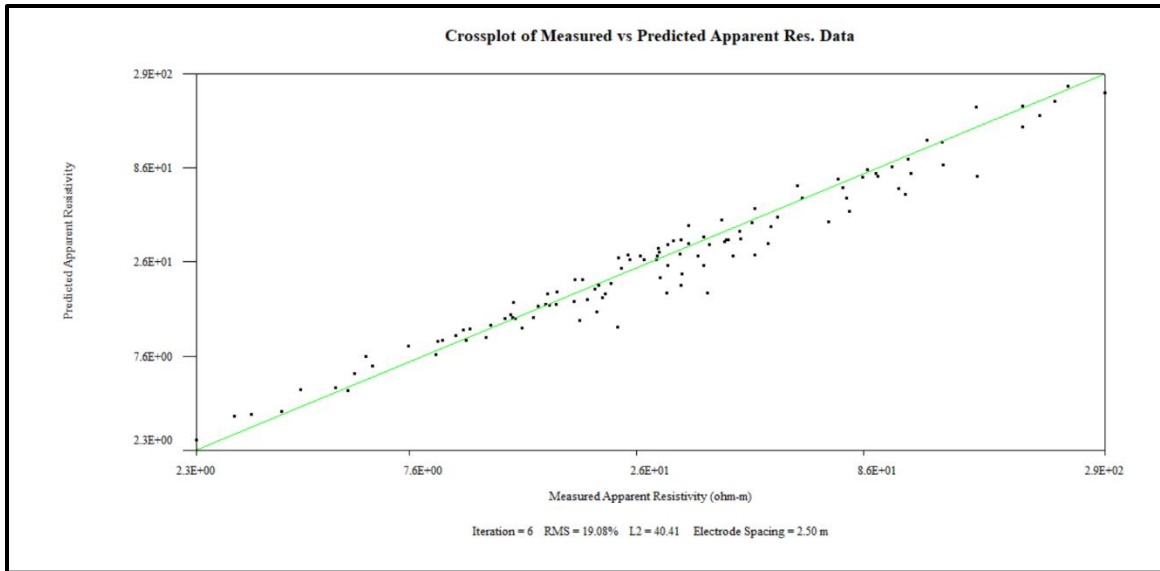


Figure 37. Crossplot of Measured vs. Predicted Apparent resistivity for Capacitively Coupled Resistivity Surveys

This shows the measured apparent resistivity (x-axis) versus the predicted apparent resistivity (y-axis) for field site 2. The green line represents the predicted apparent resistivity while the data points overlain on top of it.

4.3 MULTI-ELECTRODE ELECTRICAL RESISTIVITY METHODOLOGY

The electrical resistivity data was collected using a Super Sting R2 two-channel resistivity meter produced by *Advanced Geosciences, Inc.* that utilized the dipole-dipole array type with 28 electrodes at 4-meter or 6.5-meter spacing. Resistivity data was collected at Field Sites 1, 2, 5 and 7 (Figure 38). Resistivity data could not be collected at other sites (3, 4 and 6) because the survey cables would have intersected busy driveways or intersections. The dipole-dipole array was selected for this survey because the data is plotted in a pseudosection with each measurement having apparent resistivity data plotted at the midpoint between two poles and a depth half the distance between two poles (AGI, 2005). The main advantage of the dipole-dipole array is its high resolution and multi-channel capability. The Super Sting resistivity meter was powered by two twelve-volt batteries and the surveys were conducted in Boost mode for faster surveying time (Figure 39).

The survey length varied depending on the electrode spacing used and were chosen based on the desired depth of investigation and the resolution required to delineate a fault plane (Table 4). Smaller electrode spacing was not considered because it would have given a much shallower depth of investigation of the subsurface. All of the data were processed using EarthImager 2D software by *Advanced Geosciences, Inc.*

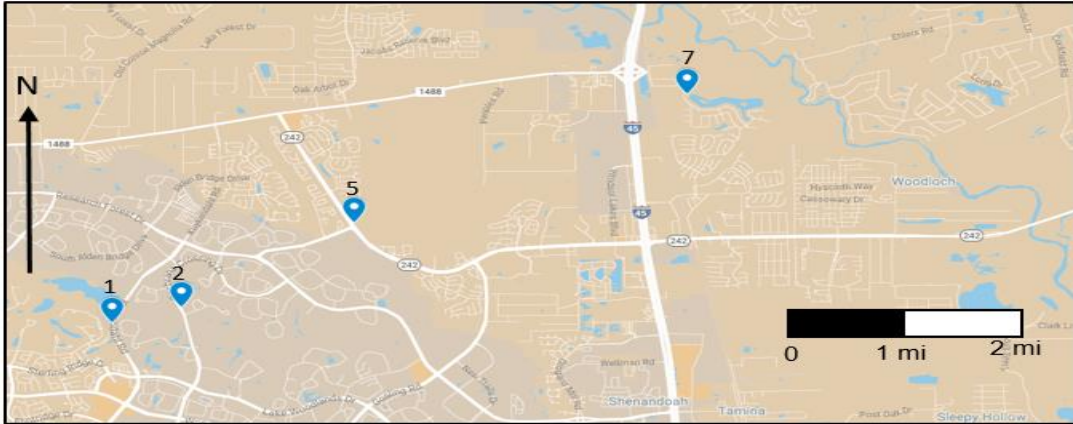


Figure 38. Super Sting Field Sites

Survey sites examined with the R2 SuperSting. Field Sites 1, 2, 5 and 7 were examined in this study. Map created in Google Maps.

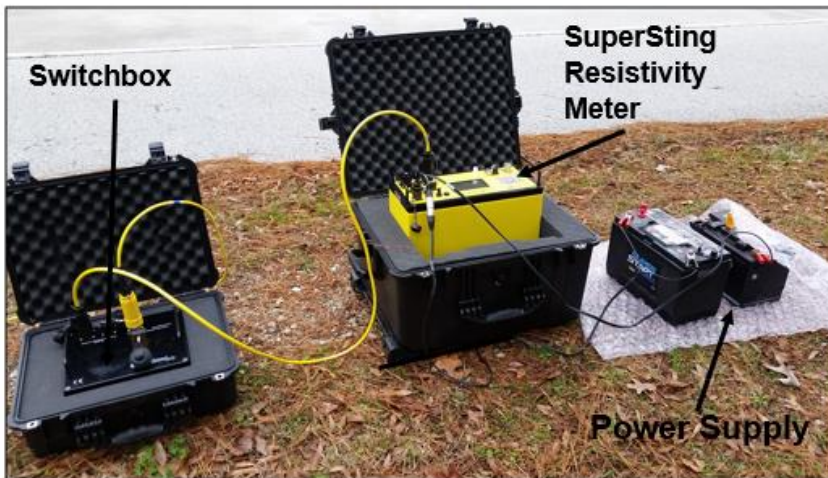


Figure 39. SuperSting R2 Electrical Resistivity Meter Setup

The SuperSting R2 electrical resistivity meter is produced by Advances Geosciences Inc. This image shows the SuperSting console, switchbox and power supply. Electrode cables are attached to the switchbox and are not shown.

Table 4. SuperSting Survey Sites and Field Parameters

Field Site	Electrode Spacing	Survey Length	Array	Maximum Depth of Investigation
1	6.5 meters	176 meters	Dipole-Dipole	32 meters
2	4 meters	108 meters	Dipole-Dipole	26.1 meters
2	6.5 meters	176 meters	Dipole-Dipole	42.5 meters
5	6.5 meters	176 meters	Dipole-Dipole	24.7 meters
7	6.5 meters	176 meters	Dipole-Dipole	42.5 meters

4.3.1 COMMAND FILES

Command files were made prior to conducting the multichannel resistivity surveys and were created in the administrator software on the tablet associated with the SuperSting and produced by *Advanced Geosciences* (Figure 40). The R2 SuperSting unit used in the survey was Wi-Fi enabled and was synchronized with the AGI SuperSting Manager application pre-installed on the tablet. The application included a Command Creator option that allowed command files to be produced. The command file for the 28-electrode dipole-dipole survey was created in the mobile application and was downloaded to the SuperSting resistivity meter via Wi-Fi___33. The command file contained the survey

parameters such as array type, number of electrodes and the spacing between the current and potential electrodes.

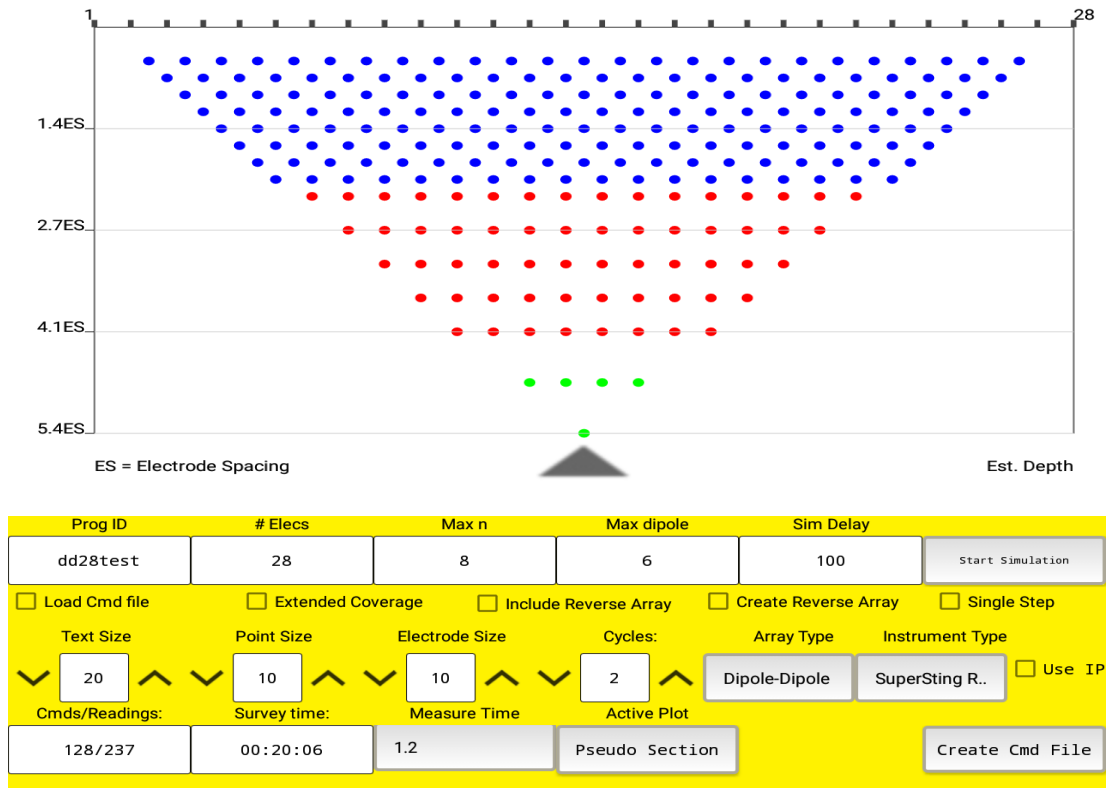


Figure 40. Parameters for a Dipole-Dipole Electrical Resistivity Survey

The parameters for a Dipole-Dipole electrical resistivity survey were customized in the AGI SuperSting Administrator software through the command creator option. The image shows the simulated version of the survey data with the set parameters.

In this study 28 electrodes were used at each survey site with a maximum spacing of 6.50 meters and a minimum spacing of 4 meters between transmitters “C1 and C2” and receiving electrodes “P1” and “P2” (Figure 41). The nomenclature used refers to this spacing as “a”. The maximum “n” is the spacing

ratio between “C1 and P1” electrodes to the “C2 and C1” or “P1 and P2” dipole separation. For this survey the “**n**” spacing was set to 8. For dipole-dipole arrays, the “**a**” spacing is initially kept fixed and gradually increased along with the “**n**” factor to allow for greater depth penetration (Loke, 1999; Majzoub, 2016). The spacing between the dipole-dipole pairs was dependent on the electrode spacing used in the field. The parameters set in the command file automatically dictate the geometry of the survey (Figure 41). Since the software dictates the geometry of the survey automatically it is not necessary to move the electrodes during the survey.

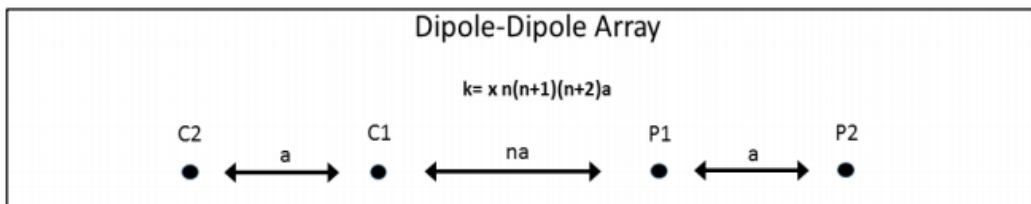


Figure 41. Dipole-Dipole Electrode Configuration

The Dipole-Dipole array is shown as a simplified model of the electrode configuration for the survey. “**n**” is the distance ratio between the dipole separation and “**a**” is the spacing between the transmitting and receiving electrodes (Majzoub, 2016).

4.3.2 DATA ACQUISITION

Survey sites and lengths were limited by their access to long stretches of roadways without intersecting driveways. A tape measure was used to measure the correct spacing in between the electrodes. The surficial deformation was first identified at each field site and then a flag was placed along the tape measure at the predetermined interval to mark the proper electrode spacing for each survey. Stainless steel stakes were hammered at the predetermined interval depending on the length of the survey. The goal of each survey was to have the fault plane as close as possible to the center of the survey line to attain maximum efficiency. The two sets of cable were connected together and then the electrodes were attached to the stainless-steel stakes. All data was collected using 28 electrodes and a dipole-dipole array.

4.3.3 FIELD SETUP

For this study, two cable sections with 14 electrodes per cable and 28 electrodes total were used. Cable sections with electrodes 1-14 represented the low-address section and 15-28 represented the high address section. The SuperSting resistivity meter was placed at the high address for all surveys, as per the recommendation of the manufacturer (Figure 42) (AGI, 2015). Two 12-volt batteries were used in this survey and allowed the SuperSting to operate in

Boost mode, which has a range of 0-200 Watt instead of the main mode that is powered by one 12-volt battery and has a range of 0-100 Watt (Figure 43).

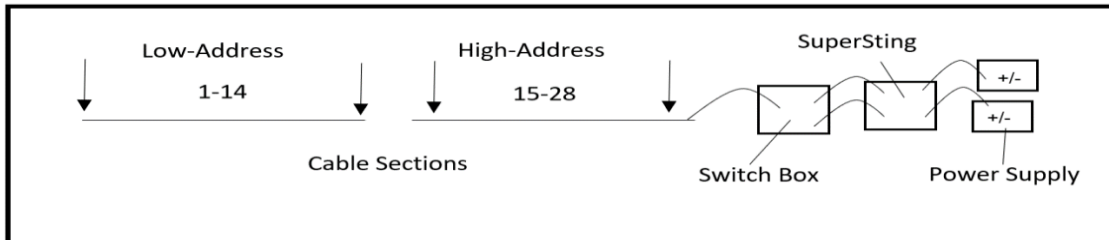


Figure 42. Schematic of Field Surveying with SuperSting

The SuperSting was placed at the end of the high-address of the cable sections and was attached to a switchbox and two 12-volt batteries that were the power supply. The switchbox was used at the end of the survey since there were no further cables sections to attach together.

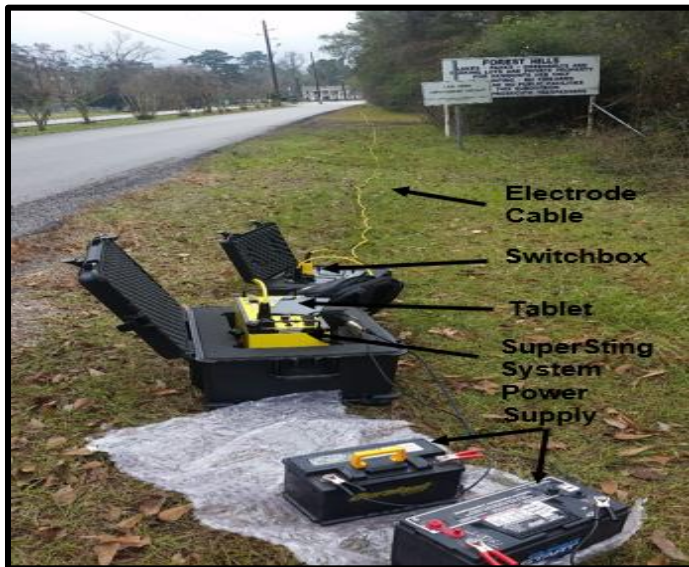


Figure 43. Field Setup of 28-Electrode SuperSting Survey

A 28-electrode survey was completed using electrode cables, a switchbox, a tablet that connected to the SuperSting system and the power supply. The low-address electrode cables were attached to the high-end address electrode cables which was then connected to the switchbox. The SuperSting system was connected to a switchbox and two 12-volt batteries. The SuperSting was Wi-Fi enabled so a tablet was used to remotely control the SuperSting and monitor the survey.

For this survey, inversion settings were set to 1.2 second measurement time with two measurement cycles at each electrode pair. The maximum error percentage between measurements was set to 2% and injected current maximum to 2000 Ma. A contact resistance test was performed at each field site in order to ensure quality control of the survey. A contact resistance test is an option when an automatic survey is selected and is a feature on the SuperSting that allows the user to check the quality of the electrode coupling with the ground. If the contact resistance was greater than 1500 ohms than the electrode cable was repositioned, or the metal stake was hammered farther into the ground. As the data was collected it was monitored on the tablet that was synced to the SuperSting (Figure 44).

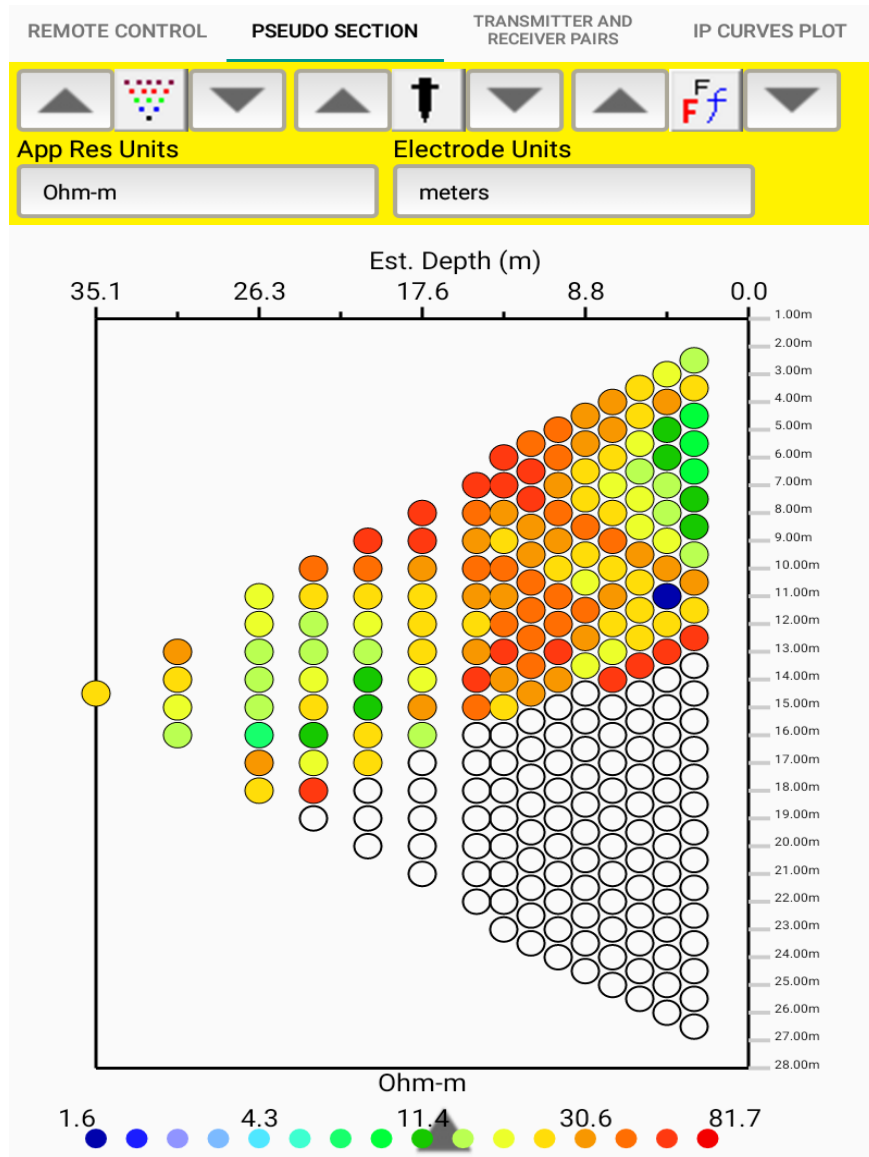


Figure 44. Pseudosection Monitored During SuperSting Field Survey

This is a screenshot of the tablet while it was synced to the SuperSting in the middle of a field survey. The estimated depth is shown versus the electrodes. Raw resistivity is shown in Ohm-m.

4.3.4 DATA PROCESSING AND PSEUDOSECTIONS

For the multi-electrode electrical resistivity surveys the electrical resistivity data was processed using AGI's Earth Imager 2D version 2.4.4. All data collected from the field site was uploaded to a personal computer from the tablet synchronized with the SuperSting resistivity meter or through a PC Com cable produced by AGI that was attached to a Brainbox adapter for a computer. Raw data uploaded into the Earth Imager 2D software was displayed as a pseudosection. The pseudosection represented a relative distribution model of the apparent resistivity values collected during the field survey. The data had to be inverted in order to produce a true Earth resistivity model and noise was removed incrementally before running the inversion processes again. All data was inverted using the smooth model inversion or Occam's inversion that finds the smoothest model to fit the collected data. *Surface* settings were used for all data collected in the survey. The maximum data removed for all multi-electrode electrical resistivity surveys was 15%. This process was repeated until the Root Mean Squared Error was reduced to <10%. A data misfit crossplot was examined for every field site to see the measured vs. apparent resistivity data. EarthImager2D was also used for the multi-electrode resistivity data so the software methodology is the same as what was previously mentioned in the capacitively coupled resistivity data processing section (Figure 32-35).

CHAPTER 5

5.0 RESULTS

For this study three geophysical techniques were used to delineate the Big Barn fault in Montgomery County, Texas. The first geophysical technique used was gravity surveying and the CG-5 Autograv was used to conduct the surveys. Gravity measurements were taken at 25m intervals six different traverses oriented roughly perpendicular to the apparent fault line. The second geophysical technique used in this study was a conductively coupled resistivity (CCR) survey using the OhmMapper resistivity meter. The CCR survey was conducted at three of the seven predetermined field sites along traverses perpendicular to the apparent fault line. The third and final geophysical technique used was multi-electrode electrical resistivity survey, utilizing the SuperSting R2 Wi-Fi RES/IP/SP resistivity meter. The SuperSting resistivity meter was used at four field sites and along traverses established in the CCR and gravity section of the study. The location of the seven field sites are shown in figure 45.

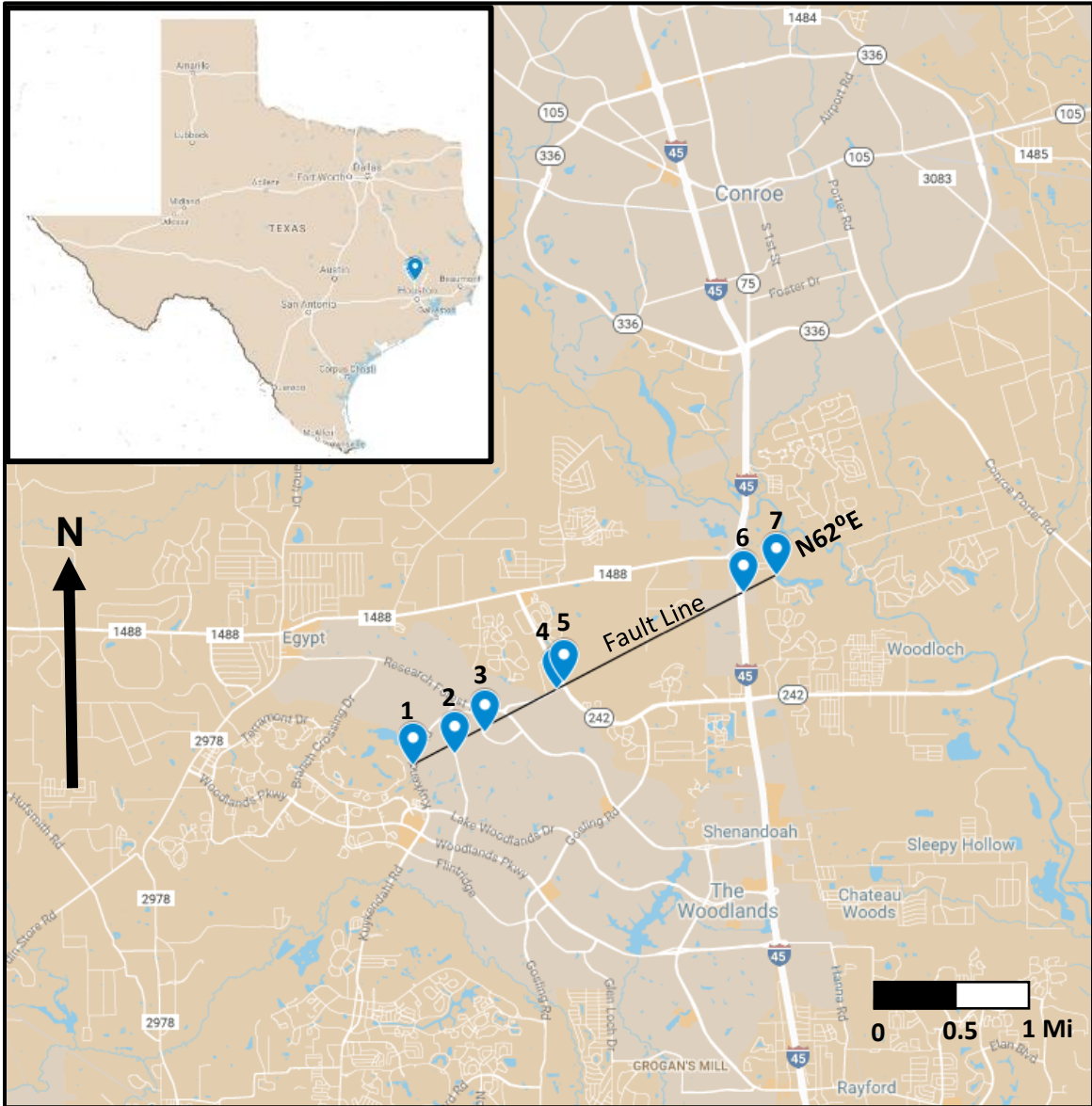


Figure 45. Study Area Regional Location

The study area is shown relative to the city of the Conroe and the Woodlands, Texas. Field stations are shown with blue icons and the approximate strike of the fault line was determined to be approximately $N62^{\circ}E$.

Various geophysical surveying techniques were performed at each field site. The number and type of techniques applied were dependent on the accessibility and safety issues associated with individual field sites. The field site, applied techniques and fault trends are shown in Table 5 below.

Table 5. Techniques Used and Fault Trends at Each Field Site

Table 5 shows the geophysical techniques applied at each field site along with the fault trends associated with the field site. An X is indicative of the geophysical technique being utilized at that particular field site, while and 0 is indicative of the geophysical technique not being utilized at that particular field site. Only field site 2 had all three geophysical techniques performed.

Field Sites	Technique Used			
#	Gravimetry	Multi Electrode Resistivity	Capacitively Coupled Resistivity	Measured Fault Trends
1	X	X	0	N61°E
2	X	X	X	N58°E
3	X	0	X	N66°E
4	X	0	0	N54°E
5	X	X	0	N65°E
6	X	0	0	N62°E
7	0	X	X	N63°E

5.1 GRAVIMETRY

Gravimetry was used in this study to delineate differences in rock densities within the study area. A previous study (Khan et. al., 2013) of the geology of the area showed that the Lissie Sand was suspected to be on the downthrown (southern) end of the fault line while the Willis Clay was suspected to be on the upthrown (northern) end of the fault line. Field sites 1-6 were examined using the CG-5 Autograv and the results of the gravity survey is shown below for each field site (Figures 46-51).

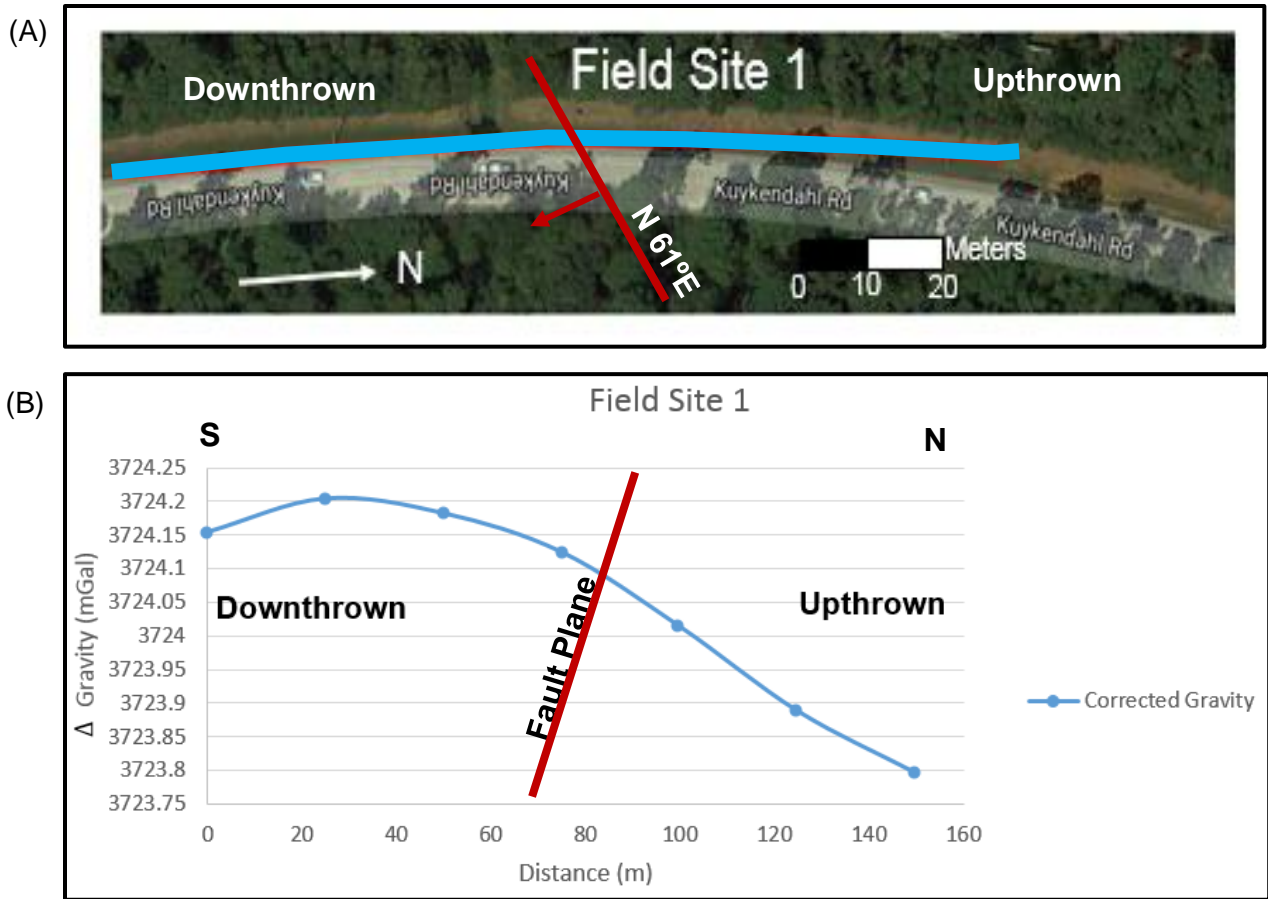


Figure 46. Gravity Data from Field Site 1

(A) Study area for field site 1 along with the N 61°E trend of the fault line measured at this field site with a Brunton compass. This location is along Kuykendahl Road in Montgomery County, Texas. Note that North is to the right in this image (Photo from Google Earth). (B) Plotted corrected gravity data from field site 1. Using gravimetry, it was determined that the (southern) downthrown side of the fault had higher gravity readings than the (northern) upthrown side of the fault. The data for this survey is anomalous to typical gravity surveys that have higher gravity readings on the upthrown side of the fault. This anomalous result could be due to a higher accumulation of the denser Lissie Sand on downthrown side of the fault and the less dense Willis Clay on the upthrown side of the fault. The Lissie Sand could also be pinching out at the fault line, leaving only the Willis Clay on the upthrown side of the fault. Khan et. al., 2013, also had anomalous gravity data that he attributed to the density differences between the Lissie Sand and Willis Clay near the Hockley Fault.



Figure 47. Gravity Data from Field Site 2

(A) Study area for field site 2 along with the N 58°E trend of the fault line measured at this field site with a Brunton compass. This site was located along Cochrans Crossing Dr. in Montgomery County, Texas (Photo from Google Maps). (B) Plotted corrected gravity data from field site 2. Using gravimetry, it was determined that the (southern) dowthrown side of the fault had higher gravity readings than the (northern) upthrown side of the fault. The data for this survey is anomalous to traditional gravity surveys that have higher gravity readings on the upthrown side of the fault. This anomalous behavior could be due to a higher accumulation of the denser Lissie Sand on dowthrown side of the fault and the less dense Willis Clay on the upthrown side of the fault. Gravity readings taken 30-40 meters along the survey line could represent the Lissie Sand interfacing with the Willis Clay along the fault line or it may be pinching out along the fault line. Khan et. al., 2013, also had anomalous gravity data that he attributed to the density differences between the Lissie Sand and Willis Clay near the Hockley Fault.

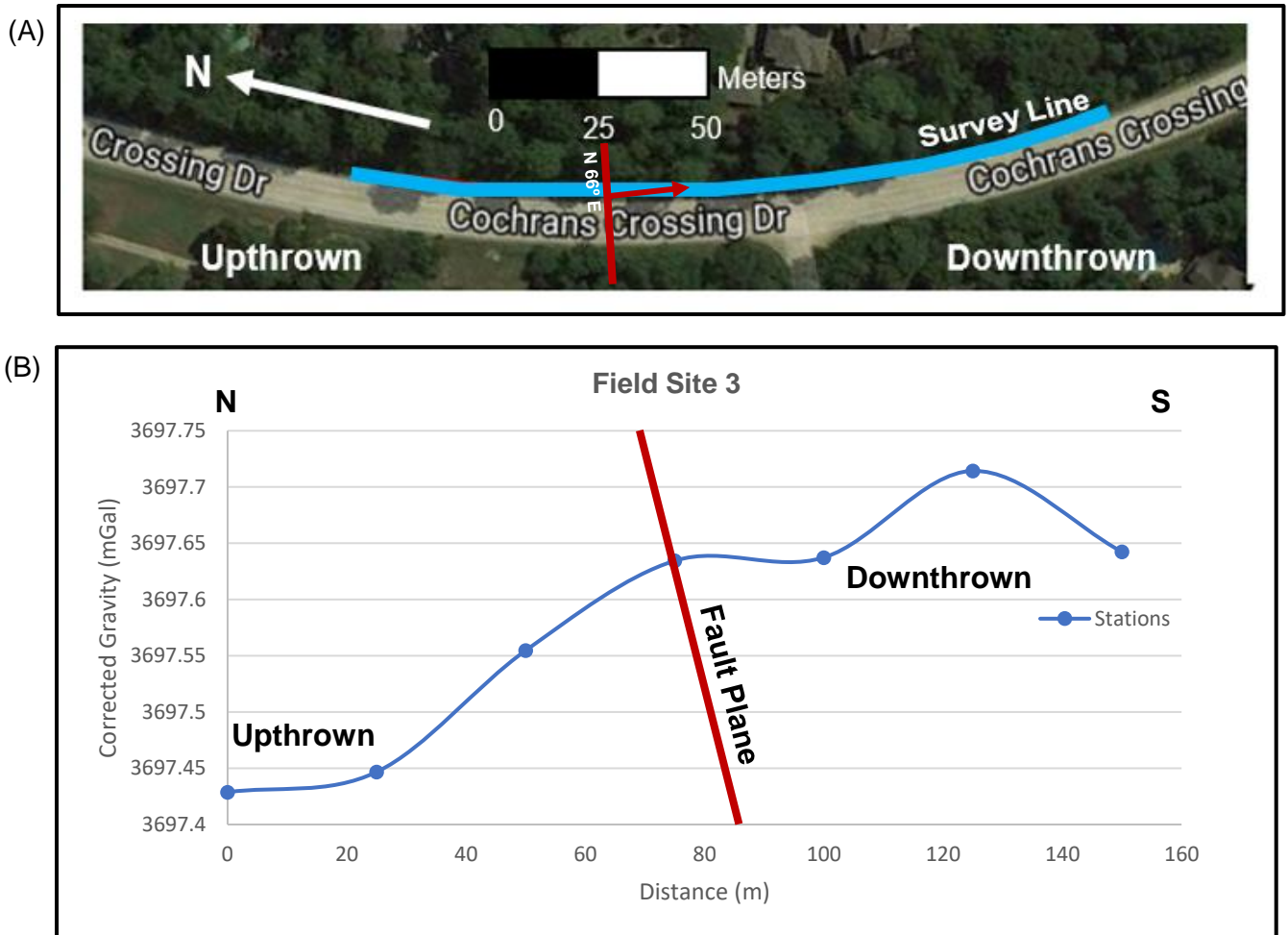


Figure 48. Gravity Data from Field Site 3

(A) Study area for field site 3 along with the N 66°E trend of the fault line measured at this field site with a Brunton compass. This site was located along the other side of Cochrans Crossing Dr. in Montgomery County, Texas (Photo from Google Maps). (B) Plotted corrected gravity data from field site 3. Using gravimetry, it was determined that the (southern) downthrown side of the fault had higher gravity readings than the (northern) upthrown side of the fault. The data for this survey is anomalous to traditional gravity surveys that have higher gravity readings on the upthrown side of the fault. This anomalous behavior could be due to a higher accumulation of the denser Lissie Sand on downthrown side of the fault and the less dense Willis Clay on the upthrown side of the fault. Khan et. al., 2013, also had anomalous gravity data that he attributed to the density differences between the Lissie Sand and Willis Clay near the Hockley Fault.

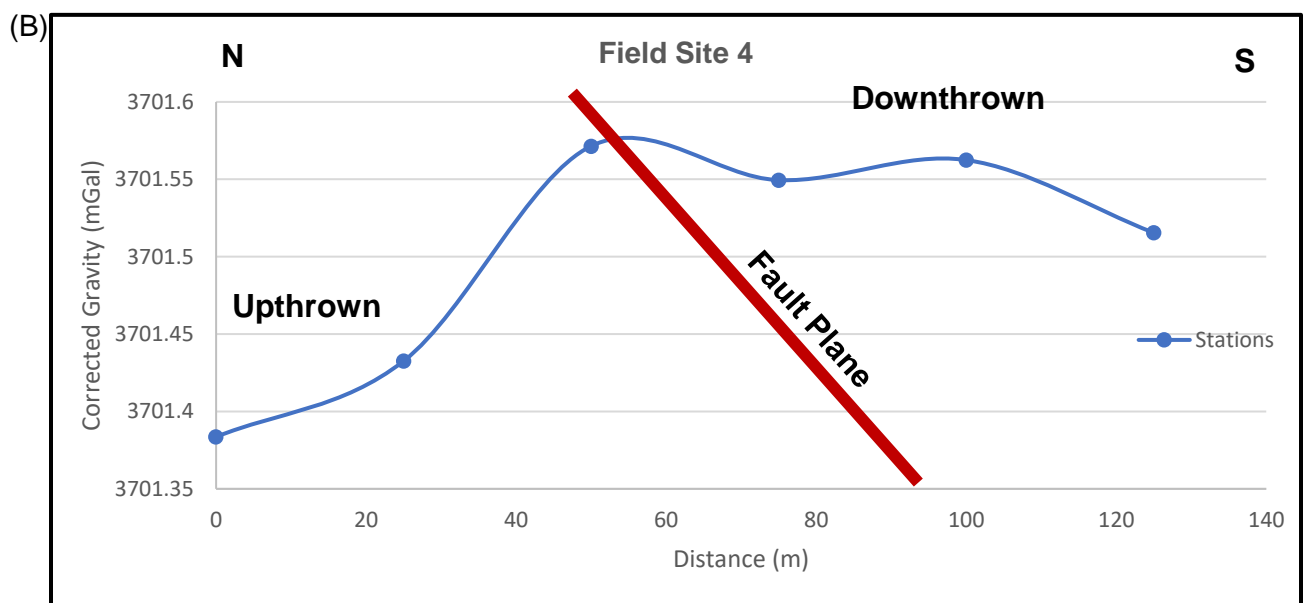
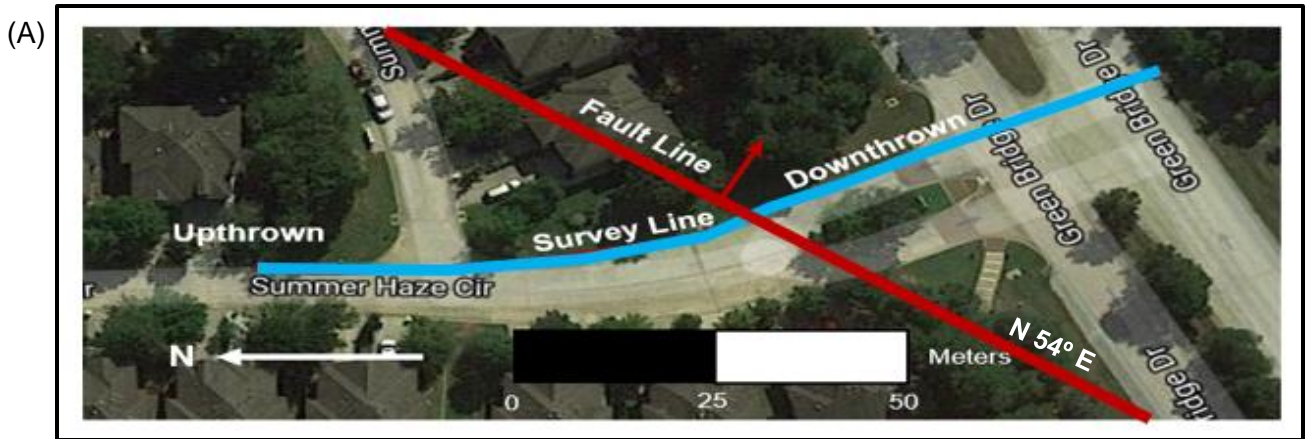


Figure 49. Gravity Data from Field Site 4

(A) Study area for field site 2 along with the N 54°E trend of the fault line measured at this field site with a Brunton compass. This site was located at Summer Haze Circle and Green Bridge Dr. in Montgomery County, Texas (Photo from Google Maps). (B) Plotted corrected gravity data from field site 2. Using gravimetry, it was determined that the (southern) downtown side of the fault had higher gravity readings than the (northern) upthrown side of the fault. The data for this survey is anomalous to traditional gravity surveys that have higher gravity readings on the upthrown side of the fault. This anomalous behavior could be due to a higher accumulation of the denser Lissie Sand on downtown side of the fault and the less dense Willis Clay on the upthrown side of the fault. Khan et. al., 2013, also had anomalous gravity data that he attributed to the density differences between the Lissie Sand and Willis Clay near the Hockley Fault.

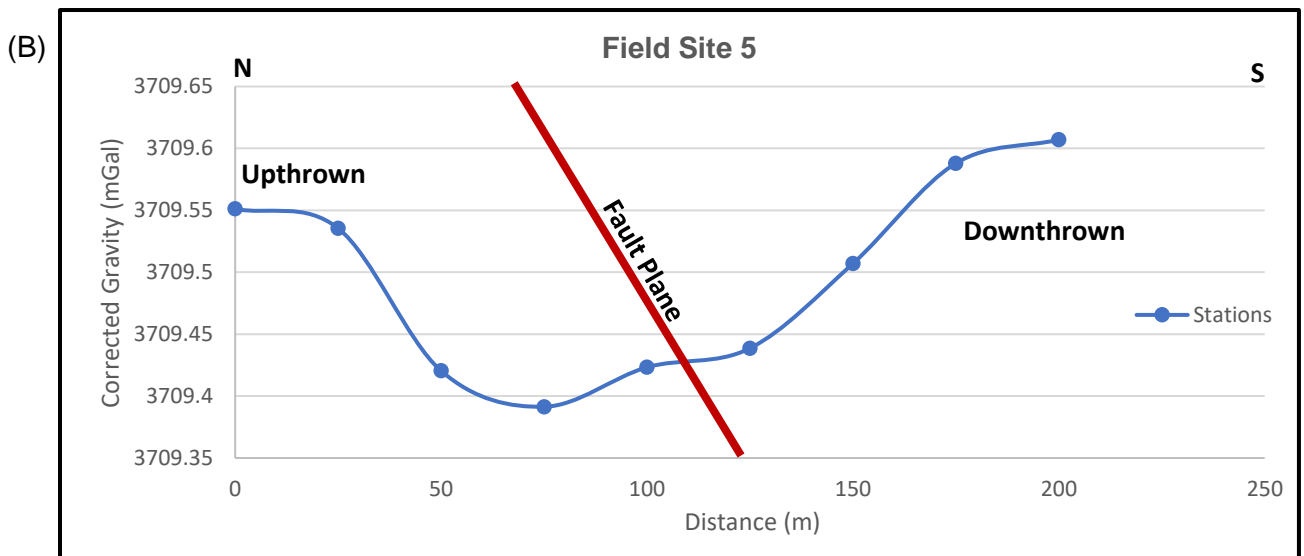
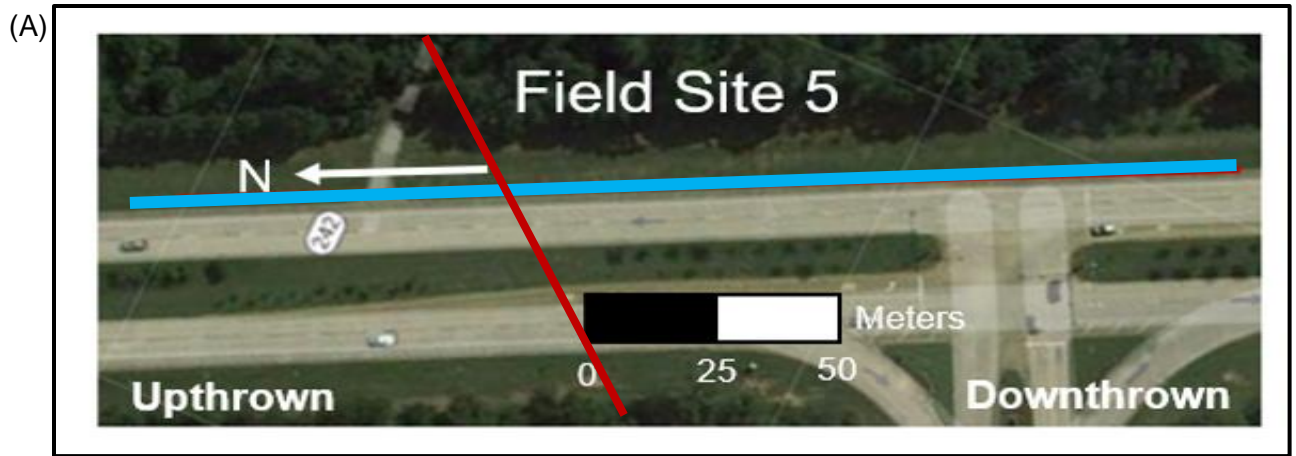


Figure 50. Gravity Data from Field Site 5

(A) Study area for field site 2 along with the N 54°E trend of the fault line measured at this field site with a Brunton compass. This site was located along TX-242 in Montgomery County, Texas (Photo from Google Maps). (B) Plotted corrected gravity data from field site 2. Using gravimetry, it was determined that the (southern) downthrown side of the fault had higher gravity readings than the (northern) upthrown side of the fault. The data for this survey is anomalous to traditional gravity surveys that have higher gravity readings on the upthrown side of the fault. For this field site, the variance in the gravity from the upthrown to downthrown side is minimal and could be caused by the Lissie Sand being overlain on top of the Willis Clay throughout the field site with offset of the layers near the vicinity of the fault. If faulting caused the layers to offset, then a slightly higher accumulation of the Lissie Sand will be seen on the downthrown side and a higher accumulation of the Willis Clay on the upthrown side of the fault. Khan et. al., 2013, also had anomalous gravity data that he attributed to the density differences between the Lissie Sand and Willis Clay near the Hockley Fault.

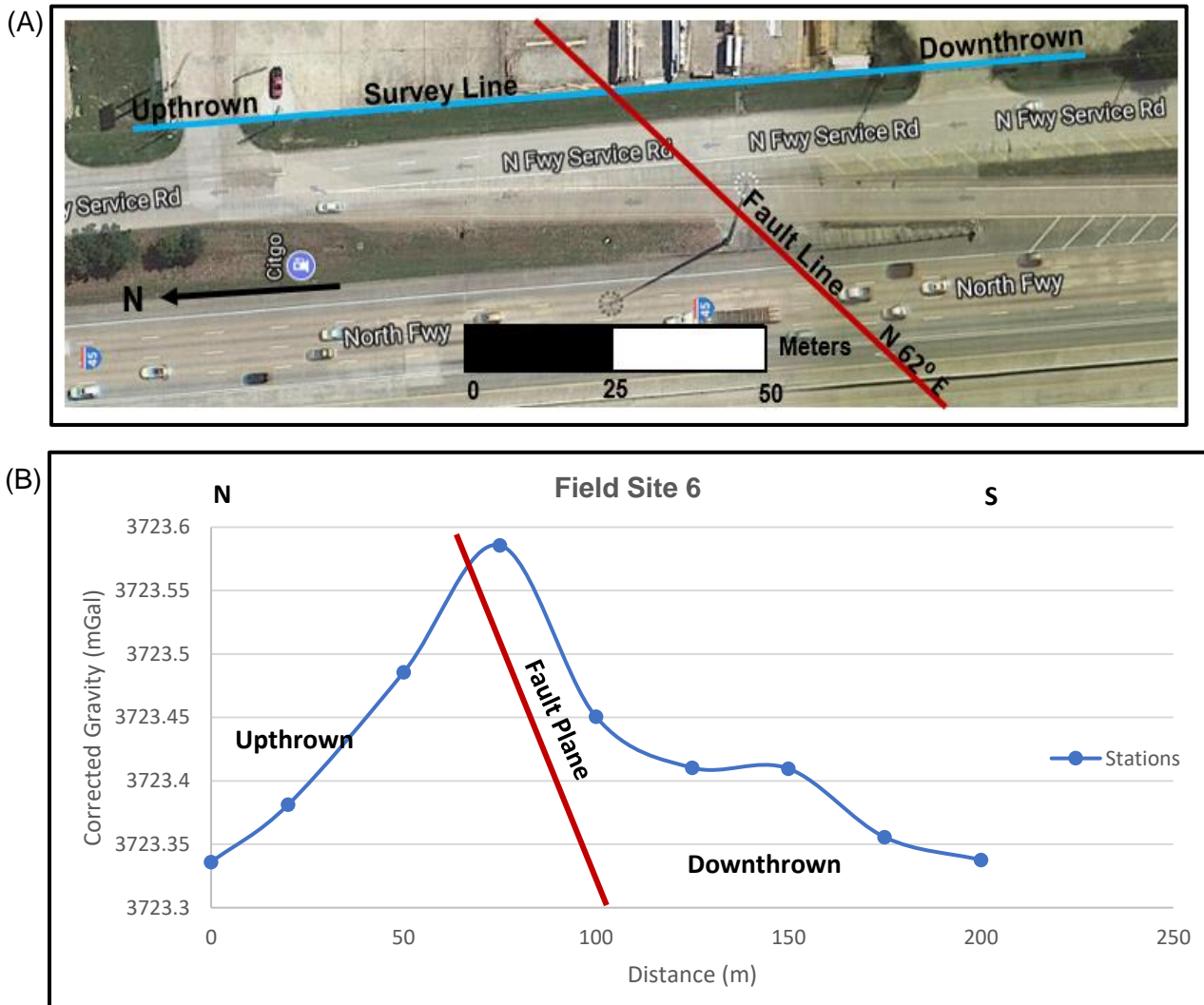


Figure 51. Gravity Data from Field

(A) Study area for field site 2 along with the N 62°E trend of the fault line measured at this field site with a Brunton compass. This site was located along the frontage road of Interstate Highway 45 in Montgomery County, Texas (Photo from Google Maps). (B) Plotted corrected gravity data from field site 2. Using gravimetry, it was determined that the (southern) dnthrown side of the fault had higher gravity readings than the (northern) upthrown side of the fault. The data for this survey is anomalous to traditional gravity surveys that have higher gravity readings on the upthrown side of the fault. For this field site, the variance in the gravity from the upthrown to dnthrown side is minimal and could be caused by the Lissie Sand being overlain on top of the Willis Clay throughout the field site with offset of the layers near the vicinity of the fault. If faulting caused the layers to offset, then a slightly higher accumulation of the Lissie Sand will be seen on the dnthrown side and a higher accumulation of the Willis Clay on the upthrown side of the fault. Khan et. al., 2013, also had anomalous gravity data that he attributed to the density differences between the Lissie Sand and Willis Clay near the Hockley Fault.

5.2 CAPACITIVELY COUPLED RESISTIVITY

The second geophysical technique used in this study utilized capacitively coupled resistivity and was completed using the OhmMapper TR4 resistivity system. The OhmMapper resistivity meter measured electrical resistivity at shallow depths and was used to delineate the varying rock types on either side of the fault. The downthrown side of the fault contained the Lissie Sand which showed a higher resistivity and was shown as a warmer color (orange-red). The upthrown side of the fault was characterized by the Willis Clay which showed a lower resistivity and was shown as a cooler color (blue-purple). The OhmMapper resistivity meter was used at three field sites but had multiple lines completed at each field site. The OhmMapper resistivity meter was used at field sites 2, 3 and 7. The data collected for the OhmMapper resistivity meter is shown below for each field site (Figures 52-54). The OhmMapper resistivity meter was not used at field sites 1, 4, 5 & 6 due to busy roadways and driveway intersections along the prospective survey lines.

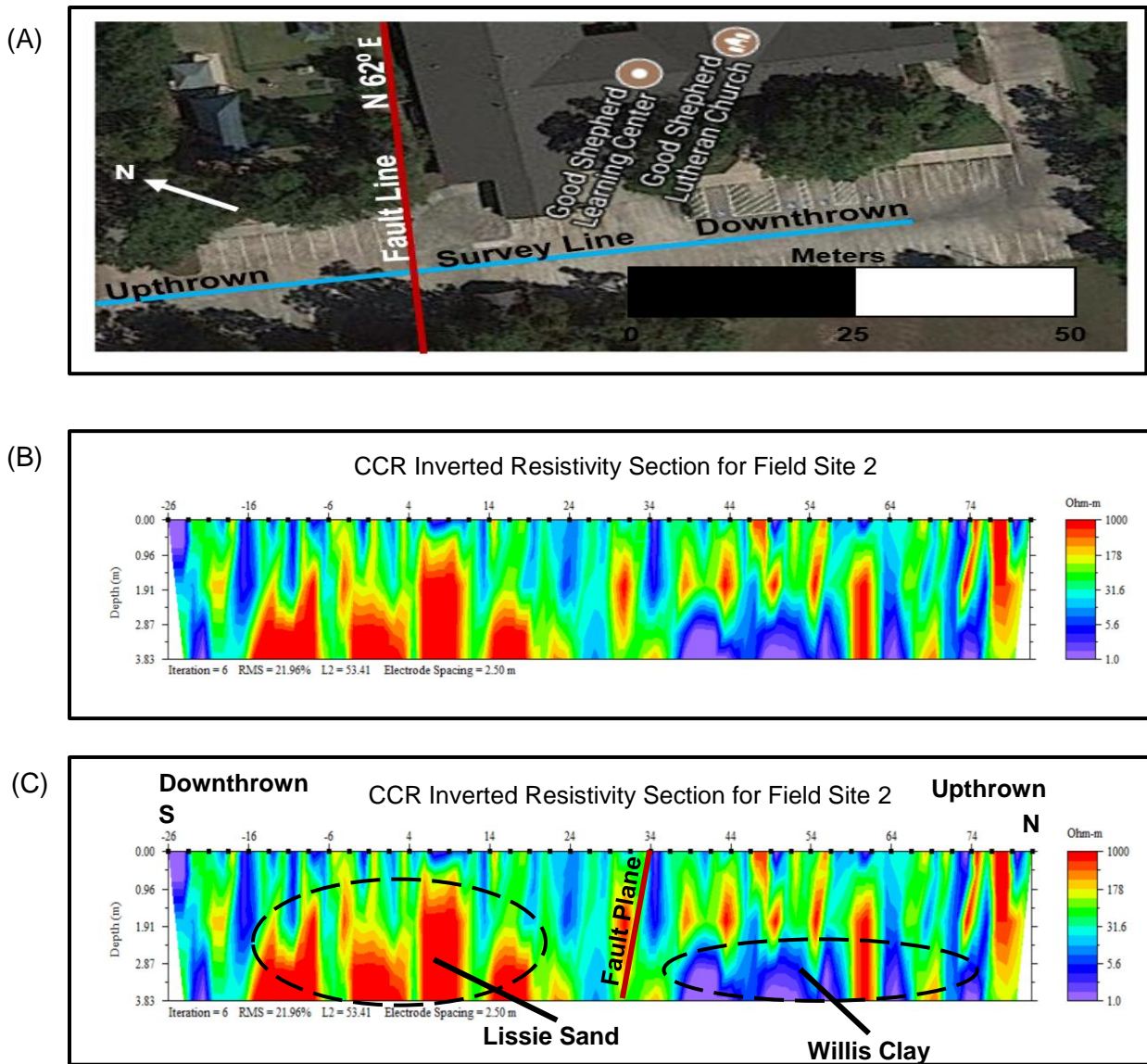


Figure 52. CCR Survey Site 2 Data

(A.) CCR survey site 2 with the fault line and survey line outlined (B.) Capacitively coupled inverted resistivity section for field site 2. (C.) Interpretation of inverted resistivity section from CCR survey site 2. The Lissie Sand was found on the downthrown side of the fault and showed a higher resistivity while the Willis Clay was found on the upthrown side of the fault and showed a lower resistivity. The fault plane was determined to be located at the proximity of the intersection of the Lissie Sand and the Willis Clay. The total depth of investigation was 3.83 meters.

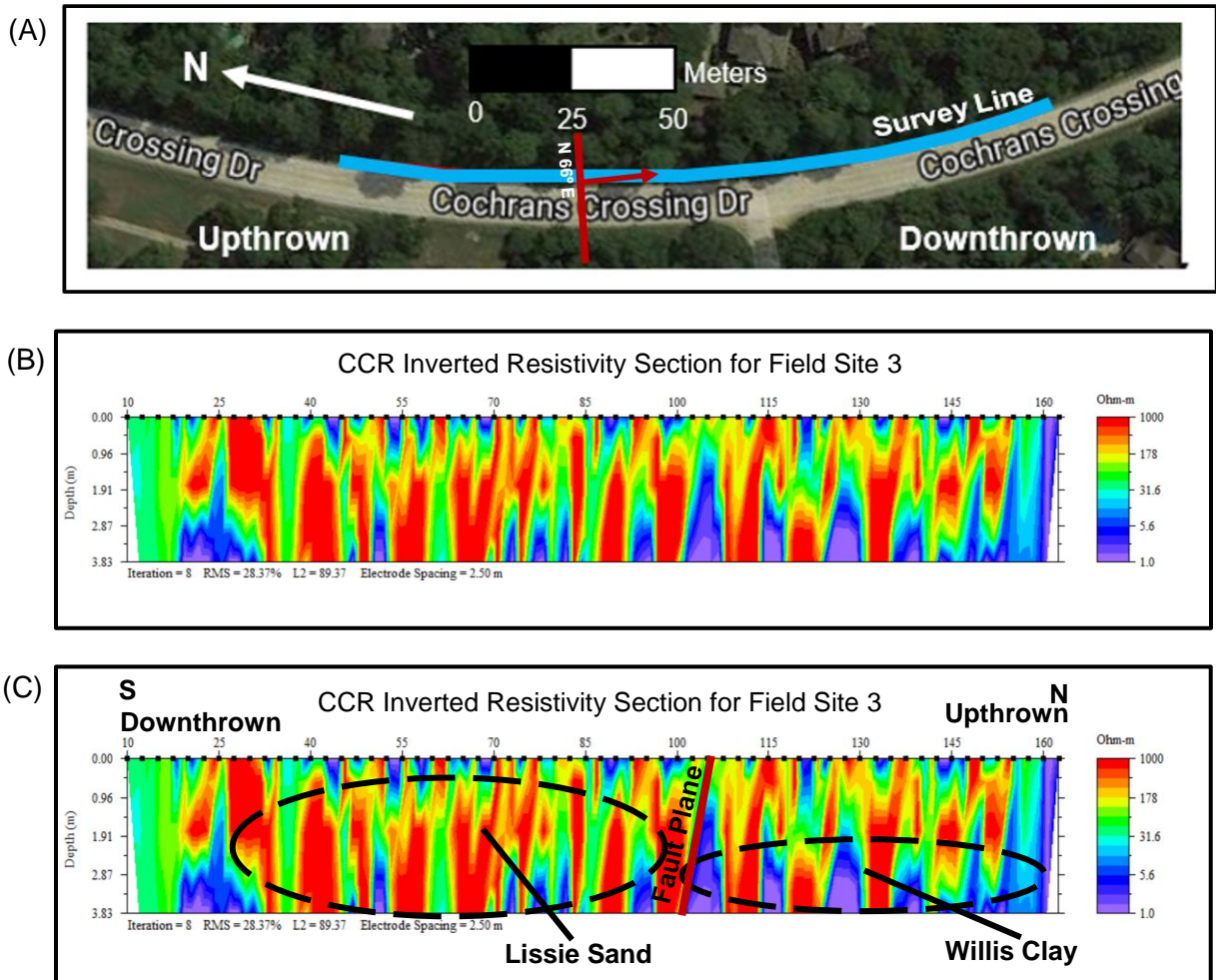


Figure 53. CCR Survey Site 3 Data

(A.) CCR survey site 3 with the fault line and survey line outlined (B.) Capacitively coupled inverted resistivity section for field site 3. (C.) Interpretation of inverted resistivity section from CCR survey site 3. The Lissie Sand was found on the downthrown side of the fault and showed a higher resistivity while the Willis Clay was found on the upthrown side of the fault and showed a lower resistivity. The fault plane was determined to be at the proximity of the intersection of the Lissie Sand and the Willis Clay. The Lissie Sand also appears to be pinching out above the Willis Clay on the upthrown side of the fault. The total depth of investigation was 3.83 meters.

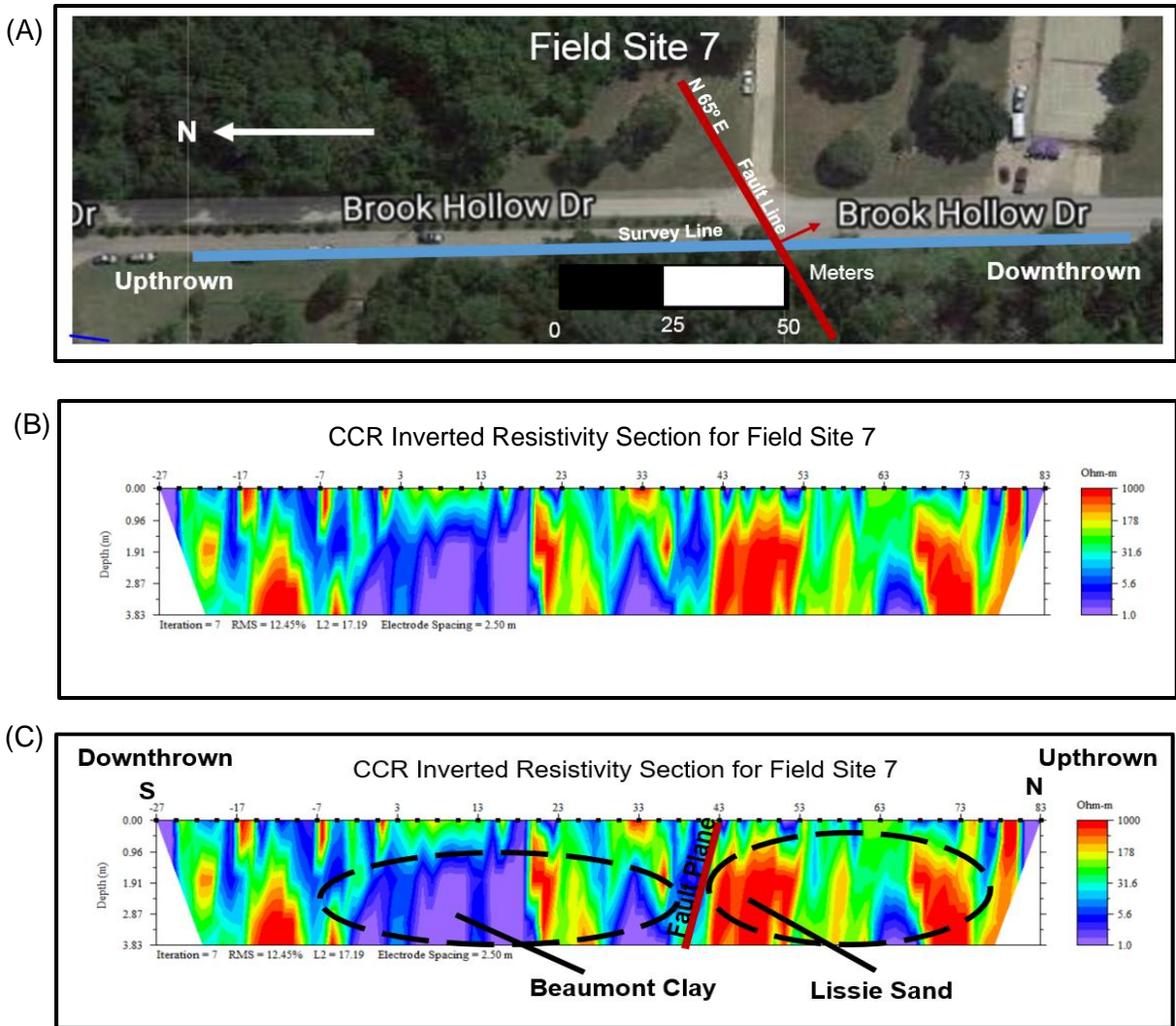
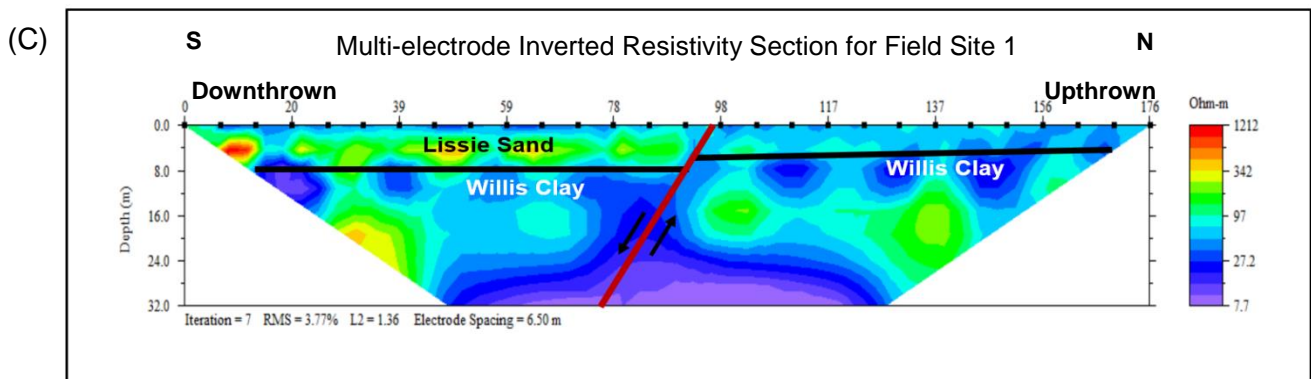
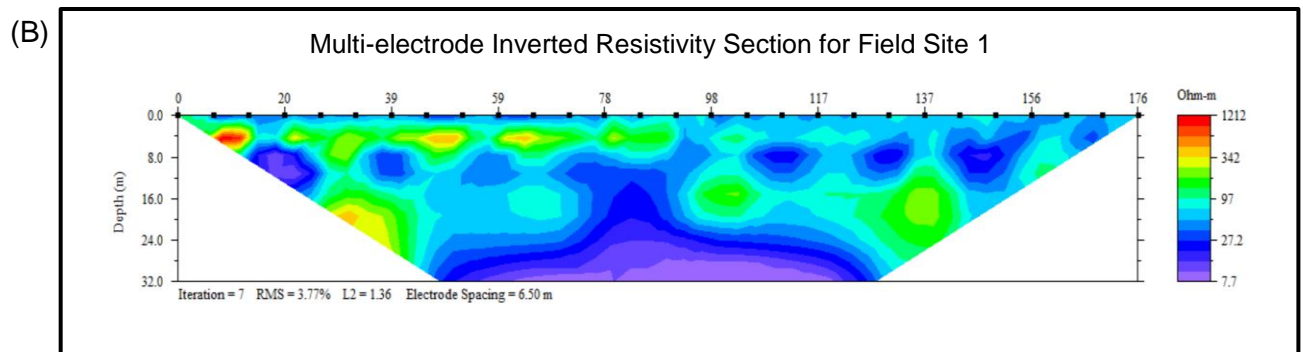
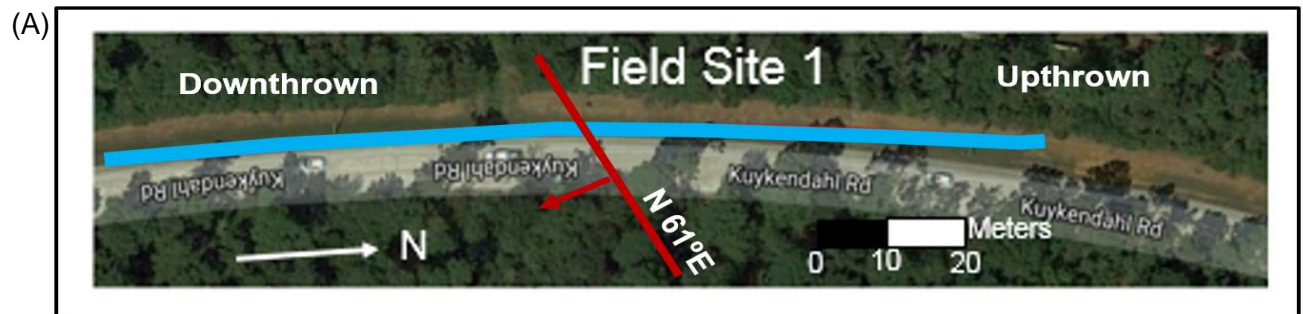


Figure 54. CCR Survey Site 7 Data

(A.) CCR survey site 7 with the fault line and survey line outlined (B.) inverted resistivity section for field site 7. (C.) Interpretation of inverted resistivity section from CCR survey site 7. The downthrown side of the fault line showed a lower resistivity while the upthrown side of the fault showed a higher resistivity which is opposite of the trend in CCR survey site 2 and 3. This change in lithology could be due to the nearby San Jacinto river that is located to the Northeast of the study area. Clays from the Beaumont Formation could have accumulated on the downthrown side of the fault. The Lissie Sand was found on the upthrown side of the survey line, but it could also be found deeper on the downthrown side of the fault. The total depth of investigation was 3.83 meters.

5.3 MULTI-ELECTRODE RESISTIVITY

The third geophysical technique used in this study utilized multi-electrode resistivity and was conducted using the R2 SuperSting resistivity meter. The SuperSting resistivity meter used electrical resistivity to delineate deeper subsurface features than the OhmMapper resistivity meter. The OhmMapper resistivity meter had a maximum depth of four meters while the SuperSting had a maximum depth of 32 meters. Multi-electrode resistivity was used at field sites 1, 2, 5 and 7. The data collected from the SuperSting resistivity meter at each field location is shown below (Figures 55-59).



55. Multi-electrode Resistivity Survey Site 1

(A) Multi-electrode Resistivity survey site 1 with the fault line highlighted in blue red and the survey line highlighted in blue. (B) Inverted resistivity section from survey site 1 (C) Interpretation of the inverted resistivity section. Higher resistivity readings were shown in red, while lower resistivity readings were shown in blue. The upper most lithologic unit in this area was the Lissie sand and was in higher accumulation on the downthrown side of the fault. The Willis Clay laid conformably underneath the Lissie Sand with offset in the layers in the vicinity of the fault plane. The approximated offset of the Willis Clay was found to be 2.8 meters. The Lissie Sand pinches out to the North on the uplifted side of the fault. The maximum depth of the survey was 32 meters.

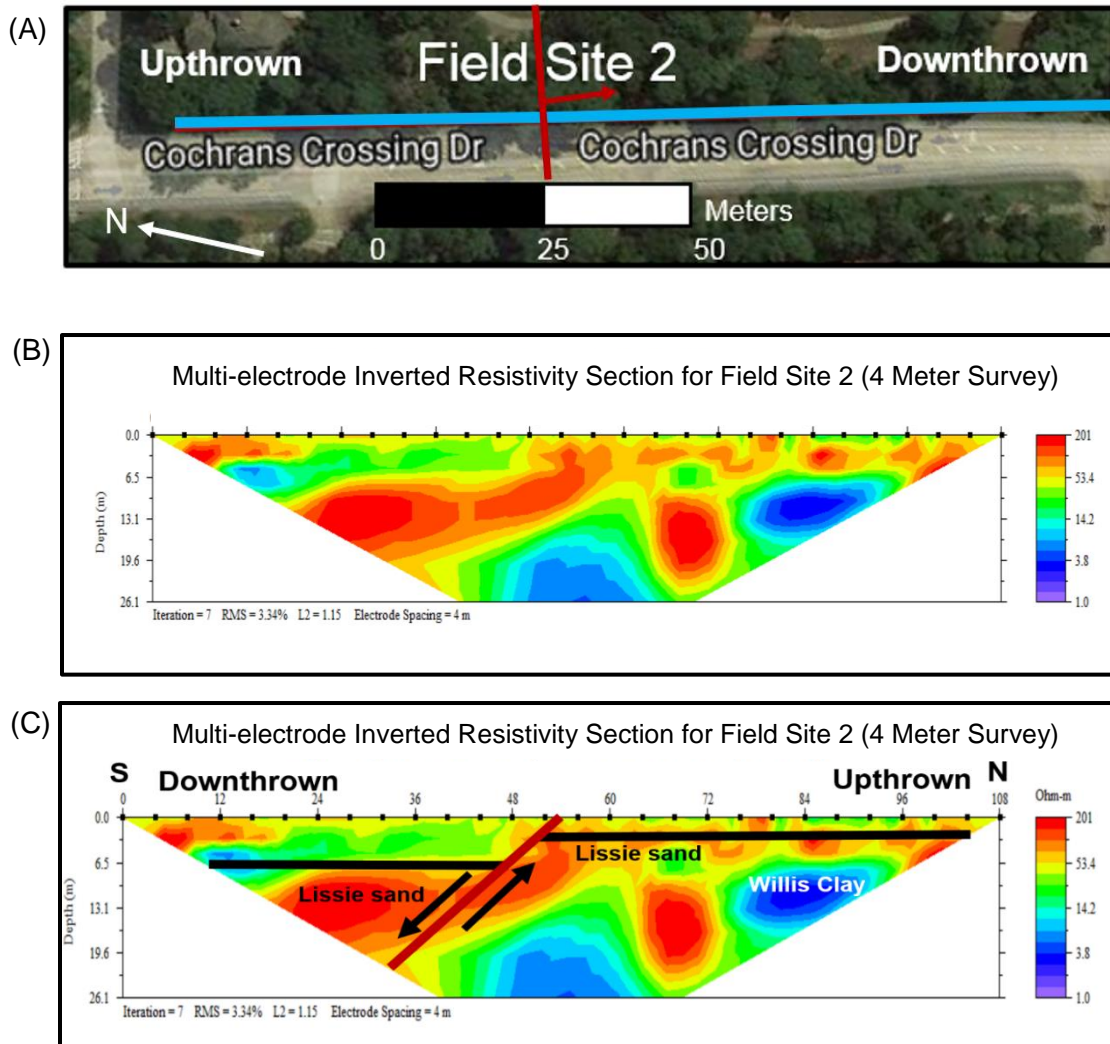
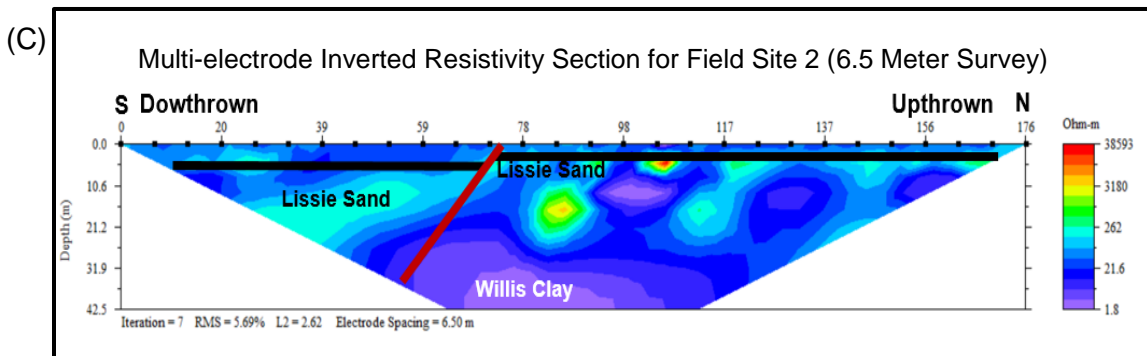
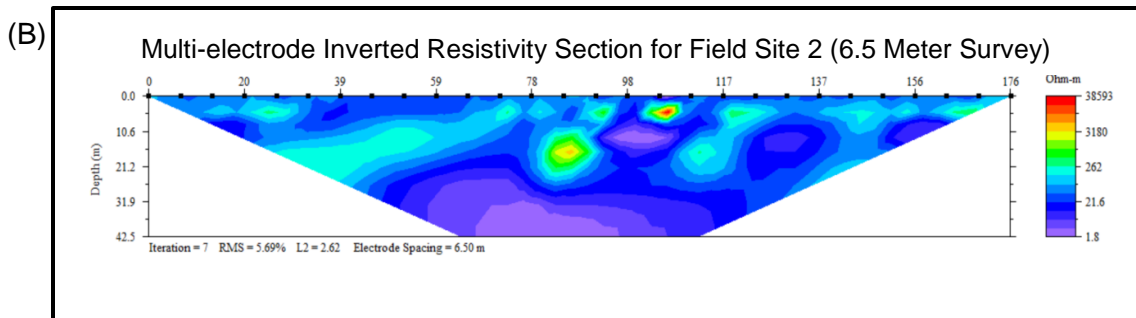
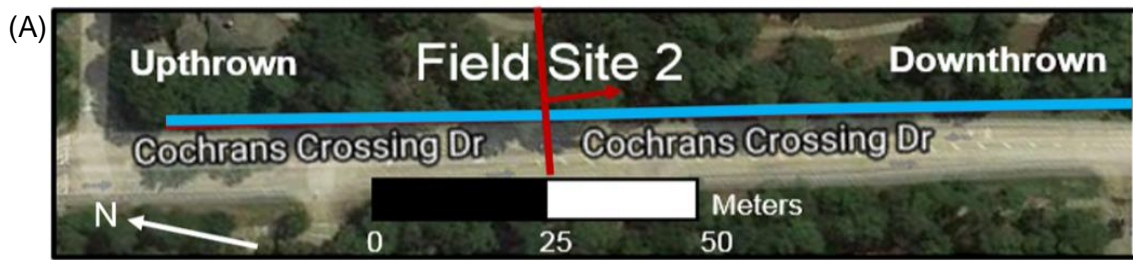


Figure 56. Multi-electrode Resistivity Survey Site 2 (4 Meter Survey)

(A) Multi-electrode resistivity survey site 2 with a NW-SE trending survey line shown in blue and a NE striking fault trend shown in red. (B) Inverted resistivity section from field site 2, with higher resistivity readings shown in red and lower resistivity readings shown in blue. The electrode spacing for this survey was set to 4 meters. (C) Interpretation of inverted resistivity section from field site 2. A normal fault was found near the center of the survey line with the Lissie Sand being dropped down to the South. The Willis Clay was found on the upthrown side of the fault line with an interfingering of the Lissie Sand. The offset of the Lissie Sand at this field site was found to be 2 meters. The total depth of this survey was 26.1 meters.



57. Multi-electrode Resistivity Survey Site 2 (6.5 Meter Survey)

(A) Multi-electrode resistivity survey site 2 with the NW-SE trending survey line outlined in blue and the NE trending fault line outlined in red. (B) Inverted resistivity section for field site 2 with higher resistivity readings shown in red and lower resistivity readings shown in blue. The electrode spacing for this survey was set to 6.5 meters. (C) Interpretation of inverted resistivity section from field site 2. A normal fault was found near the center of the survey line with the Lissie Sand being dropped down to the South. The Willis Clay was found on the upthrown side of the fault line with an interfingering of the Lissie Sand. The offset of the Lissie Sand at this field site was found to be 2 meters. The total depth of this survey was 26.1 meters.

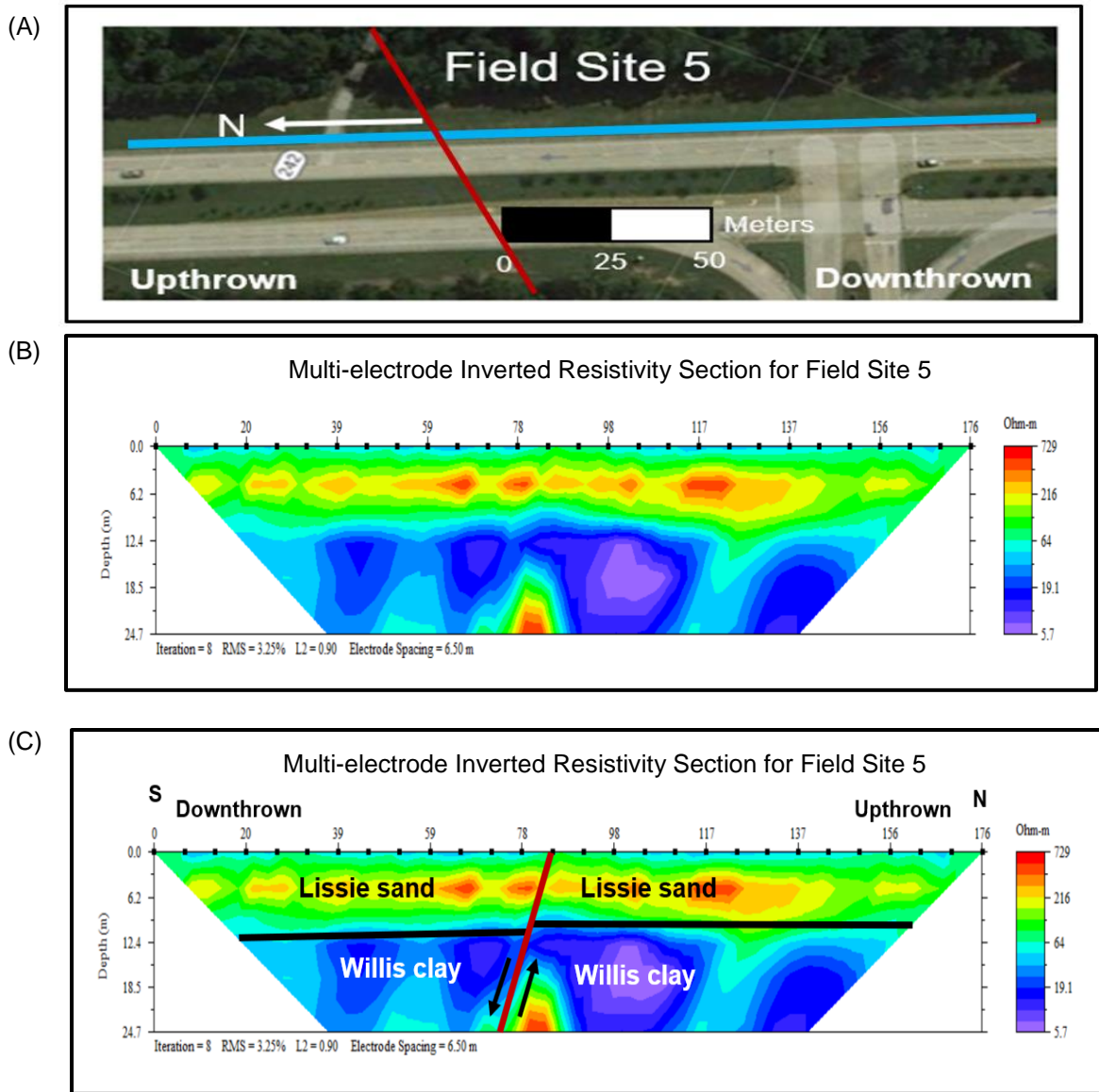


Figure 58. Multi-electrode Resistivity Survey Site 5

(A) Multi-electrode resistivity survey site 2 with the NW-SE trending survey line outlined in blue and the NE trending fault line outlined in red. (B) Inverted resistivity section for field site 2 with higher resistivity readings shown in red and lower resistivity readings shown in blue. The electrode spacing for this survey was set to 6.5 meters. (C) Interpretation of inverted resistivity section from field site 2. A normal fault was found near the center of the survey line with the Lissie Sand being dropped down to the South. The Lissie Sand was found to lie conformably above the Willis Clay. The offset of the layers was found to be 2 meters. The total depth of this survey was 26.1 meters.

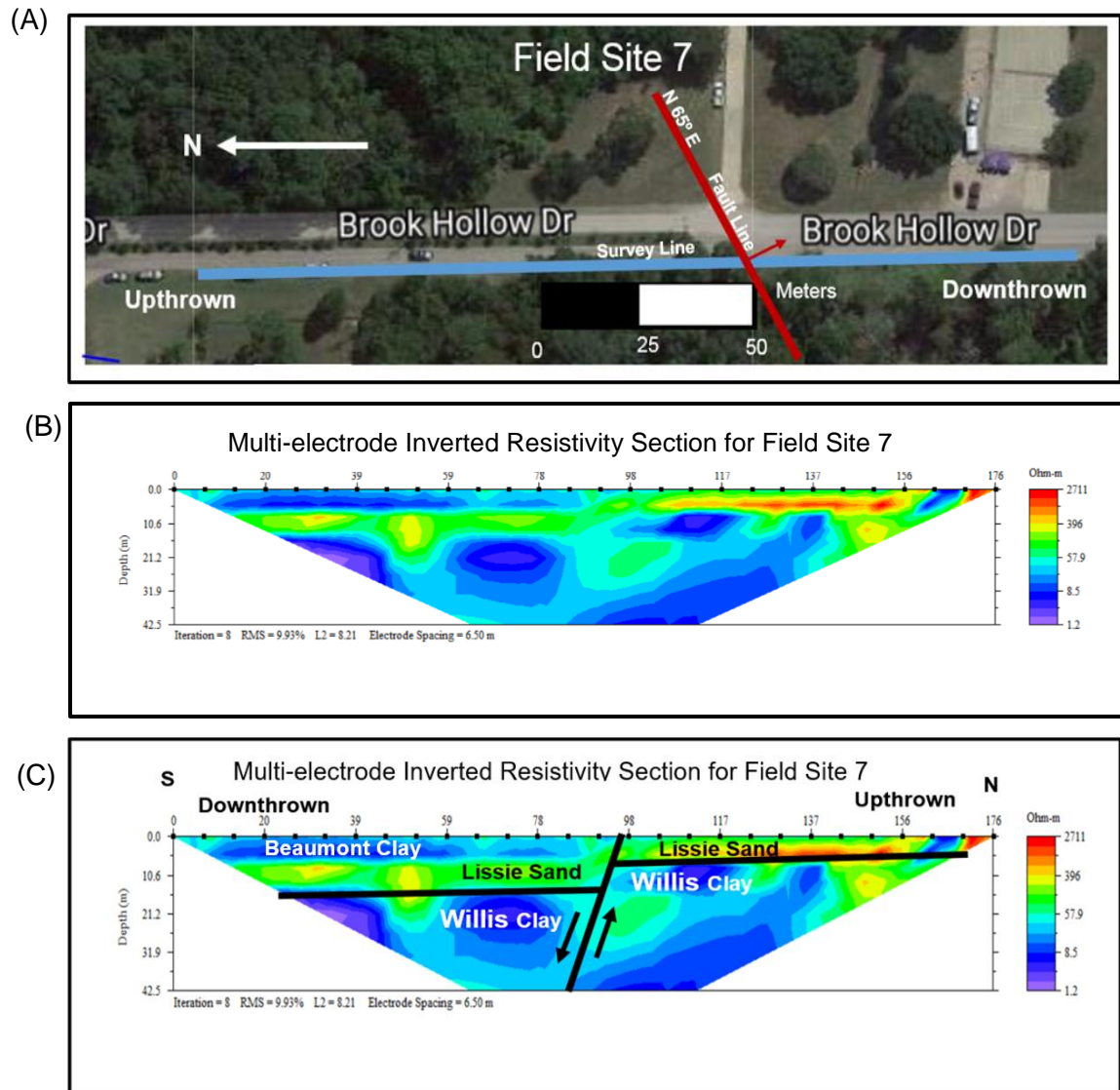


Figure 59. Multi-electrode Resistivity Survey Site 7

(A) Multi-electrode resistivity survey site 2 with the NW-SE trending survey line outlined in blue and the NE trending fault line outlined in red. (B) Inverted resistivity section for field site 2 with higher resistivity readings shown in red and lower resistivity readings shown in blue. The electrode spacing for this survey was set to 6.5 meters. (C) Interpretation of inverted resistivity section from field site 2. A normal fault was found near the center of the survey line with the Lissie Sand being dropped down to the South. The Lissie Sand was found to lie conformably above the Willis Clay and the offset of the layers was found to be 5 meters. The total depth of this survey was 42.5 meters.

CHAPTER 6

6.0 DISCUSSION

For this study gravity and electrical resistivity methods were used to delineate the Big Barn fault in Montgomery County, Texas. After examining existing geologic maps and through gravity and electrical resistivity techniques, the Big Barn fault was interpreted to truncate the Lissie Sand and the Willis Clay. Gravity data showed that the majority of the field sites (field sites 1, 2, 3, 4 and 5) showed a higher gravity on the downthrown side of the fault than on the upthrown side of the fault. The downthrown side of the fault was interpreted to contain higher accumulations of the Lissie Sand. Since sandstones are generally denser than claystones, they will naturally result in higher gravity readings. Electrical resistivity correlated well to the gravimetry data and also showed that the downthrown side of the fault had a higher resistivity consistent with the Lissie Sand, while the upthrown side of the fault had a lower resistivity consistent with the Willis Clay. The offset between the Lissie Sand and Willis Clay was found in field sites 1, 2, 5 and 7 through multi-electrode electrical resistivity techniques. Interpretations of the data collected at different field sites are discussed below.

Field Site 1

Field site 1 (Figure 60) utilized gravity and multi-electrode resistivity techniques to delineate faulting. At this field site, the downthrown side of the fault had higher gravity readings than the upthrown side. This contrast in gravity readings was likely due to a higher accumulation of the denser Lissie Sand on the downthrown side of the fault. The upthrown side of the fault had a higher accumulation of the less dense Willis Clay. Through multi-electrode resistivity imaging, a two-dimensional inverted resistivity section was created. The Lissie Sand was shown as light green- red in color and represented a higher resistivity. The Willis Clay was shown as light purple-blue in color and represented a lower resistivity. A normal fault offset the Lissie Sand and Willis Clay by 2 meters and the total survey depth was 32 meters.

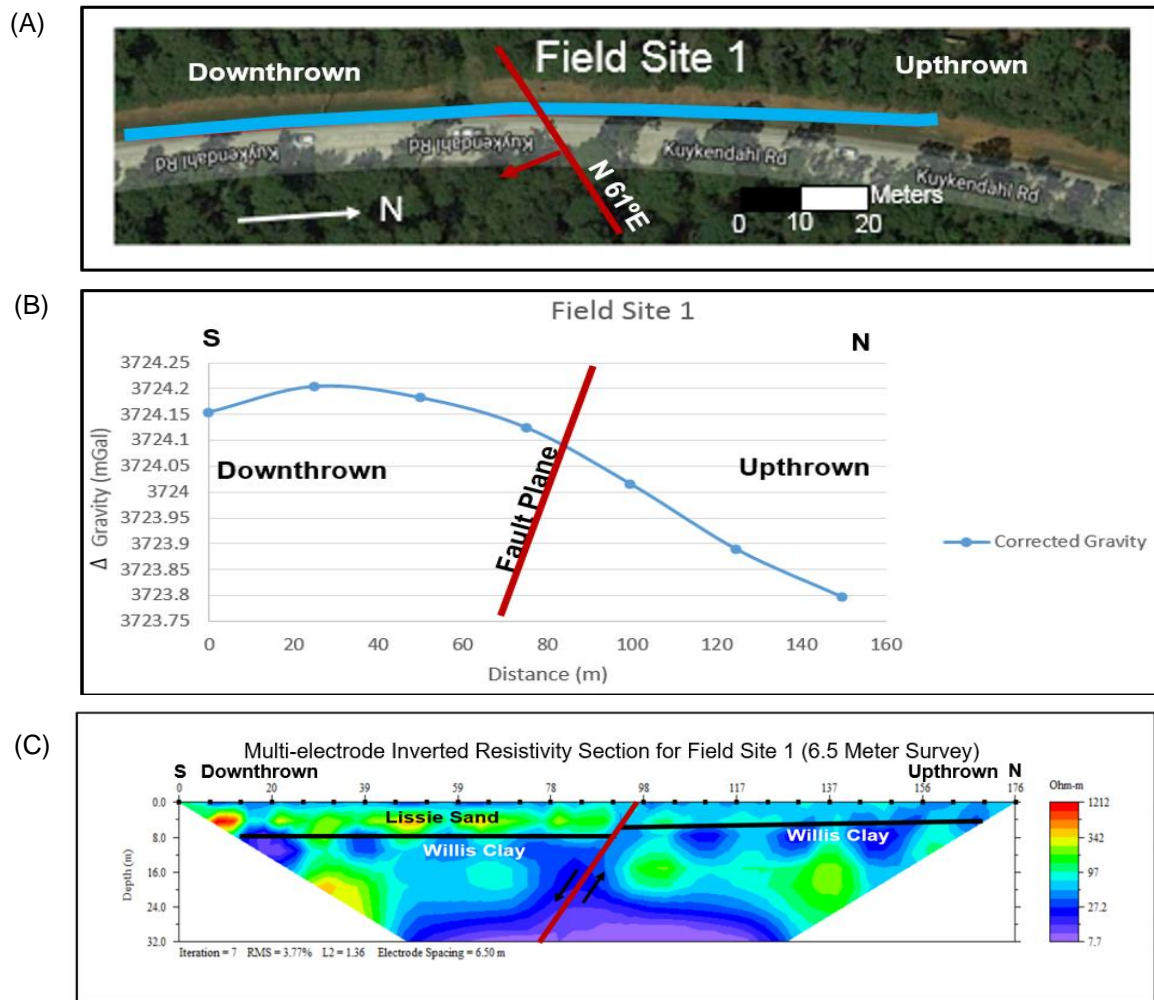


Figure 60. All Geophysical Data from Field Site 1

(A) Field Site 1 is shown with a NW-SE trending survey line highlighted in blue and a N61°E trending fault line shown in red. (B) Gravity readings from field site 2. (C) 4-meter multi-electrode inverted resistivity section (D) 6.5-meter multi-electrode inverted resistivity section.

Field Site 2

Field site 2 (Figure 61) utilized gravimetry, capacitively coupled resistivity and multi-electrode resistivity techniques to delineate the faulting. Gravimetry readings from field site 2 showed a higher gravity on the downthrown side of the fault and a lower gravity on the upthrown side of the fault. Capacitively coupled resistivity readings were displayed as an inverted resistivity section and had a total depth of 3.8 meters. The capacitively coupled inverted resistivity section showed a higher accumulation of the Lissie Sand on the downthrown side of the fault and a higher accumulation of the Willis Clay on the upthrown side of the fault. The multi-electrode inverted resistivity section showed the Lissie Sand in higher accumulation on the downthrown side of the fault and the Willis Clay in higher accumulation on the upthrown side of the fault. The offset of the layers was found to be 2 meters at this field site. A small accumulation of the Lissie Sand was found in the center of the survey line and is reflected in the gravity data with higher readings and in the multi-electrode inverted resistivity section with higher resistivity readings.

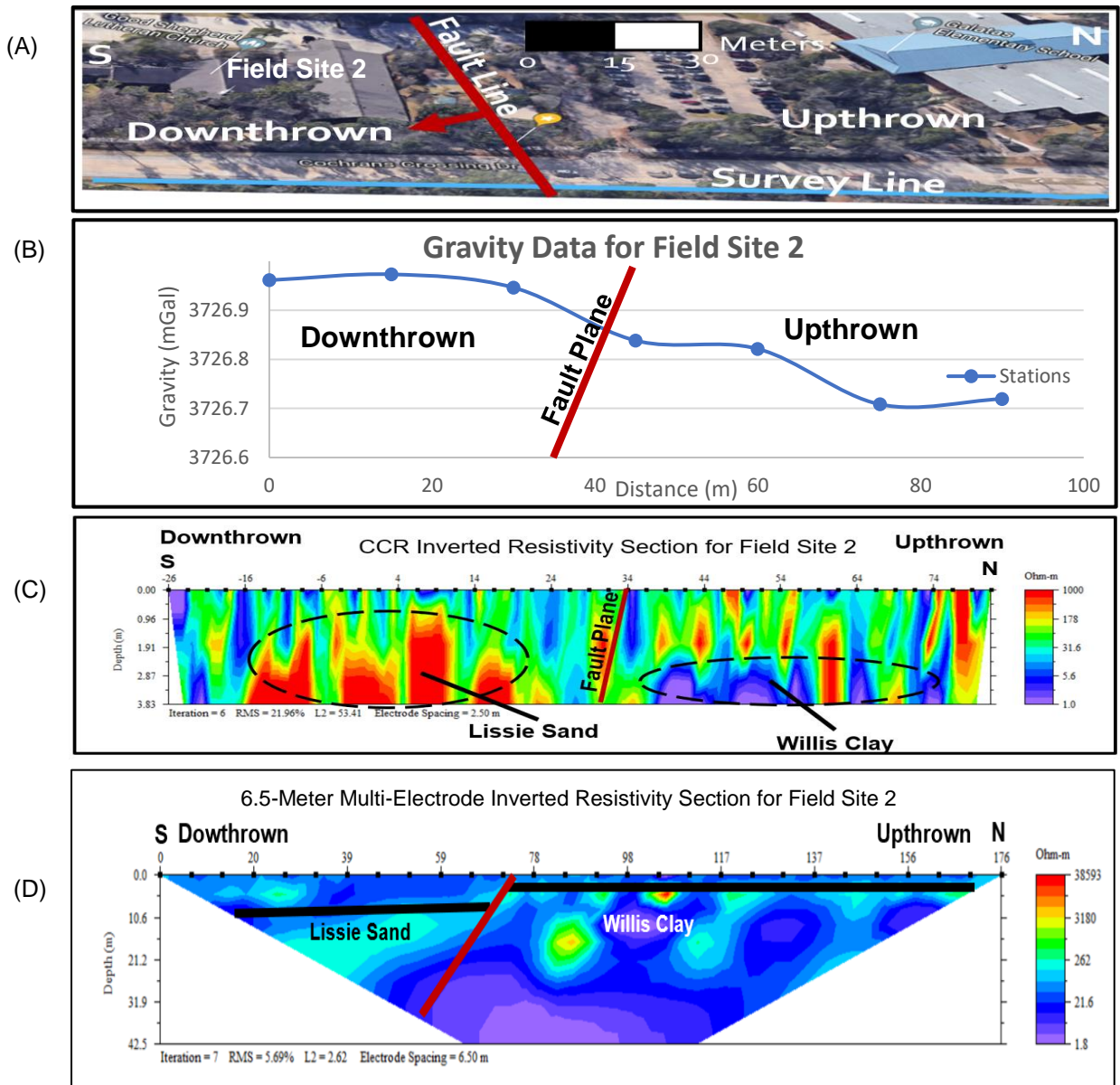


Figure 61. All Geophysical Data from Field Site 2

(A) Survey site 2 with the NW-SE trending survey line highlighted in blue and a N58°E trending fault line highlighted in red. (B) Plotted gravimetry readings from field site 2 (C) CCR inverted resistivity section (D) Multi-electrode inverted resistivity section.

Field Site 3

Field Site 3 (Figure 62) utilized gravity and capacitively coupled resistivity techniques to delineate the fault line. Plotted gravimetry readings from field site 3 showed higher gravity readings on the downthrown side of the fault and lower gravity readings on the upthrown side of the fault. Capacitively coupled resistivity section with the Lissie Sand found in higher accumulation on the downthrown side of the fault and the Willis Clay in higher accumulation on the upthrown side of the fault. The total depth of the capacitively coupled resistivity survey was 3.83 meters. The plotted gravimetry readings correlated well with the capacitively coupled resistivity section for field site 3.

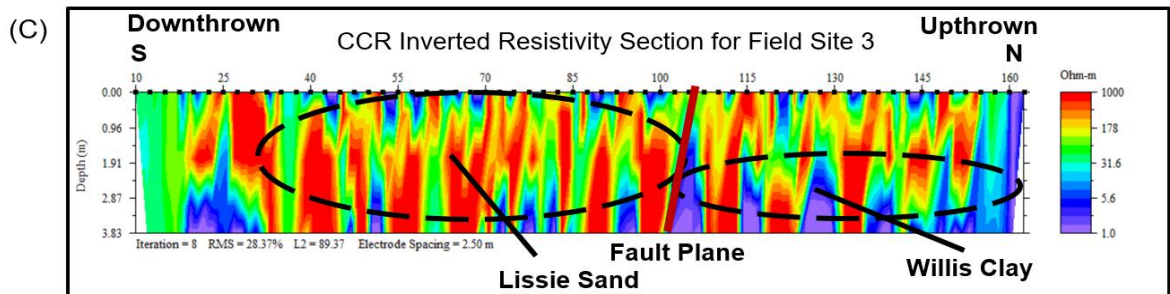
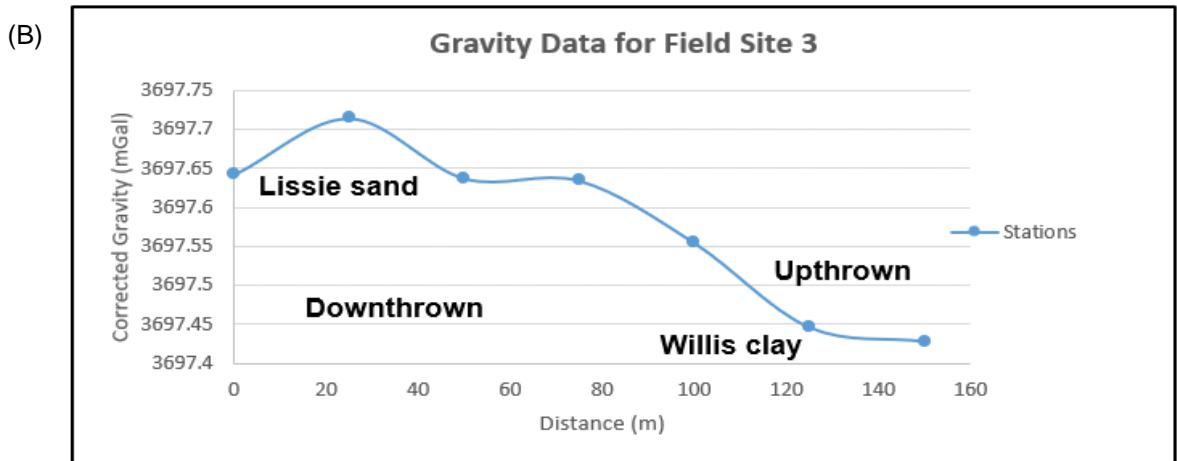
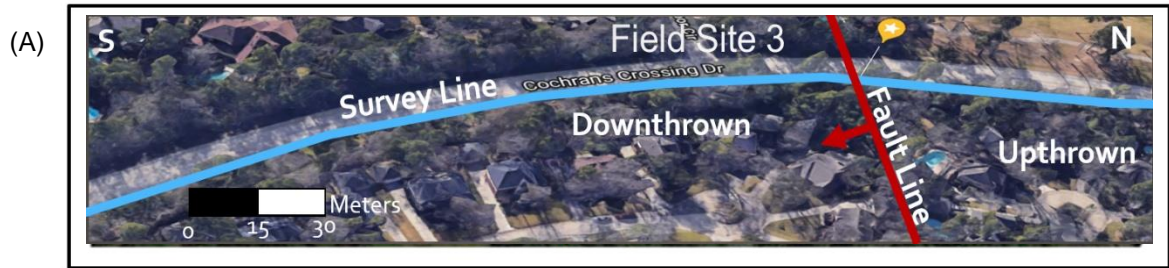


Figure 62. All Geophysical Data from Field Site 3

(A) Survey site 3 with the NW-SE trending survey line highlighted in blue and the N66°E trending fault line highlighted in red. (B) Gravimetry readings from field site 3. (C) Capacitively-coupled inverted resistivity section.

Field Site 4

Field site 4 (Figure 63) only utilized gravimetry readings to delineate the fault. Anthropogenic barriers such as busy roadways, businesses and residences prevented any electrical resistivity techniques to be used at this field site. Using gravimetry, it was determined that the downthrown (southern) side of the fault had higher gravity readings than the (northern) upthrown side of the fault. The denser Lissie Sand was found to be in higher accumulation on the downthrown side of the fault and the less dense Willis Clay was found in higher accumulation on the upthrown side of the fault.

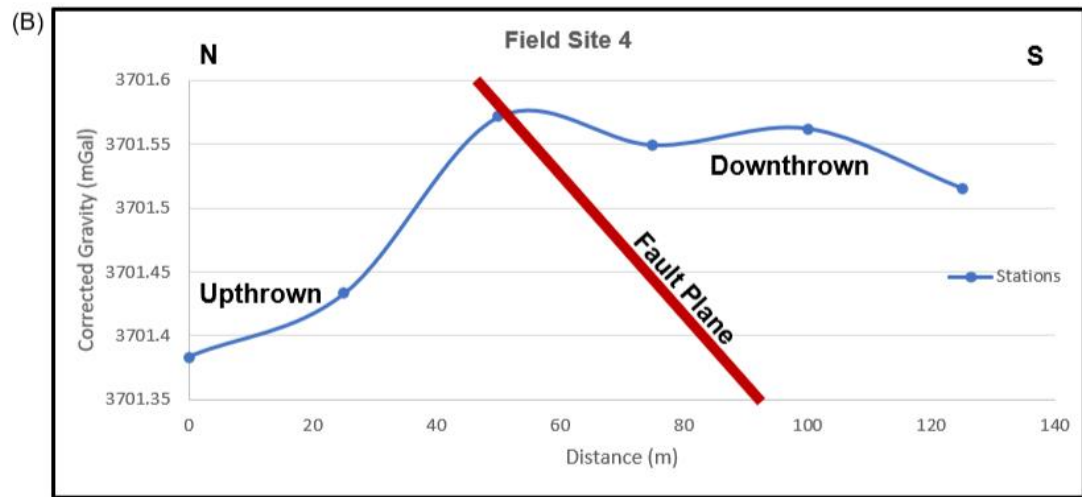
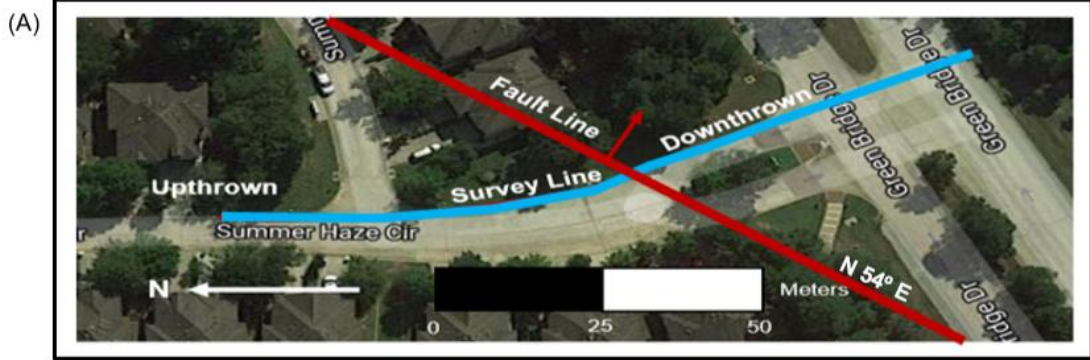


Figure 63. All Geophysical Data from Field Site 4

(A) Study area for field site 2 with the N54°E trend of the fault line highlighted in red and the survey line highlighted in blue. (B) Plotted gravimetry readings from field site 4.

Field Site 5

Field site 5 (Figure 64) utilized gravimetry and multi-electrode electrical resistivity techniques to delineate the fault. The plotted gravimetry readings with the upthrown side of the fault were found to have slightly lower gravity readings than the upthrown side of the fault. The lowest gravity readings were found in the center of the survey. The multi-electrode inverted resistivity section showed the Lissie Sand being the upper lithologic unit and the Willis Clay lying conformably underneath it. Normal faulting offset the Willis Clay and Lissie Sand by 2 meters. The changes in gravity match the faulting patterns shown in the inverted resistivity section. The anomalously low gravity readings at the center of the survey corresponded well to the multi-electrode electrical resistivity inverted resistivity section.

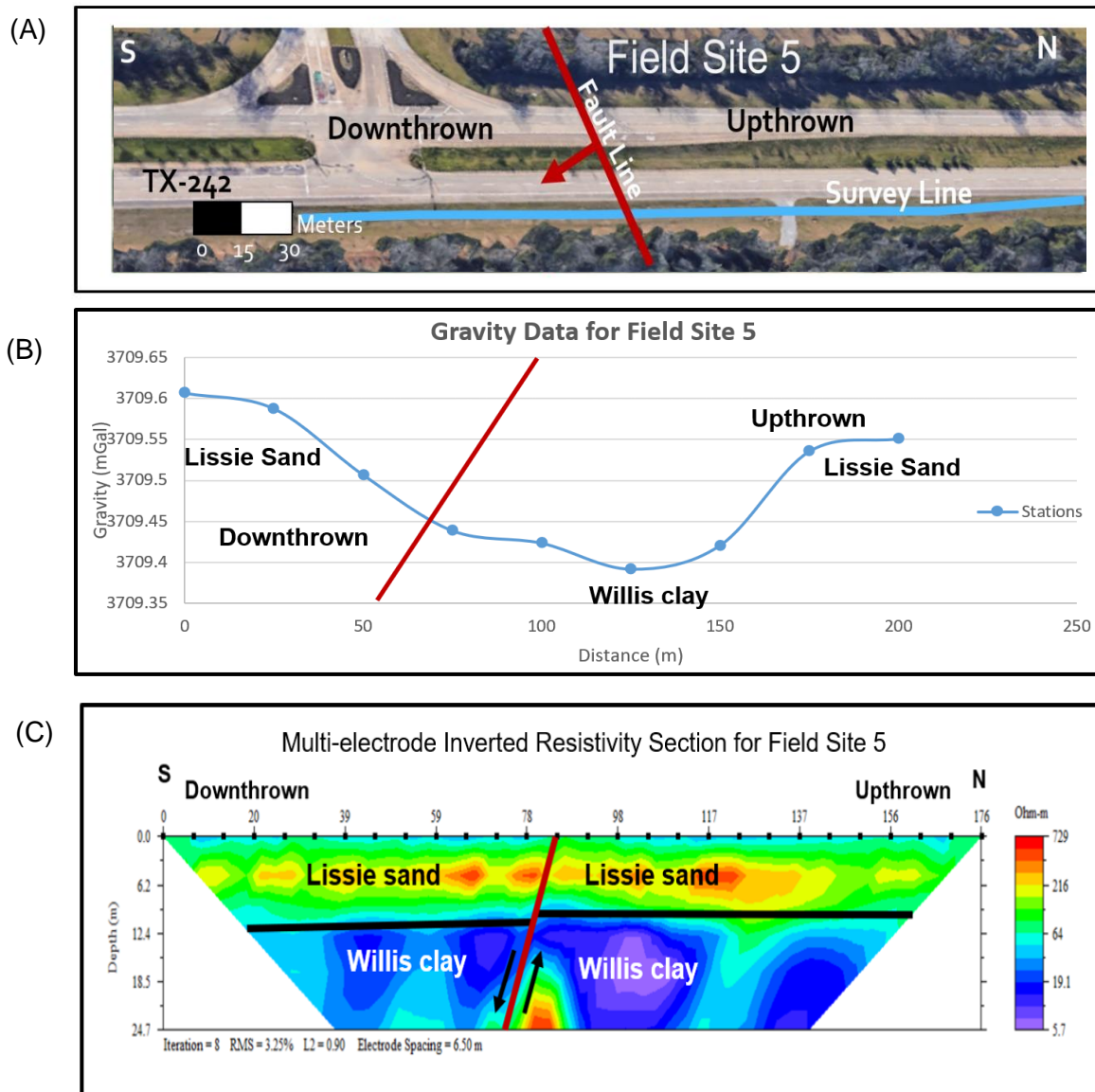


Figure 64. All Geophysical Data from Field Site 5

(A) Field site 5 with the N-S trending survey line highlighted in blue and the N65°E trending fault line highlighted in red. (B) Plotted gravimetry readings. (C) Multi-electrode inverted resistivity section.

Field Site 6

Field site 6 (Figure 65) only utilized gravimetry techniques due to the field site being located on the frontage road of Interstate Highway 45. Commercial driveways intersected the prospective survey line so neither electrical resistivity technique could be utilized. Using gravimetry techniques, it was determined that the downthrown side of the fault had higher gravity readings than the upthrown side of the fault. The denser Lissie Sand was found to be in higher accumulation on the downthrown side of the fault and the less dense Willis Clay was found in higher accumulation on the upthrown side of the fault. Anomalously high gravity readings were found near the center of the survey, which is also where the suspected fault line crossed the survey line. This anomaly could be due to a higher concentration of Lissie Sand near the fault plane, but further studies should be done to confirm this.

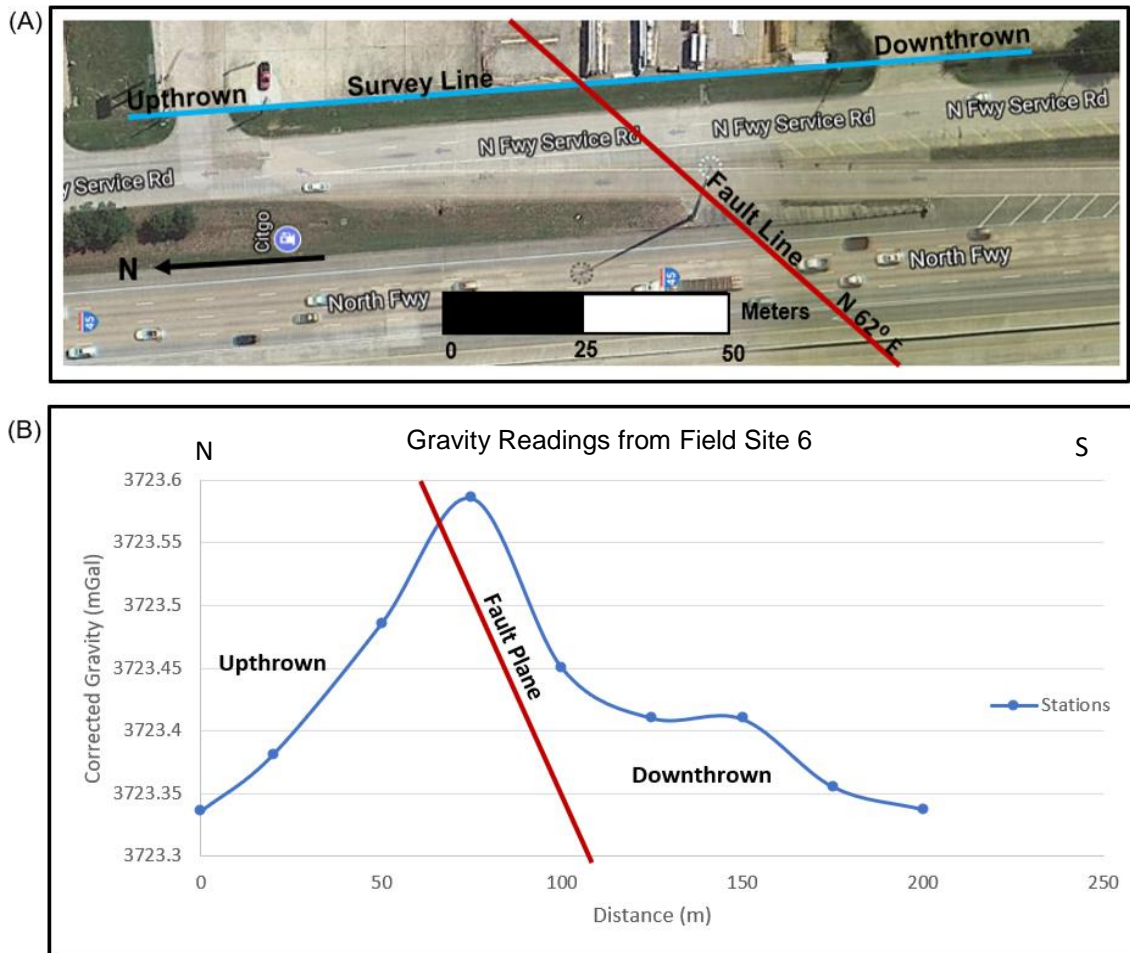


Figure 65. All Geophysical Data from Field Site 6

(A) Study area for field site 6 with the N62°E trend of the fault line highlighted in red and the survey line highlighted in blue. (B) Plotted corrected gravity data from field site 6.

Field Site 7

Field site 7 (Figure 66) utilized capacitively coupled electrical resistivity techniques and multi-electrode resistivity techniques to delineate the fault. Gravimetry techniques were not utilized at this field site due to equipment malfunctions in the field. The capacitively coupled inverted resistivity section showed higher resistivity Lissie Sand on the upthrown side of the fault and the lower resistivity Beaumont Clay on the downthrown side of the fault. The depth of the survey was 3.83 meters. The multi-electrode inverted resistivity section corresponded well to this and showed the Beaumont Clay as the upper geologic unit on the downthrown side of the fault and the Lissie Sand as the upper geologic unit on the upthrown side of the fault. The fault was determined to be a normal fault dipping toward the Gulf of Mexico. The Lissie Sand and Willis Clay were offset at this field site by 5 meters. The depth of the survey was 42.5 meters.

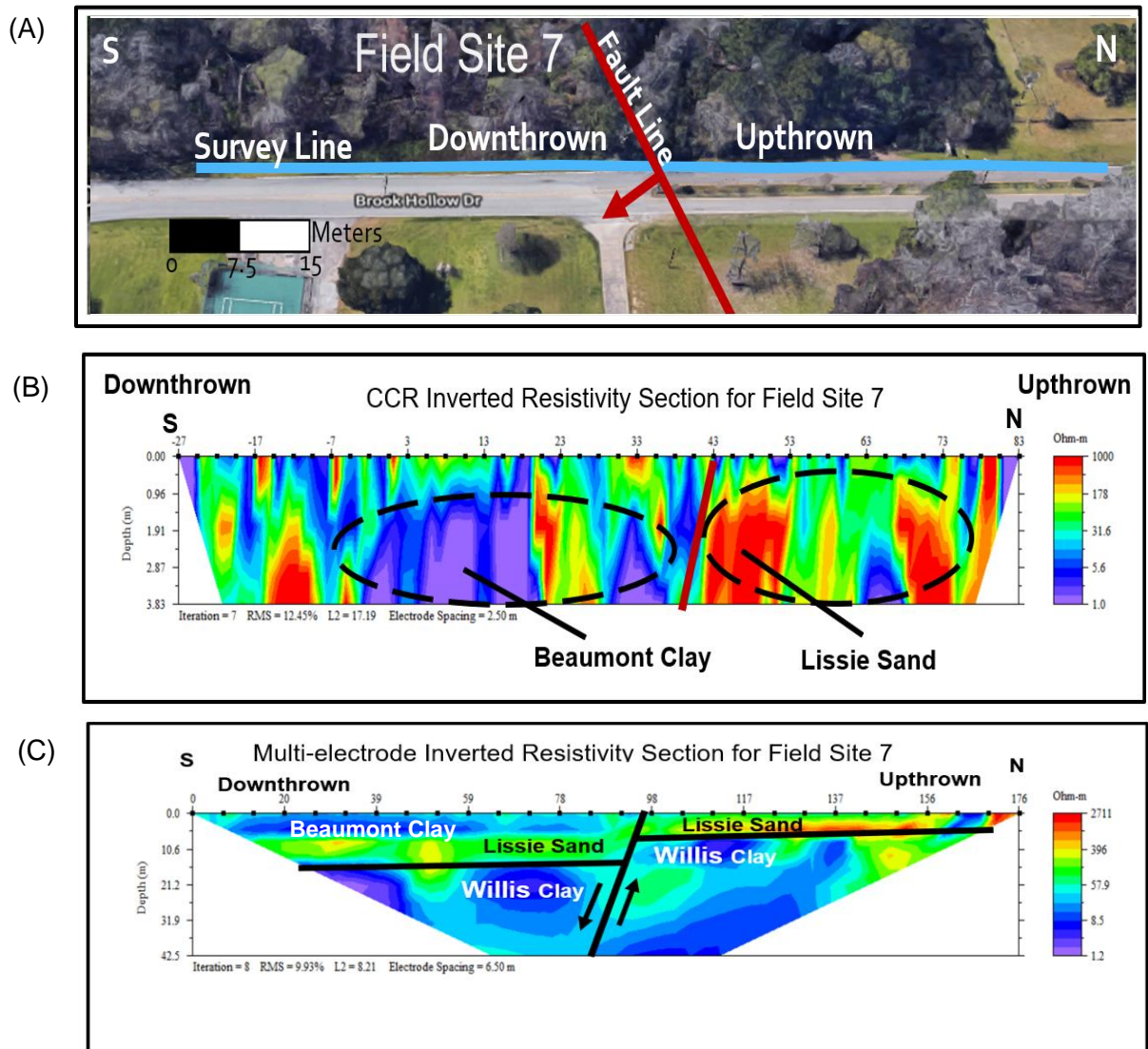


Figure 66. All Geophysical Data from Field Site 7

(A) Field site 7 with the NW-SE trending survey line highlighted in blue and the N65°E trending fault line highlighted in red. (B) CCR inverted resistivity section (C) Multi-electrode inverted resistivity section.

CHAPTER 7

7.0 LIMITATIONS

The field sites for this study were all located in urban environments which caused many challenges in conducting geophysical field work. Some field sites were located on busy roadways, such as field site 6 which was located on the frontage road of Interstate Highway 45. Field site 6 was limited to using gravimetry techniques because of these anthropogenic barriers and problems with gaining access to private properties. Capacitively coupled resistivity techniques could only be used on three field sites because of anthropogenic barriers such as woods or busy driveways. The OhmMapper resistivity meter is a very long apparatus that had to be pulled by the surveyor, which caused further limitations in line length and survey location. The RMS error associated with capacitively coupled resistivity techniques was higher than the multi-electrode resistivity techniques which could have been caused by variance in the field setup. Since the equipment for the capacitively coupled resistivity surveys were being towed, any bump or depression in the roadways could have caused extra noise in the survey.

7.1 CONCLUSION

For this study the Big Barn fault was examined using electrical resistivity and gravimetry techniques. Seven field sites were examined in total and each site used varying methodologies to delineate the fault and define the geology of the upper rock units. All field sites showed significant fractures in roadways along with a sharp contrast in elevation from the upthrown side of the fault to the downthrown side. The N62°E trending fault line was interpreted to trend along the same strike as the intersection of the Lissie Sand and Willis Clay, in most cases.

Gravimetry techniques were first used to delineate the fault because of the varying densities of the Lissie Sand and Willis Clay. The Lissie Sand was denser than the Willis Clay, so it had higher gravity readings. The gravity data was compared to the electrical resistivity data to determine the subsurface features in each field sites. The capacitively coupled and multi-electrode electrical resistivity data correlated well to the gravimetry data.

Field sites 1, 2, 5 and 7 showed a 2-5-meter offset between the interpreted Lissie Sand and Willis Clay. Field site 2 was the only field site that was able to utilize gravimetry, capacitively coupled resistivity and multi-electrode resistivity techniques to delineate the Big Barn fault and identify other subsurface features. All three geophysical techniques showed the Lissie Sand in higher accumulation on the downthrown side of the fault and the Willis Clay in higher

accumulation on the upthrown side of the fault. This corresponds to the geologic contact of the Lissie Sand and Willis Clay initially determined by previous geologic mapping. This truncation could have been caused normal faulting (Figure 4). Gravimetry and electrical resistivity data from the field sites correlated well and defined a higher resistivity anomaly in the Willis Clay on the upthrown side of the fault. Field sites 1 and 5 also showed an offset of the Lissie Sand and the Willis Clay layers in the proximity of a normal fault. Field site 7 showed the greatest offset of approximately 5m and showed a higher concentration of the Lissie Sand on the downthrown side of the fault and the Willis Clay on the upthrown side of the fault. For this field site another low resistivity layer was found to be above the Lissie Sand on the downthrown side which could be attributed to the field site's close location to the East Fork of the San Jacinto River. This layer was determined to be the Beaumont Clay. The USGS reported the Beaumont Clay in the same area as field site 7, which could account for the layer above the Lissie Sand.

7.2 FUTURE WORK

Future work could be done by utilizing more geophysical techniques along the fault line. Field investigations for this survey were extended past the seven field locations but anthropogenic barriers limited the extent of the study. More extensive field mapping could be done to more precisely define where the Lissie Sand truncates the Willis Clay and to determine the extent of the Beaumont Clay. Further work could be completed by extending the length of the fault line to the southwest and northeast.

Subsidence is a known problem in the Gulf Coastal Plain and could have been caused by a variety of factors. Conducting subsidence studies through time using LiDAR elevation maps could determine the reactivation of the fault line. Saribudak et. al., 2018, used LiDAR elevation maps along with other geophysical methods to further characterize the Hockley fault. Examining elevations in the study area throughout time could be useful in determining the timing of faulting, which could be correlated to a specific cause of reactivation. This timing could be correlated to subsidence rates in the city of Houston, which could be caused by anthropogenic or natural causes. To further prevent damages to residences, businesses and roadways it is important that continuous studies be done on faults throughout the greater Houston area to pinpoint the cause of reactivation of faulting and to map the true extent of the fault lines.

REFERENCES

- AGI, 2005. Instruction manual for the SuperSting with Swift automatic resistivity and IP system: Austin, TX, Advanced Geosciences, Inc., 87 p.
- AGI, 2017. Seminar on resistivity imaging, AGI Resistivity Imaging Seminar, Nov. 6-8, Austin, TX.
- Aronow, S., Fisher, W.L., McGowen, J.H., and Barnes, V.E. (V.E. Barnes, Project Director), 1982, Geologic atlas of Texas, Houston sheet: Austin, University of Texas, Bureau of Economic Geology, scale 1:250,000.
- Baker, E.T., 1994, "Stratigraphic Nomenclature and Geologic Sections of the Gulf Coastal Plains
- Barker, R. A., and Ardis, A. F., 1996, Hydrogeologic framework of the Edwards-Trinity Aquifer System, west-central Texas: U.S. Geological Survey Professional Paper 1421-B, 61 p. with plates of Texas" U.S. Geological Survey Open-File Report 94-461.
- Ball, L., Kress, W., Steele, G., Cannia, J., and Andersen, M., 2004, Determination of canal leakage potential using continuous resistivity profiling techniques, Interstate and Tri-State Canals, Western Nebraska and Eastern Wyoming: U.S. Department of the Interior, U.S. Geological Survey Open-File Report 2006-5032, p. 8.
- Barton, D.C., Ritz, C., and Hickey, M., 1933, Gulf Coast geosyncline: Am. Assoc. Petroleum Geologists Bull., v. 17, p. 1446-1458.
- Bates, R.L., and Jackson, J.A., 1984, Dictionary of geologic terms: The American Institute, Anchor Books, New York.
- Bauer, P., 1999, The Gravity Geophysical Method, Astronaut Geophysical Training, New Mexico Bureau of Geology and Mineral Resources, New Mexico Technical University, https://geoinfo.nmt.edu/geoscience/projects/astronauts/gravity_method.html.
- Bebout, D.G., Luttrell, P.E., and Seo, J.H., 1976, Regional Tertiary cross sections Texas Gulf Coast: Austin, University of Texas, Bureau of Economic Geology Geological Circular 76-5, 10 p.
- Beckman, J.D. and Williamson, A.K., 1990, Salt-Dome Locations in the Gulf Coastal Plain, South-Central United States, U.S. Geological survey water-Resources Investigations Report 90-4060.

- Berryhill, H.L., Jr., Suter, J.R., and Hardin, N.S., 1987, Late Quaternary Facies and Structure, Northern Gulf of Mexico Interpretations from Seismic Data, American Association of Petroleum Geologists Studies in Geology no. 23, 289 p.
- Billings, M.P., 197, Structural Geology, 3rd Edition, London, Prentice-Hall International, Inc, ISBN: 0-13-853846-8, print.
- Bird, D., Burke, K., Hall, S., and Casey, J., 2005, Gulf of Mexico Tectonic History: Hotspot Tracks, Crustal Boundaries, and Early Salt Distribution, American Association of Petroleum Geologists Bulletin, v. 89, p. 311–328, doi: 10.1306/10280404026.
- Blakey, R., 2016, Paleogeography and Geologic Evolution of North America: www.jan.ucc.nau.edu/rcb7/nam.html. Accessed April, 10 2016.
- Braile, L.W., Hinze W.J., Geller G.R., Lidiak E.G., and Sexton J.L., 1986 Tectonic Development of the New Madrid Rift Complex, Mississippi Embayment, North America, Tectonophysics, 131, p. 1-21.
- Brun, J., and Mauduit, T., Rollovers in salt tectonics: The inadequacy of the listric fault model, 2008, Tectonophysics, 457, p. 1-11.
- Bureau of Economic Geology., 1992, Geology of Texas, University of Texas at Austin, 2 p.
- Byerly, G.R., 1991, Igneous activity, in Salvador, A., editor, The Gulf of Mexico Basin: Boulder, Colorado, Geological Society of America, The Geology of North America, v. J., p. 91-108.
- Cardimona, S., 2002, Electrical resistivity techniques for subsurface investigation: Department of Geology and Geophysics, University of Missouri Rolla, Rolla, MO, p. 1-10.
- Carpenter, P.J., 1997, Use of resistivity and EM Techniques to Map Subsidence Fractures in Glacial Drift, Association of Environmental and Engineering Geologists, v. 8, doi: 10.2113/gseegeosci.III.4.523.
- Campbell, M.D., Wise, H.M., and Bost, R.C., 2015, Growth Faulting and Subsidence in the Houston, Texas Area: Guide to the Origins, Relationships, Hazards, Potential Impacts and Methods of Investigation, Institute of Environmental Technology, Technical Report, doi: 10.13140.
- Chowdhury, A.H., Boghici, R., and Hopkins, J., 2006, Hydrochemistry, Salinity Distribution, and Trace Constituents: Implications for Salinity Sources, Geochemical Evolution, and Flow Systems Characterization, Gulf Coast Aquifer, Texas. Texas Water Development Board, Report R365, ch. 5.

- Doering, J., "Post Fleming Surface Formations of Coastal Southeast Texas and South Louisiana, Bulletin of the North American Association of Petroleum Geologists, Vol. 19. No. 5 (May, 1935), p. 651-688.
- Engelkemeir, R.E., and Khan, S.D., 2007, Near surface geophysical studies of Houston faults: The Leading Edge, v. 26, no. 8, p. 1004–1008, doi: 10.1190/1.2769557.
- Engelkemeir, R., S. Khan, and Kevin Burke, 2010, Surface Deformation in Houston, Texas using GPS, Tectonophysics, Vol. 490, p. 47–54.
- Ferrill, D.A., Morris, A., 2008, Fault Zone Deformation Controlled by Carbonate Mechanical Stratigraphy, Balcones Fault System, Texas, AAPG Bulletin 92(3):359-380.
- Fugro Consultants, Inc., 2012, Geologic Fault Delineation Study SJRA Distribution Lines, Route W1, San Jacinto River Authority, Montgomery County, Texas.
- Garrison, L.E., and Martin, R.G., Jr., 1973, Geologic structures in the Gulf of Mexico basin: U.S. Geological Survey Professional Paper 773, 85 p.
- Geometrics, Geophysical Methods, Capacitively Coupled Resistivity, <http://www.geometrics.com/applications/geophysical-methods/capacitively-coupled-resistivity/>.
- Halbouty, M. T., 1967, Salt Domes, Gulf Coast region, United States and Mexico: Gulf Publishing Company, Houston, Texas, 425 p.
- Hatherton, T., and Hunt, T.M., 1968, Gravity Profiles across the Alpine Fault, New Zealand, Journal of Geophysical Research, Vol. 73, No. 16, August 15, 1968.
- Hentz, T.F., and Zeng, H., 2003, High-frequency Miocene sequence stratigraphy, offshore Louisiana: Cycle framework and influence on production distribution in a mature shelf province, AAPG Bulletin, v. 87, no. 2 (February 2003), p. 197–230.
- Hosman, R.L., 1996, "Regional Stratigraphy and Subsurface Geology of Cenozoic Deposits, Gulf Coastal Plain, South-Central United States" U.S. Geological Survey Professional Paper 1416-G.
- Hosman, R.L. and Weiss, J.S., 1991, Geohydrologic units of the Mississippi Embayment and Texas Coastal Uplands Aquifer Systems, South-Central United States – Regional aquifer system analysis-G.
- Hudec, M. R., Norton N. O., Jackson, M. P. A., and Peel F. J., 2013, Jurassic evolution of the Gulf of Mexico salt basin: AAPG Bulletin, 97, p. 1683–1710, doi: 10.1306/04011312073.
- Jackson, M.P.A., 1982, Fault tectonics of the East Texas Basin: Texas Bureau of Economic Geology, Geologic Circular 82-4, Austin, p. 31.

- Khan, S.D., Stewart, R.R., Otoum, M., et. al., 2013, A geophysical investigation of the active Hockley Fault System near Houston, Texas, *Geophysics*, Vol. 78, No. 4, pp. B177-B185.
- Kneller, E. A., and C. A. Johnson, 2011, Plate kinematics of the Gulf of Mexico based on integrated observations from the Central and South Atlantic: *Gulf Coast Association of Geological Societies Transactions*, 61, p. 283–299.
- Kolay, K.K., Sandeep, B.G., and Sanjeev, K. 2016, Effect of Salt and NAPL on electrical resistivity of fine-grained soil-sand mixtures: *International Journal of Geotechnical Engineering*, pp. 1-7, doi:10.1080/19386362.2016.1239378.
- Loke, M.H., 1999, *Electrical imaging surveys for environmental and engineering studies: A practical guide to 2-D and 3-D surveys*. 63 p.
- Lowrie, W., 2007, *Fundamentals of Geophysics, Second Edition*: Cambridge University Press.
- Marton, G., and R. T. Buffler, 1994, Comment on Jurassic reconstruction of the Gulf of Mexico Basin: *International Geology Review*, 36, p. 545–586, doi: 10.1080/00206819409465475.
- Majzoub, A.F., 2016, *Characterization and Delineation of Karst Geohazards Along RM652 Using Electrical Resistivity Tomography, Culberson County, Texas*, Stephen F. Austin State University, Electronic Theses and Dissertations.
- McGookey, D.P., 1975, Gulf Coast Cenozoic sediments and structure: An excellent example of extra-continental sedimentation: *Gulf Coast Association of Geological Societies Transactions*, v. 25, p. 104-120.
- Metcalf, R.J., “Deposition of Lissie and Beaumont Formations of Gulf Coast of Texas”, *Bulletin of the American Association of Petroleum Geologists*, Vol. 24, No. 4 (April, 1940), p. 693-700.
- Moore, D.W. and Wermund, E.G., Jr., 1993a, Quaternary geologic map of the Austin 4 x 6 degree quadrangle, United States: U.S. Geological Survey Miscellaneous Investigations Series Map I-1420 (NH-14), scale 1:1,000,000.
- Mussett, A.E., and Khan, A.M., 2000, *Looking into the earth: An introduction to geological geophysics*: Cambridge, Cambridge University Press.
- Norman, C. E., and Britt, P.W., 1991, Active Faults in North Harris County and South Central Montgomery County, Texas, in *Environmental and Engineering Geology of North Harris and South Montgomery Counties, Texas*, Houston Geological Society Guidebook 91-1, Field Trip of October 19, p. 13-27.
- Norman, C.E., 2005, Ground subsidence and active faults in the Houston metropolitan area: Coastal subsidence, sea level and the future of the Gulf Coast: Houston Geological Society/Engineering, Science and Technology Council of Houston Conference, Field Trip Guide.

- Nguyen, L.C., and Mann, P., 2016, Gravity and magnetic constraints on the Jurassic opening of the oceanic Gulf of Mexico and the location and tectonic history of the Western Main transform fault along the eastern continental margin of Mexico, *Interpretation*, Vol. 4, No. 1 (February 2016); p. SC23–SC33.
- Okocha, F.C., 2016, Gravitational Study of the Hastings Salt Dome and Associated Faults in Brazoria and Galveston Counties, Texas, Master's thesis, Stephen F. Austin State University, <http://scholarworks.sfasu.edu/etds/80>.
- Oldani, M.J., 1986, Episodic Sedimentation in the Rio-Grande-Trans Pecos Region as Related to Periods of Tectonic Activity, Houston Geological Society, Field Seminar of the Big Bend, Trans-Pecos Region, Texas.
- Pindell, J. L., and Kennan L., 2009, Tectonic evolution of the Gulf of Mexico, Caribbean and northern South America in the mantle reference frame: An update, in K. H. James, M. A. Lorente, and J. L. Pindell, eds., *SC32 Interpretation / February 2016*, the origin and evolution of the Caribbean Plate: Geological Society of London, 1–5.
- Pratsch, J.C., 1997 Relationship of Gulf Coast Basement Tectonics to Present and Future Oil and Gas Fields, Houston Geological Society, June 1997 Issue.
- Rucker, D.F., Noonan, G.E., and Greenwood, W.J., 2011, Electrical resistivity in support of geological mapping along the Panama Canal, *Engineering Geology* 117, p. 121-133.
- Saribudak, M., 2011, Geophysical mapping of the Hockley growth fault in northwest Houston, USA, and recent surface observations, the Leading Edge, *Near-Surface Geophysics*, p. 936-943.
- Saribudak, M., Ruder, M., and Nieuwenhuise, B.V., 2018, Hockley Fault revisited: More geophysical data and new evidence on the fault location, Houston, Texas, *Geophysics*, Vol. 83, No.3, p. 1-10.
- Scintrex, 2008, CG-5 Scintrex Autograv System Operation Manual, part # 867700 Revision 5.
- Scintrex, 2012, www.scintrexltd.com [Retrieved December, 2017].
- Solis, R.F., "Upper Tertiary and Quaternary Depositional Systems, Central Coastal Plain, Soli Texas", 1981, Bureau of Economic Geology, Report of Investigations, No. 108.
- Stoneham, S. L., 1953, A Generalized Geologic North-South Cross Section from Hays County, Texas, to the Gulf of Mexico, Guidebook, A.A.P.G. Annual Meeting, Houston, Texas (March), p. 24-25.
- USGS, 2018, Geologic Units of Montgomery County, <https://mrdata.usgs.gov/geology/state/fips-unit.php?code=f48339>. [Retrieved January 2018].
- Telford, W.M., Geldart, L.P., and Sheriff, R.E., *Applied Geophysics*, Second Edition: Cambridge, Cambridge University Press, 1990.

- Thomas, W. A., 2011, The Iapetan rifted margin of southern Laurentia, *Geosphere*, vol. 7, p. 97-120.
- Thompson, W.C., 1937, Geologic sections in Texas and adjoining states: *American Association of Petroleum Geologists Bulletin*, v. 21, no. 8, p. 1,083-1,087.
- Trimble Inc., 2011, NOMAD 9000 Series Users Guide: www.Trimble.com [Accessed January, 2018].
- Van Sicken, D. C., 1967, The Houston fault problem: *American Institute of Professional Geologists, Texas Section: Third Annual Meeting Proceedings*, p. 9–31.
- Verbeek, E. R., 1978, Quaternary fault activity in Texas Gulf Coast: *American Association of Petroleum Geologists Bulletin*, v. 63, p. 545–545.
- Verbeek, E. R., and Clanton U. S., 1981, historically active faults in the metropolitan area, Texas, *Houston area environmental geology*, in E. M. Etter, ed., *Houston area environmental geology: Surface faulting, ground subsidence, and hazard liability: Houston Geological Society, Texas*, p. 28–68.
- Wada, S., Sawada, A., Hiramatsu, Y., et. al., 2017, Continuity of subsurface fault structure revealed by gravity anomaly: the eastern boundary fault zone of the Niigata plain, central Japan, *Earth, Planets and Space*, 69:15, doi: 10.1186/s40623-017-0602-x.
- Waters, P. W. McFarland, and J. W. Lea, 1955, Geologic Framework of Gulf Coastal Plain of Texas, *Bulletin, A.A.P.G. Vol. 39. NO. 9 (September, 1955)*. p. 1821-1850.
- Williamson, J.D.M., 1959, Gulf Coast Cenozoic history: *Gulf Coast Association of Geological Societies Transactions*, v. 9, p. 15-29.
- Winker, C.D., 1982, Cenozoic shelf margins, northwestern Gulf of Mexico: *Gulf Coast Association of Geological Societies Transactions*, v.32, p.427 – 448.
- Wood, D.H. and Giles, A.B., 1982, Hydrocarbon Accumulation Patterns in the East Texas Salt Dome Province, Bureau of Economic Geology, *Geological Circular*, 82-6.
- Woodruff, C.M. Jr., 1980, Regional Tectonic Features of the Inner Gulf Coast Basin and the Mississippi Embayment, *Gulf Coast Associations of Geologic Societies*.
- Yamashita, Y., Groom, D., Inazaki, T., and Hayashi, K., 2004, Rapid near surface resistivity survey using the capacitively-coupled resistivity system: OhmMapper, OYO Corporation, Japan, Geometrics, Public Works Research Institute, Japan.

APPENDIX

A.1 DATA REMOVAL

Table 6. Capacitively Coupled Electrical Resistivity Data Removal Percentages

This table shows the OhmMapper data removal percentages along with the RMS error percentages for each field site. A larger percentage of data had to be removed for this study than the SuperSting study because of higher sources of noise. The RMS error percentage was also higher for the OhmMapper because of higher noise source as discussed earlier.

Capacitively Coupled Electrical Resistivity Data Removal Percentages		
Field Site	% of Data Removed	RMS %
2	20.9	21.96
3	14.5	28.37
7	18.8	12.45

Table 7. Multi-Electrode Electrical Resistivity Removal Percentages

This table shows the percentage of data removed from each field site for all multi-electrode electrical resistivity surveys. The RMS (Root Mean Squared) percentage is also shown for each field site. The maximum amount of data removed at any field site was 14.3% while the highest RMS was found to be 9.93%.

Multi-Electrode Electrical Resistivity Removal Percentages		
Field Site	% of Data Removed	RMS %
1 (6.5m)	8.1	3.77
2 (4.0m)	10.1	3.34
2 (6.5m)	11.3	5.69
5 (6.5m)	5.6	3.25
7 (6.5m)	14.3	9.93

A.2 GRAVIMETRY CORRECTIONS

Field Site 1 Gravity Data									
Latitude	Longitude	Distance (m)	Observed Gravity (mGal)	Elevation (m)	Δ Elevation (m)	Rock Density (g /m-3)	Bouguer Anomaly (mGal)	Free Air Correction (mGal)	Corrected Gravity (mGal)
30.19194444	95.53638889	0	3720.929	45.7921	9.2921	2.65	0.001032487	2.86754206	3723.79551
30.19166667	95.53638889	25	3721.021	45.7921	9.2921	2.65	0.001032487	2.86754206	3723.88751
30.19138889	95.53638889	50	3721.147	45.7921	9.2921	2.65	0.001032487	2.86754206	3724.01351
30.19111111	95.53611111	75	3721.335	45.5421	9.0421	2.65	0.001004708	2.79039206	3724.124387
30.19083333	95.53611111	100	3721.47	45.2921	8.7921	2.65	0.00097693	2.71324206	3724.182265
30.19083333	95.53583333	125	3721.492	45.2921	8.7921	2.65	0.00097693	2.71324206	3724.204265
30.19055556	95.53583333	150	3721.442	45.2921	8.7921	2.65	0.00097693	2.71324206	3724.154265

Field Site 2 Gravity Data									
Latitude	Longitude	Distance (m)	Observed Gravity (mGal)	Elevation (m)	Δ Elevation (m)	Rock Density (g /m-3)	Bouguer Anomaly (mGal)	Free Air Correction (mGal)	Corrected Gravity (mGal)
30.196167	-95.527472	0	3722.805	49.188801	12.688801	2.65	0.00140991	3.915763989	3726.719354
30.196083	-95.527556	15	3722.794	49.188801	12.688801	2.65	0.00140991	3.915763989	3726.708354
30.196001	-95.527408	30	3722.907	49.188801	12.688801	2.65	0.00140991	3.915763989	3726.821354
30.195869	-95.527308	45	3723.001	48.938801	12.438801	2.65	0.001382131	3.838613989	3726.838232
30.195742	-95.527256	60	3723.109	48.938801	12.438801	2.65	0.001382131	3.838613989	3726.946232
30.195667	-95.527278	75	3723.136	48.938801	12.438801	2.65	0.001382131	3.838613989	3726.973232
30.195583	-95.527139	90	3723.124	48.938801	12.438801	2.65	0.001382131	3.838613989	3726.961232

Field Site 3 Gravity Data

Latitude	Longitude	Distance (m)	Observed Gravity (mGal)	Elevation (m)	Δ Elevation (m)	Rock Density (g /m-3)	Bouguer Anomaly (mGal)	Free Air Correction (mGal)	Corrected Gravity (mGal)
30.201053	-95.519806	0	3693.38	49.624363	13.124363	2.65	0.001458307	4.050178422	3697.42872
30.200647	-95.519606	25	3693.398	49.624363	13.124363	2.65	0.001458307	4.050178422	3697.44672
30.200583	-95.519556	50	3693.506	49.624363	13.124363	2.65	0.001458307	4.050178422	3697.55472
30.200442	-95.519403	75	3693.74	49.124363	12.624363	2.65	0.00140275	3.895878422	3697.634476
30.200269	-95.519403	100	3693.82	48.874363	12.374363	2.65	0.001374971	3.818728422	3697.637353
30.200106	-95.519228	125	3693.897	48.874363	12.374363	2.65	0.001374971	3.818728422	3697.714353
30.199925	-95.519069	150	3693.825	48.874363	12.374363	2.65	0.001374971	3.818728422	3697.642353

Field Site 4 Gravity Data

Latitude	Longitude	Distance (m)	Observed Gravity (mGal)	Elevation (m)	Δ Elevation (m)	Rock Density (g /m-3)	Bouguer Anomaly (mGal)	Free Air Correction (mGal)	Corrected Gravity (mGal)
30.208522	-95.504353	0	3695.857	54.415028	17.915028	2.65	0.001990619	5.528577641	3701.383587
30.208614	-95.504147	25	3695.906	54.415028	17.915028	2.65	0.001990619	5.528577641	3701.432587
30.208703	-95.503906	50	3696.122	54.165028	17.665028	2.65	0.001962841	5.451427641	3701.571465
30.208814	-95.503736	75	3696.1	54.165028	17.665028	2.65	0.001962841	5.451427641	3701.549465
30.208897	-95.503508	100	3696.113	54.165028	17.665028	2.65	0.001962841	5.451427641	3701.562465
30.208986	-95.503289	125	3696.066	54.165028	17.665028	2.65	0.001962841	5.451427641	3701.515465
30.208522	-95.504353	150	3695.857	54.415028	17.915028	2.65	0.001990619	5.528577641	3701.383587

Field Site 5 Gravity Data

Latitude	Longitude	Distance (m)	Observed Gravity (mGal)	Elevation (m)	Δ Elevation (m)	Rock Density (g /m-3)	Bouguer Anomaly (mGal)	Free Air Correction (mGal)	Corrected Gravity (mGal)
30.211833	-95.501011	0	3704.229	53.752323	17.252323	2.65	0.001916983	5.324066878	3709.55115
30.211639	-95.500806	25	3704.214	53.750323	17.250323	2.65	0.001916761	5.323449678	3709.535533
30.211417	-95.500761	50	3704.176	53.500313	17.000313	2.65	0.001888981	5.246296592	3709.420408
30.211253	-95.500667	75	3704.147	53.500313	17.000313	2.65	0.001888981	5.246296592	3709.391408
30.211056	-95.500572	100	3704.256	53.250313	16.750313	2.65	0.001861203	5.169146592	3709.423285
30.210917	-95.500406	125	3704.333	53.050313	16.550313	2.65	0.00183898	5.107426592	3709.438588
30.210694	-95.500344	150	3704.402	53.048313	16.548313	2.65	0.001838758	5.106809392	3709.506971

Field Site 6 Gravity Data

Latitude	Longitude	Distance (m)	Observed Gravity (mGal)	Elevation (m)	Δ Elevation (m)	Rock Density (g /m-3)	Bouguer Anomaly (mGal)	Free Air Correction (mGal)	Corrected Gravity (mGal)
30.229975	-95.457725	0	3722.55	39.047815	2.547815	2.65	0.000283032	0.786255709	3723.335973
30.229850	-95.457694	20	3722.596	39.045315	2.545315	2.65	0.000282754	0.785484209	3723.381201
30.229611	-95.457669	50	3722.708	39.020315	2.520315	2.65	0.000279977	0.777769209	3723.485489
30.229386	-95.457667	75	3722.809	39.017815	2.517815	2.65	0.000279699	0.776997709	3723.585718
30.229197	-95.457667	100	3722.828	38.517815	2.017815	2.65	0.000224155	0.622697709	3723.450474
30.228972	-95.457611	125	3722.865	38.267815	1.767815	2.65	0.000196383	0.545547709	3723.410351
30.228775	-95.457583	150	3722.872	38.242815	1.742815	2.65	0.000193606	0.537832709	3723.409639

A.3 CROSSPLOT OF MEASURED VS APPARENT RESISTIVITY

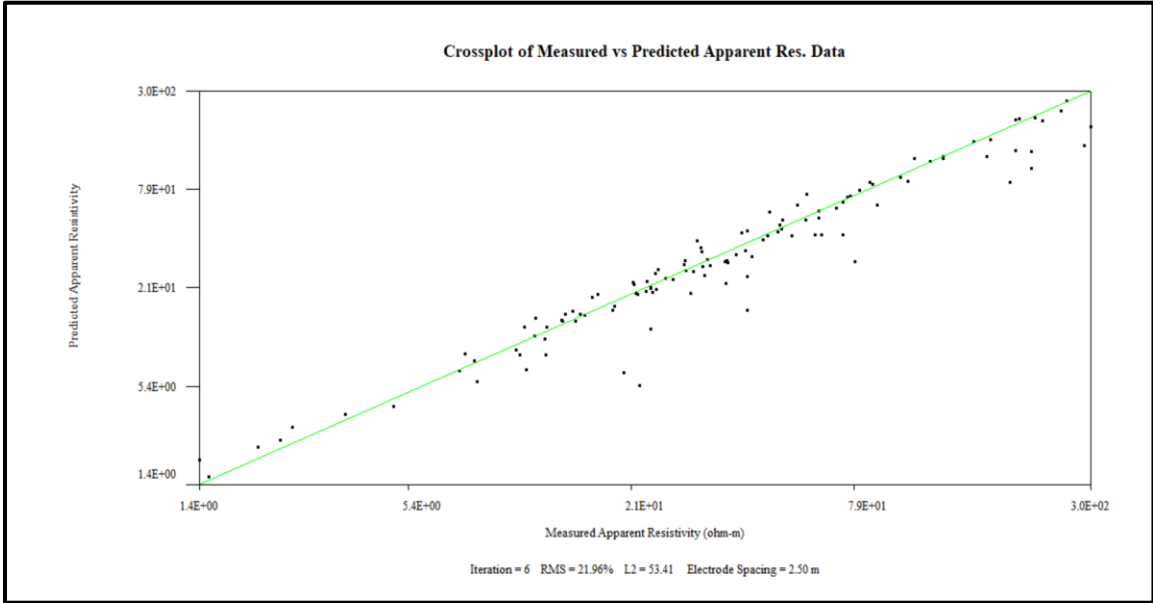


Figure 67. Crossplot of Measured vs. Apparent Resistivity from CCR Survey Site 2

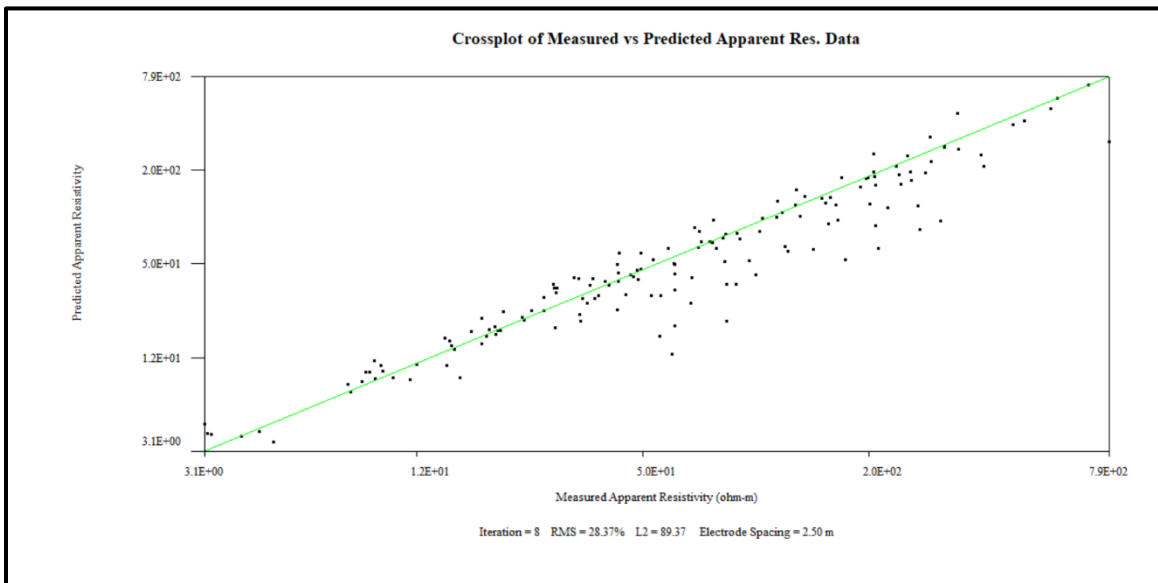


Figure 68. Crossplot of Measured vs. Apparent Resistivity from CCR Survey Site 3

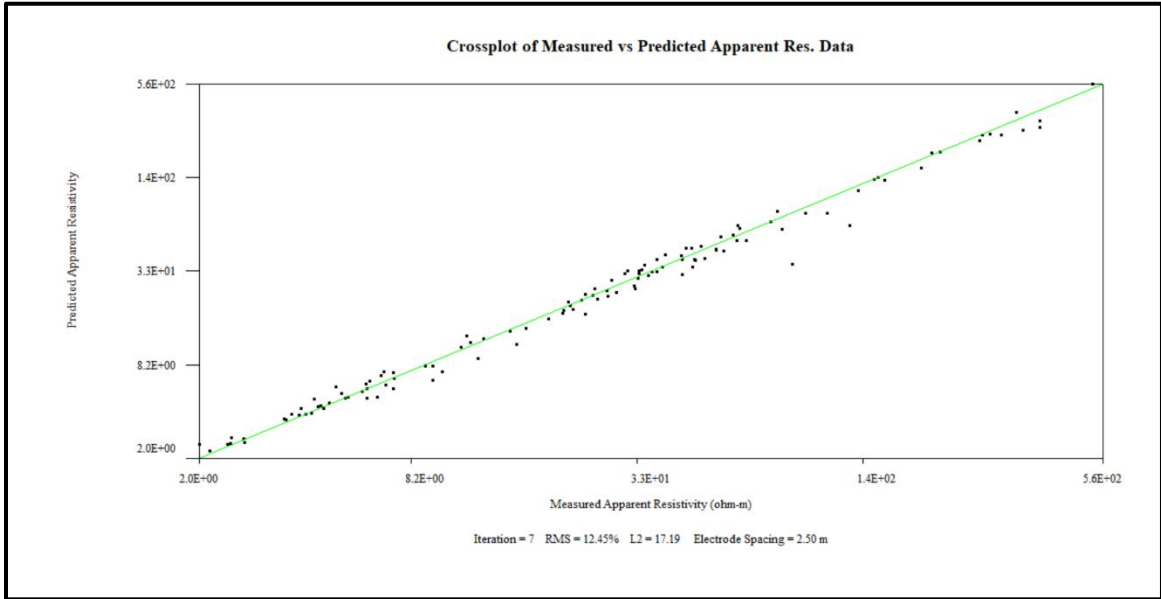


Figure 69. Crossplot of Measured vs. Apparent Resistivity from CCR Survey Site 7

Multi-electrode Resistivity Data Crossplot

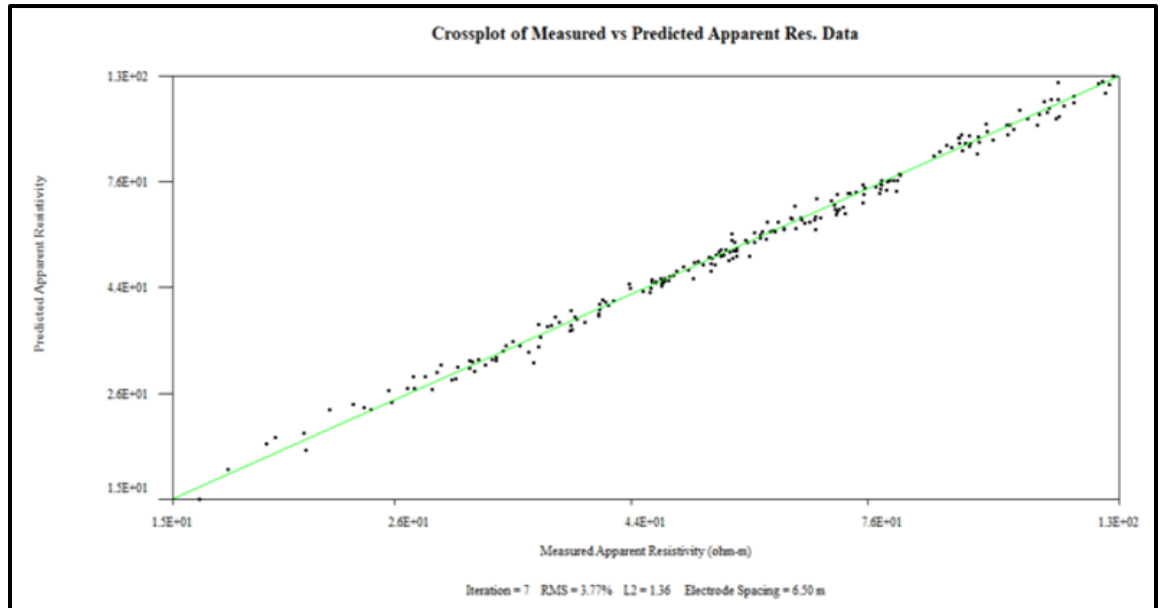


Figure 70. Crossplot of Measured vs. Apparent Resistivity from Multi-electrode Resistivity Survey Site 1

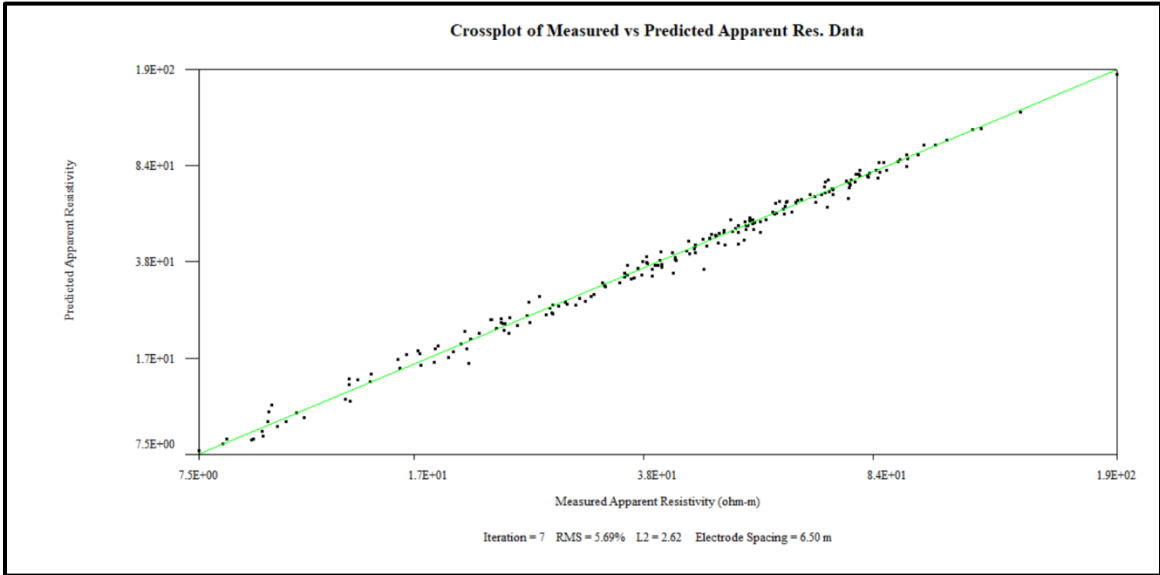


Figure 71. Crossplot of Measured vs. Apparent Resistivity from Multi-electrode Resistivity Survey Site 2

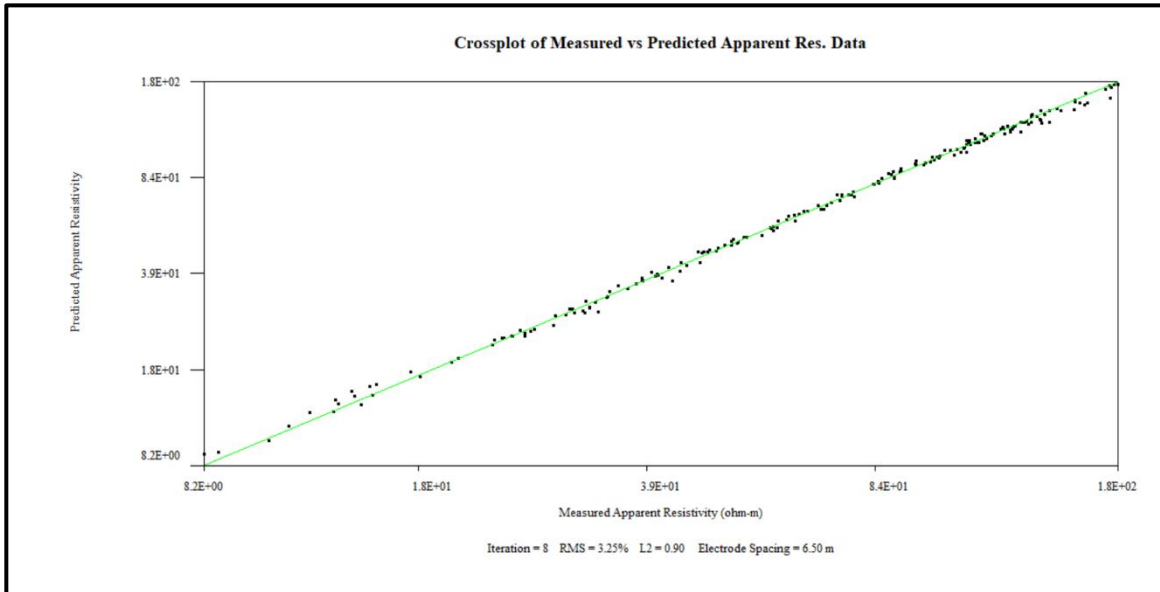


Figure 72. Crossplot of Measured vs Predicted Apparent Resistivity from Multi-electrode Resistivity Field Site 5

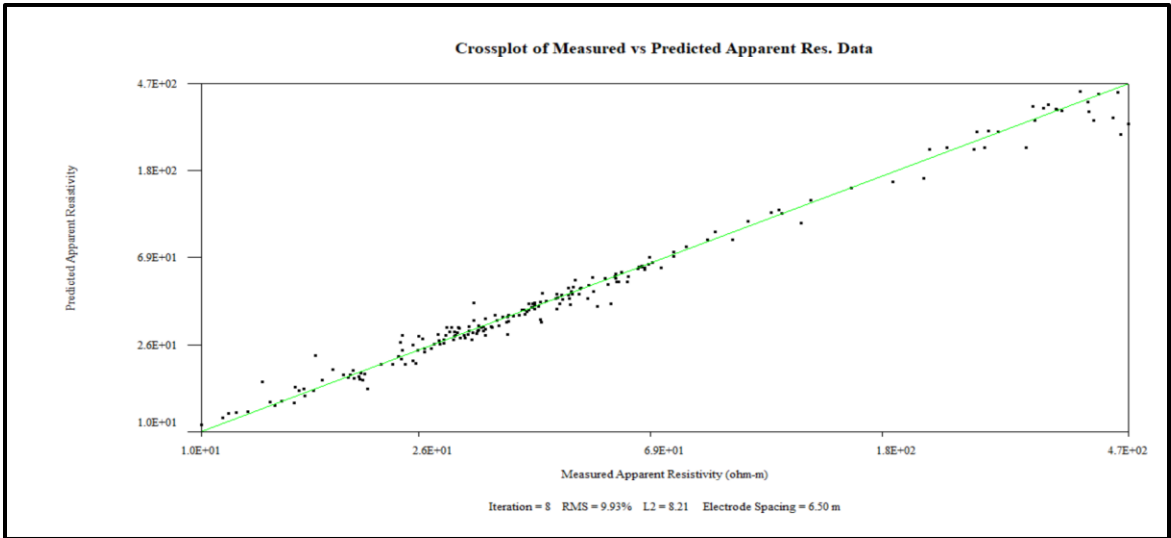


Figure 73. Crossplot of Measured vs Predicted Apparent Resistivity from Multi-electrode Resistivity Field Site 7

VITA

After graduating from Klein Collins High School, Spring, TX, in 2011, Danielle Minter entered Stephen F. Austin State University in Nacogdoches, TX. She received the degree of Bachelor of Science from Stephen F. Austin State University in August, 2016. In January 2017, she entered the Graduate School of Stephen F. Austin State University, and received the degree of Master of Science in May of 2018.

Permanent Address: 523 Willow Wisp Circle
 Spring, TX 77388

Style manual designation: Geological Society of America

This thesis was typed by Danielle R. Minter